APPROACHES FOR POWER GRID MANAGEMENT AND ANCILLARY SERVICES WITH DC-AC MICRO-GRIDS COMPRISING OF PV FARM AND HYBRID ENERGY STORAGE SYSTEM

by

Aniket Mohan Joshi

A dissertation submitted to the faculty of
The University of North Carolina at Charlotte
in partial fulfillment of the requirements
for the degree of Doctor of Philosophy in
Electrical Engineering

Charlotte

2021

Approved by:

_____
Dr. Sukumar Kamalasadan

_____
Dr. Madhav Manjrekar

_____
Dr. Valentina Cecchi

_____
Dr. Craig Ogle

ABSTRACT

ANIKET MOHAN JOSHI. Approaches for power grid management and ancillary services with DC-AC micro-grids comprising of PV farm and hybrid energy storage system. (Under the direction of DR. SUKUMAR KAMALASADAN)

The emergence of the concept of DC grids comes from the fact that there is an increasing number of power grid components that naturally operate with DC power. The combined trend of DC sources and loads in power grids is an important player in the sudden growth of research interest in DC micro-grids and their interplay with the main power grid. Even though DC grids are easy to implement on a small scale and their own, the connection of the DC micro-grid with the AC power grid takes research problems to another level. Innovative approaches, methods, distribution system architectures, and control strategies are required to manage and mitigate the problems of involving DC micro-grid in conjunction with conventional power grids. Through this research work, novel, innovative and comprehensive system architectures and control strategies are proposed to mitigate some of the problems of DC micro-grid like DC-AC micro-grid interplay during steady-state and dynamic conditions, tandem operation of DC, and AC micro-grids for frequency regulation. The dissertation also proposes the concept of a DC ring architecture to emulate a small residential community using a common DC-bus-centric structure. The research work aims to provide a comprehensive DC-AC micro-grid design and control architecture that can provide a platform for testing and validation of steady-state and fault time system performance. The proposed methods in each chapter have been incorporated and validated on standard distribution test systems provided by IEEE like the 13 bus and 123 bus systems and hence their analysis is crucial and could serve as a reference for future design and control of DC micro-grids.

In this work, first, a new approach for improving grid inertia based on a Photo-Voltaic (PV) farm in conjunction with a fully active Hybrid Energy Storage System

(HESS) comprising of battery and ultra-capacitor is proposed. The approach captures grid dynamics using the Point of Common Coupling (PCC) angle measurements (δ) at the inverter terminal. The proposed approach in this thesis demonstrates an overall improvement in the inertial response of the system by up to 25% compared to the conventional frequency-droop approach. It also records a faster settling time than the frequency-droop approach by up to 47 seconds. The approach has been tested using an error minimization-based Proportional-Integral (PI) control and an error minimization-based Optimal Control (LQR) for frequency regulation. This method utilizes the rate of change of PCC angle ($\frac{d\delta}{dt}$) which is observed to vary based on the proximity of PCC to the grid dynamic location. It has been observed that the proposed architecture controls the Rate of Change of Frequency (RoCoF) and primary and secondary frequency response without the need for frequency-droop information of the system, thereby ensuring grid stability that utilizes renewable energy-based resources. The second contribution is a novel voltage angle minimization-based approach for grid inertia improvement which further updates and validates the proposed test system and primary control that was used for the previous approach discussed above. The proposed method successfully quantifies and differentiates grid dynamics from steady-state conditions by measuring the deviation of voltage angles at the DER interconnection bus ($\Delta\delta$). A Linear Quadratic Regulator (LQR) controller with a quality function is formulated to minimize ($\Delta\delta$) during the event of grid dynamics for frequency regulation of the distribution system by optimal dispatch of HESS. The proposed LQR architecture is observed to perform better for inertial support when compared with the conventional frequency-droop approach. Third, a novel architecture that dynamically updates LQR penalty gains based on a combination of recursion and energy storage ramp-rate function is proposed. This helps control the HESS devices separately and not based on their size. The proposed approach is considered as an improvement on the static gain LQR with the added attribute of being

robust to uncertainty in the control input. Finally, a concept of DC Ring where 4 DERs are connected to emulate the electrical network of a small residential community is introduced. An Alternating Direction Method of Multipliers (ADMM) based Multi-Input-Multi-Output (MIMO) identification is used to completely identify the dynamic state-space of 4 DERs along with AC-interfacing two 3-phase $d-q$ inverters. This approach is used to generate globally optimized LQR control actions for each of the 4 DERs based on individual weighting factors provided by ADMM. These weighting factors are deduced by drawing a consensus among each output to control the input transfer function. The approach generates globally coordinated control setpoints for all DERs that can detect the change in ($\Delta\delta$) corresponding to the fault event.

DEDICATION

This dissertation is dedicated to my family (Aai, Baba, Aaji and Nikhil), cousins and friends who have stood firmly by my side and have been my pillars of strength, inspiration and courage throughout this entire journey.

ACKNOWLEDGEMENTS

I would like to express my gratitude towards my family for believing in me and supporting me mentally and financially to follow my dream of pursuing higher education in the USA. They have been with me throughout this process and never let me feel away from home.

I thank my adviser, Dr. Sukumar Kamalasadan, for his guidance and motivation. His ideas instilled in me a clear approach towards solving my problems and his mentorship kept my desire to positively work towards my goals and achieve them in time. I would also like to thank my dissertation committee members : Dr. Valentina Cecchi, Dr. Madhav Manjrekar and Dr. Craig Ogle for their valuable feedback during the entire process that helped me improve my work significantly.

My friends and colleagues have been my family away from home and I cannot thank them enough for the support they have given me to see through this journey.

TABLE OF CONTENTS

LIST OF TABLES

LIST OF FIGURES

CHAPTER 1: INTRODUCTION

1.1 General Background

The face of the electrical power grid has been changed by economic, technology, and environmental incentives through recent decades. Centralized generation is giving way to smaller and compact distributed generating structures encompassing a wide range of prime mover technologies like micro-turbines, PV farms, fuel cells, and gas combustion engines. Generally, these devices have an inverter to connect with the electrical distribution system. Penetration of distributed generation in various parts of the power grid is growing over the decade and along with it rises the danger of destabilization due to improper integration practices. To realize the emerging potential of distributed generation a system approach needs to be taken by viewing these generation and associated loads as a subsystem called micro-grid. This approach promotes local control of distributed generation and eliminates the need for a central dispatch. These generation units also have the flexibility of being able to easily island themselves in cases of disturbance without harming the transmission grid′s integrity. Apart from this, intentional islanding of generation and loads also has the potential to provide for higher local reliability than the power grid itself. The size and optimally placed distributed generation can more than double the overall efficiency of the system.

Micro-grids can be majorly classified in AC and DC topologies. This classification is based on the method of connecting micro-grid components through a common bus structure. In the case of AC micro-grids, the common bus connection is AC coupled, whereas it is DC coupled in DC micro-grids. The nature of power grid topology around the world is primarily AC. This is because the AC system we found

to be more cost-effective for generation, transmission, and distribution during the time the power grid concept was developed. Also, most of the loads during that time were AC loads. But that is not the case anymore. With the rise of computers more and more DC load-based devices are trying to interact with the power grid. These cause overloading problems in the existing grid because the existent power conversion devices are proving incapable of handling the ever-increasing DC load demand. Also, adding more of the DC-AC power converters makes grid operation complex and inefficient due to the incurred DC-AC conversion losses.

A micro-grid is a group of distributed generating sources, distributed energy storage, sensitive and non-sensitive loads, and a centralized/decentralized control system, operating as a single controllable subsystem. These can operate in a grid-connected and islanded mode of operation. The DC micro-grid generally comprises one or more sources which are Distributed Energy Resources (DERs) along with ancillary devices which support the primary generating source and DC loads. So, a modular DC micro-grid would consist of a PV farm or a wind farm and a hybrid energy storage system which comprises of battery and capacitors. Loads would involve local DC loads. All the systems are connected to a common terminal called DC link which acts as a communication link between internal components of the DC micro-grid as well as outside it. The other end of the DC link is connected to AC power conditioning devices called inverters. The system would look like figure 1.1 The inverters can either be current source or voltage source inverters depending on the parameter they can control while transferring power.

Reliable and stable operation of a micro-grid with its multiple DGs demand an energy management system (EMS) that allocates real and reactive power set-points to the DG units to allow for proportional and economic sharing of power among the DG units. This also ensures balanced generation with load and maintains system frequency with a quick response to any disturbances and transients. Thus involving a

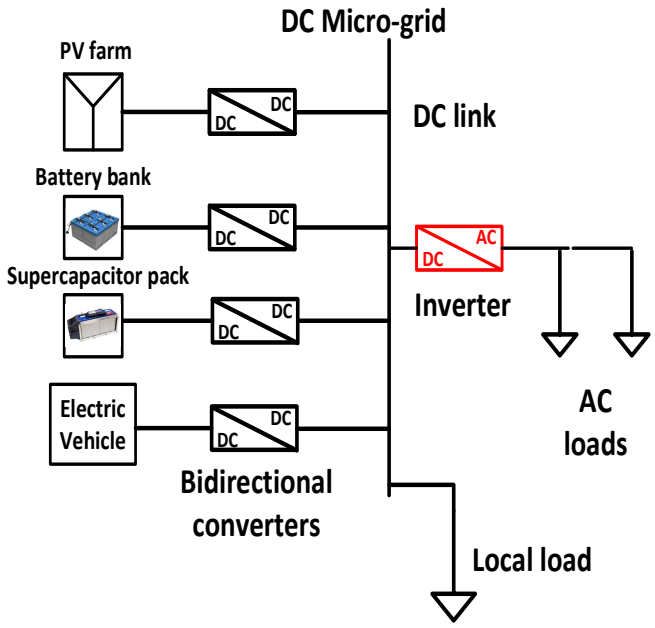

Figure 1.1: Modular DC micro-grid

hierarchical EMS provides a system with a seamless transition from islanded mode to a grid-connected mode of operation [1], [2]. The droop method of control for parallel operation of uninterruptible power supply inverters is proposed in [3]. The output of voltage of every inverter should have the same magnitude, frequency, and phase angle for equal sharing of the load as mentioned in [3]. The droop control takes care of this condition by using local measurements for regulating the voltage and frequency of the ac micro-grid.

If we look at the general trend in power grids, DC-based sources and loads are on the rise. This is because advancements in the field of Information and technology have increased the number of electronic devices like laptops, LED lights, and other data and telecommunication accessories. This entire influx of load on the power grid is DC in nature. Additionally, the current and future trend of Electric Vehicles (EV) point to the fact that DC loads will keep on increasing [4]. Most of the DERs are operated by DC sources like PV, wind, fuel cells and their supporting accessories like batteries and ultra-capacitor storage system are all favorable for DC integration [5]. Easy

integration of such DC loads and sources into a DC micro-grid will mean flexibility and increased efficiency compared to an AC micro-grid.

DC micro-grids also have a lot of advantages when compared to AC micro-grids. Implementation of DC topology reduces the number of converters used to supply DC loads and improved efficiency due to reduced DC-AC energy conversion loss. DC micro-grids enable the connection of a wide range of DC source DERs and also provide an easier micro-grid integration approach for energy storage systems. Unlike AC micro-grids, DC micro-grids do not require synchronization of generators and hence allowing them to operate at their optimum speeds. The addition of EV is favorable for DC miro-grids, where they can serve as a controllable load as well as a generation by supporting grid as part of ancillary service. DC link topology in micro-grids provides the flexibility of controlling the power output of all devices individually. They enable unequal power-sharing based on higher-level optimization routines. In case of malfunction, only the affected section of DC source DER can be isolated and the rest of the system can perform under normal operating conditions, thus making it easy for detection and isolation of faults.

1.2 Motivation

Although research interests in DC micro-grids are increasing, there are still some research gaps that the author has discovered after reviewing articles about DC micro-grids and the frequency regulation approach. First of all, there is a need for a comprehensive micro-grid model with DC-AC hybrid interconnection capabilities. This helps in the study of both DC and AC systems and related multi-level control architecture. The model should involve a primary and secondary level controller for DERs and various storage devices and should be easily integrable into a distribution test system for validation of high-level control architectures. Secondly, there needs to be a DC bus-centric structure of DER and loads, like a DC Ring, to perform modeling and control study of DC connected systems. Another research area that hasn't been

studied in depth is the design and control of storage system architecture that can simultaneously support PV intermittence mitigation and grid-side frequency regulation. Lastly, an alternative approach to frequency-droop regulation is needed because the control approach depends heavily on the successful extraction of droop characteristics of the system [6]. These characteristics do not remain constant in the event of a fault or increased loading in the system as the resistance-impedance (R/X) ratio is changed. This thesis proposes solutions that deal with all the above-mentioned research shortcomings in the field of power grid study.

The motivation behind this research work is to recognize and reconsider the importance of DC-micro-grids in a broader picture. With the emergence of Distributed Energy Resources (DERs), DC-micro-grids has slowly started gaining attention. Researchers have started identifying the advantages of DC-centric micro-grid topology. Also, hybrid DC-AC systems are studied extensively due to the flexibility of connecting both AC and DC loads. Coordination of such DC and AC topologies is achieved by adopting hierarchical control strategies broadly classified into primary droop control, distributed secondary control (DC-bus signaling), and centralized secondary control (coordination control).

This thesis provides an alternative to the conventional frequency-droop approach for micro-grids, in general, while supplying for inertial and secondary regulation in a distributed system network. The proposed approach uses the Point of Common Coupling (PCC) angle (δ) as an information parameter and changes in the angle, ($\Delta\delta$), are used as a deterministic gauge for the measure of sensitivity to fault or grid dynamic.

1.3 Thesis Outline

The thesis outline is as follows:

Chapter 2 is a comprehensive literature review of the state-of-the-art distribution micro-grid systems investigating connection topology, energy storage device selection,

and sizing, control hierarchies, and evolving trends for the future.

Chapter 3 proposes a PCC angle-based frequency regulation approach that regulates grid frequency dynamics and at the same time controls the rate of frequency. The proposed framework aims at frequency regulation-based extended inertia support. The outer loop detects the rate of change of (δ) and operates a conventional Proportional-Integral (PI) controller to achieve frequency regulation. The inner loop distributes the control set-points to high energy density battery and high power density ultra-capacitor devices using a frequency-dependent power-sharing approach. This chapter also tests the proposed approach using an optimal control (LQR). The minimization function is aimed at mitigating the rate of change of PCC angle.

Chapter 4 extends the proposed PCC angle-based frequency regulation approach to multi-micro-grid structure (2 micro-grids) in a distribution system. Moreover, it studies the effect of severity and fault location on the change in ($\Delta\delta$) for PCCs of multi-micro-grids. An optimal control approach based on angle minimization is proposed in this chapter and the result is compared with the conventional frequency-droop approach.

Chapter 5 proposes an optimal robust controller based on control uncertainty that includes dynamically updating state and control penalty factors Q and R. To optimize the power-sharing of energy storage devices the control penalty factor update is made dependent on the sensitivity of frequency to power contributed from each device.

Chapter 6 expands the proposed PCC angle control approach into a Multi-Input-Multi-Output (MIMO) model for micro-grids connected in the distribution system. Also, the distribution system is modified with an outer DC-ring structure where 4 micro-grids are connected. There are 2 locations of PCC for the inverter to connect the DC-ring to the distribution network. Thus the proposed approach is validated on a hybrid AC-DC micro-grid topology. MIMO model is derived using the Alternating Direction Method of Multipliers (ADMM) which is capable of solving convex opti-

mization problems by breaking them down into smaller pieces. The ADMM tool is used to derive a sensitivity transfer function for each micro-grid. When these sensitivity gains are implemented for the individual micro-grids a globally optimized solution is achieved. The proposed approach is implemented using the global optimization ADMM algorithm.

Chapter 7 concludes the thesis with a summary of results compiling the proposed frequency regulation framework, its implementation on distribution system comprising of multi-micro-grids and improvements due to application of control optimization. A probable path towards extending this work into the future is also be discussed.

CHAPTER 2: STATE-OF-THE-ART MICRO-GRID AND DC MICRO-GRID SYSTEMS: LITERATURE REVIEW

2.1 Foreword

The literature review provides a summary of the research material that is directly or indirectly related to the proposed work carried out in the thesis. This chapter aims at covering the state-of-the-art design and control approaches in the field of DC and AC micro-grids.

2.2 Current work on DC micro-grids

Present control techniques in DC micro-grid can be classified in three prominent groups based on the hierarchy of control adopted:

- Decentralized Primary Control (Droop control)
- Distributed Secondary Control
- Centralized Secondary Control

2.2.1 Decentralized Primary Control

Various types of droop control approaches can be seen such as in [7]. In this paper control of dc micro-grid involves reduced reference dc voltage with increased output current. This conventional droop degrades current-sharing accuracy due to creating unequal voltage drops across line resistance. A virtual resistance-based droop strategy can also be seen implemented to achieve power-sharing in [8]. An adaptive droop control based on instantaneous virtual resistance is proposed in [9] to minimize the current sharing difference among converters.

2.2.2 Distributed Secondary Control

Distributed dc-bus signaling-based control approach where dc bus voltage monitors the action of interface converters of sources and loads of the micro-grid is proposed in [10] and a digital average current sharing based approach for voltage regulation and accurate load sharing is proposed in [11].

2.2.3 Centralized Secondary Control

As a centralized approach, a voltage control method based on fuzzy logic with gain scheduling is implemented for dc micro-grid involving electric double layer capacitor storage system in [12]. Also, a real-time EMS with adaptive energy analyzer based on moving average technique is discussed for a dc micro-grid in [13]. A practical implementation of coordination and wireless strategy for multiple dc sources is found at the Nanyang University of Technology in Singapore [14].

2.3 Types of micro-grid

Micro-grid planning is necessary for determining the optimal size and the generation mix of distributed energy resources (DERs), as well as the micro-grid type, i.e., AC or DC. Considering the growing ratio of DC loads and DERs, dc micro-grids could be potentially more beneficial than ac micro-grids by avoiding the need to synchronize generators, reducing the use of converters, facilitating the connection of various types of DERs and loads to the micro-grid common bus with simplified interfaces, and reducing losses associated with the ac-dc energy conversion. The selection of microgrids is based on economic considerations, where the planning objective includes the investment and operation costs of DERs, cost of energy purchase from the main grid, and the reliability cost [15].

Based on the voltages and currents adopted in a micro-grid, they can be classified into three types:

- AC

- DC
- Hybrid

In AC micro-grids, all DERs and loads are connected to a common AC bus. The DC generating units, as well as energy storage, are connected to the AC bus via inverters. On the other side, AC to DC rectifiers are deployed to supply DC loads.

In DC micro-grids, the case is opposite to that of AC micro-grid. Here the DC bus acts a the common bus and DC loads are directly connected to the DC bus. Whereas the AC loads are fed through DC-AC inverters.

In hybrid micro-grids, both types of buses exist prominently and connections to each are made depending on the proximity of the source or load to the bus.

[16] discusses a planning model for ac micro-grid considering the uncertain physical and financial constraints. Here, the micro-grid problem is broken down into an investment problem and an operational problem. [17] suggests an operating model of hybrid DC-AC micro-grids stressing the advantages of both AC and DC micro-grids on system and device levels.

2.4 Advantages of DC micro-grid

Even though the utility grid is AC and hence employing AC DERs can be perceived for a majority of study and control, the DC micro-grid offers numerous advantages over AC micro-grid when a detailed comparison is done [18].

The advantages of DC micro-grid over AC micro-grid are as follows:

- Higher efficiency and reduced numbers of converters to supply for DC loads
- easier integration of various DC DERs and storage devices
- increased efficiency due to easy addition of dc loads, electric vehicles, and LED lights

- eliminating synchronization for generators enabling them to operate at their optimum speeds
- eliminating the need of synchronization on bus ties
- significantly increased DC loads like laptops, LED lights, data and telecommunication are an easy fix into the DC bus micro-grid

2.5 Evolving trends in DC micro-grid

The multi-micro-grid concept, proposed in [19], involves dividing the distribution system into several micro-grid-like regions. This is carried out to give more flexibility and apply smart grid concepts like self-healing, resilience, intentional islanding, and other dynamics.

In the future, micro-grids will involve a large amount of active and passive energy storage components. An example can be given about EVs making their mark on the micro-grid. They can serve as a controllable load as well as generation and maintain the supply by supporting the grid.

Control, protection, and stability of dc micro-grid is a challenge arising due to the absence of zero crossing of current. Not a lot of research has been conducted in this direction to improve protection methods. The control with clustered micro-grid and EV as active load by incorporation of smart meters and two-way communication technique can be investigated in detail [20].

Game theory-based concepts such as non-cooperative game theory are finding their way into research for solving complex optimization problems and distinguishing their results, especially when the end-users are making their decisions non-cooperatively. This has been discussed in [21]

2.6 Power and Energy management of DC micro-grid

Distributed generations have a characteristic of being intermittent due to their medium of sourcing power. PV suffers from intermittence due to a lack of solar

insolation. Weather conditions and temperature play a key role in determining the output of PV farms. In the case of wind farms, wind velocity plays an important factor in determining the output power.

To mitigate the problem of intermittence and make the DERs dispatchable and reliable storage systems provide multiple advantages like [22]:

- renewable energy time shift
- renewable capacity firming
- frequency regulation
- energy arbitrage
- reactive power support with converters

Electrochemical batteries, flow batteries, capacitors, compressed air energy storage, flywheel energy storage, pumped hydroelectric, and superconducting magnetic energy storage (SMES) are some of the available storage options for today's systems. The selection of a storage device is very specific to its application.

2.6.1 Power Vs Energy application

While characterizing the rating of a storage system, two key criteria that are addressed are power and energy. Power determines the rate at which the system can supply energy. Energy relates to the amount of energy that can be delivered to the load. Thus the amount of energy stored denotes the amount of time that the system can discharge at its rated power output. This is called a discharge duration.

The Ragone chart shown in figure 2.1 is used as a medium of comparison between Power density and Energy density of various storage devices. The scales of this chart are logarithmic to incorporate an entire range of storage devices.

Based on this chart it can be observed that Li-Ion batteries and supercapacitors lie on either side of the Power and Energy density spectrum. This means that a

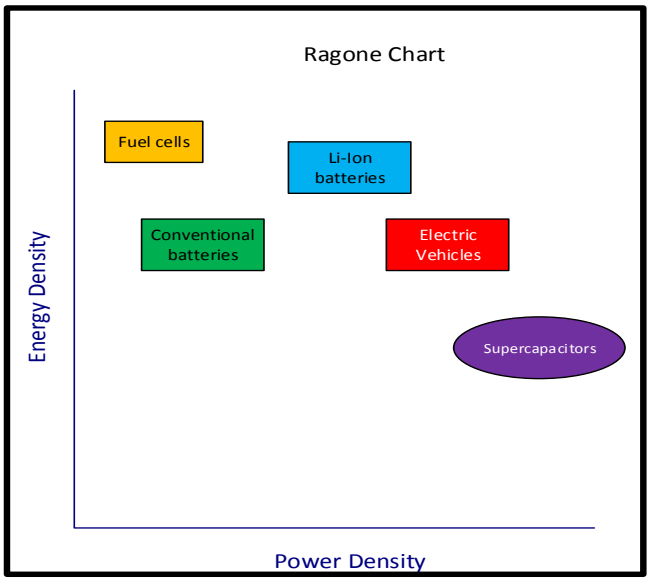

Figure 2.1: Ragone Chart

combination of Li-Ion batteries and supercapacitor would make the storage device capable of supplying for both high power and high energy demands wherein battery can be used as a high energy density device and super-capacitor can be operated to supply high power demands for a short duration.

2.6.2 Storage Power

The storage system's power rating is assumed to be the system's nameplate power rating under normal operating conditions. For applications that require a storage system to supply its maximum power output only for a short duration of time, the storage power specification is taken into consideration.

2.6.3 Energy density and Power density

Power density is the amount of power that can be delivered from a storage device with a given volume or mass. Energy density is the measure of the energy that can be stored in a storage device that has a given volume or mass.

Table 2.1: Round-trip efficiencies for various energy storage systems

S.No	Storage type	Round trip efficiency
1	Conventional Electrochemical batteries	60-70%
2	Advanced Electrochemical batteries	75-80%
3	CAES	73-80%
4	Pumped hydroelectric	75-78%
5	Flywheel storage	80-90%
6	Capacitors and SMES	95%

2.6.4 Storage system round-trip efficiency

The round-trip efficiency of a storage system reflects the amount of energy that is discharged from the storage system relative to the amount put into the system during charging mode. Table. 2.1 shows the round-trip efficiencies of different storage devices [22].

Energy storage applications can be classified depending on their localization as electric supply-based, ancillary service-based, Grid system, End user-based, and Renewable energy supporting. Table 2.2 showcases the energy storage applications based on the mentioned classification

2.6.5 ESS topologies

The classification of ESS topologies can be made as follows:

- DC link topology
- Cascade topology
- AC link topology
- DC-AC link topology

2.6.5.1 DC link topology

The DC link topology involves all the devices (primary source and storage devices) connected to a common DC link as shown in figure 2.2. The DC link serves as a

Table 2.2: Energy storage applications

S.No	Application type	Application
1	Electric supply	Electric energy time-shift
2	Electric supply	Electric supply capacity
3	Ancillary services	Load following
4	Ancillary services	Area regulation
5	Ancillary services	Electric supply reserve capacity
6	Ancillary services	Voltage support
7	Grid system	Transmission support
8	Grid system	Transmission congestion
9	Grid system	T and D upgrade deferral
10	Grid system	Substation on-site power
11	End user	Time use Energy cost management
12	End user	Demand charge management
13	End user	reliability
14	End user	power quality
15	Renewable Integration	Renewable energy time-shift
16	Renewable Integration	Renewable capacity firming
17	Renewable Integration	Wind farm grid integration

communication link between all the devices connected at the common voltage level. This topology has the flexibility of controlling the power output of all the devices individually. It can also enable unequal power-sharing based on higher-level optimization routines. In case of malfunction of one of the devices, the storage system can function with reduced power output.

2.6.5.2 Cascade topology

In the Cascade topology, the generator and the storage devices are connected one after the other in cascading fashion. The only advantage of this method of connection is that it requires a lesser number of power converters. However, there are a lot of drawbacks to such topology. Lack of flexibility means that it is impossible to control each device separately. This also prevents the system from receiving optimal setpoints for different storage devices. In case of failure of one device, the system is at risk of losing all its power due to the way the topology implements cascading for its devices.

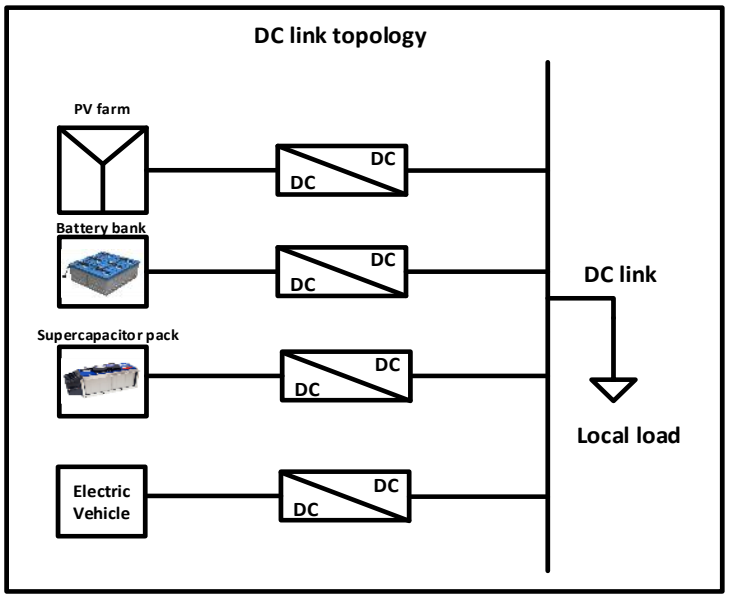

Figure 2.2: DC link topology

2.6.5.3 AC link topology

In this type of topology, the storage system is connected to the AC link instead of the DC link voltage. Each device can have a dedicated inverter or they can be grouped and connected to a common inverter. The individual droop of the inverters can be used as a reference signal for optimization in cases of higher-level control application. Figure 2.3 shows the AC link topology of the micro-grid.

2.6.5.4 DC-AC Link topology

This topology combines the DC link and AC link topology and has the flexibility discussed in these structures. Such topologies are used where the storage requirements are on both the AC and the DC link of the system and such system will exhibit good reception of hierarchical control due to the availability of a controller on either side of the links. Figure 2.4 shows the DC-AC link topology.

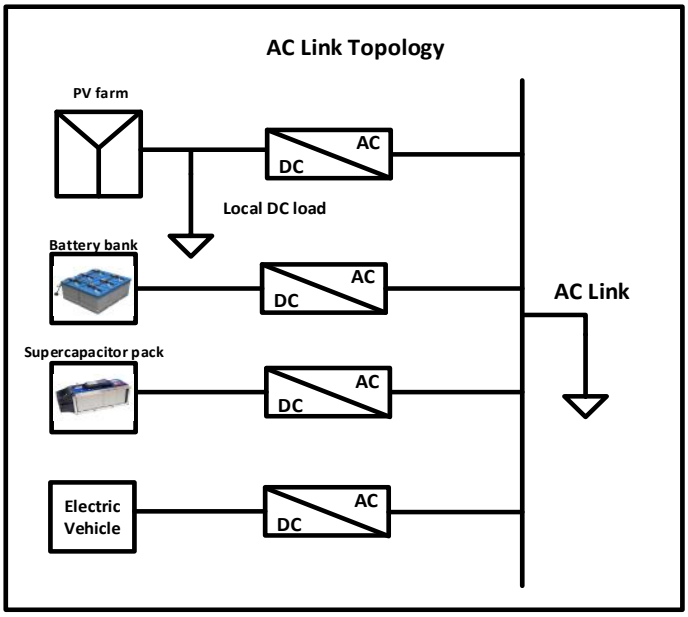

Figure 2.3: AC link topology

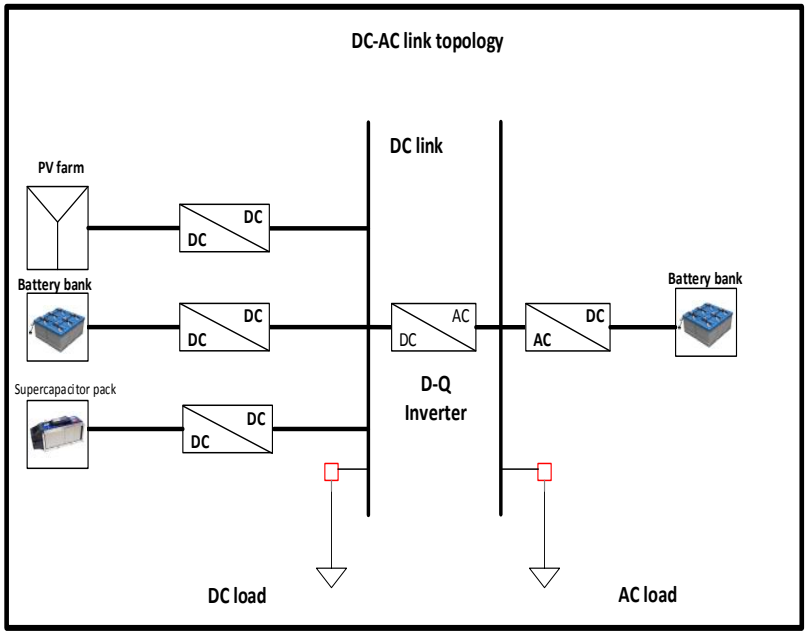

Figure 2.4: DC-AC link topology

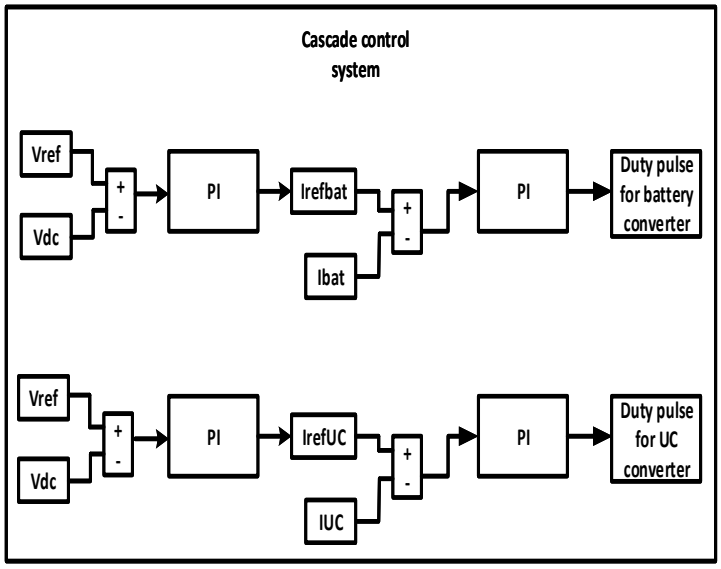

Figure 2.5: Cascade control for ESS in DC link topology

2.6.6 Battery and Ultracapacitor Management

ESS management can be accomplished by employing converters as power conditioning devices to change the nature (DC or AC) and voltage level while supplying to the micro-grid. Depending on the topology with which the storage device is connected to the micro-grid either a DC-DC bidirectional converter is selected or a voltage source inverter (VSI) is chosen as the power conditioning device. In the case of an AC link topology for a storage system, the voltage source inverter can be operated in dc voltage control mode. This mode of operation is similar to the grid supporting or grid forming mode of operation of the inverter. Here the job is regulation of the DC link voltage by the supply of absorption of power by a storage device (in this case, battery) [23].

For a storage system employing a DC link topology, a DC-DC bidirectional converter is used to change the voltage level at the output of the ESS. A generic control structure governing the charging and discharging mode of operation of battery and UC system is shown in figure 2.5. In this control structure, the DC link voltage serves as an information parameter about the power demand on the DC link. The

error in the voltage is balanced by either charging or discharging of the ESS depending on the direction of the error signal generated. A simple PI compensator is used to generate an equivalent duty pulse that the converter needs to operate on to regulate the voltage. Cascading of the control signal to generate an intermediate current control option can prove helpful in applying optimization routines on the rate of charge/discharge or per unit capacity sharing of the storage device. A more optimized power-sharing approach is described in [4]. This approach utilizes the concept of high power density and high energy density of a hybrid energy storage system involving battery and ultracapacitors. It uses frequency-based splitting of current demand for the ESS and generates a current reference for each of the storage devices. Different levels of control strategies and algorithms have been implemented on ESS such as simple dead beat control, cascade PI compensator, multi-level power management controller [24], [25], [26]. Most of the research demonstrated is focused on power enhancement, discharge cycle life, specific power, and energy loss concerning pulsed load profiles [27].

2.6.7 Energy Source Management

The two main DERs that are implemented currently in the DC micro-grid are the PV and wind generators. The PV generator is a DC source and contains no moving parts whereas a wind generator is an induction machine. The power available at the PV output is DC power which needs to be processed by using power conditioning devices. Since the PV is a DC source a DC-DC unidirectional converter is used to serve the purpose. Depending on the voltage level of PV generation the converter topology can either be buck or boost. The maximum power point tracking technique is used to extract maximum power from the PV farm. Thus the converter operates in input voltage control mode. This way it can be observed that the PV and ESS control systems complement each other in terms of regulation of voltage at different terminals.

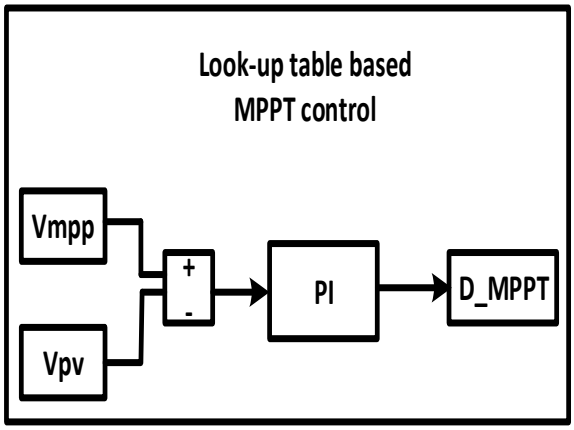

Figure 2.6: MPPT control loop for DC-DC converter

Various MPPT techniques are implemented for PV applications like hill climbing (HC), fuzzy logic control (FLC), perturbed extremum seeking control (PESC), firefly algorithm (FA), and cuckoo search algorithm (CS) [28]. Other commonly used MPPT algorithms are Perturb and observe (P and O) and Incremental conductance test (IC). A look-up table-based MPPT is also implemented in [29]. Figure 2.6 shows the control structure of look-up table based MPPT control. As (P and O) and (IC) algorithms are only suitable for PWM converters, resonant converters with high efficiency and the capability to operate at very high switching frequency can be used as a pre-stage DC/DC with MPPT [30]. For wind generators, a d-q transform-based inverter is used as a power conditioning converter. Papers [31] and [32] discuss this type of inverter structure for DFIG wind plants.

2.6.8 Integration and Management of DC micro-grid

The integration and management of DC micro-grid include tandem arrangement and functioning of control structure implemented for each source and storage device.

For the case discussed in PV energy source management, there is no need for a supervisory control to direct regulatory reference as the PV MPPT and the ESS cascade control complement each other and balance the voltages on all the dc terminals. Though optimization routines can be implemented in the current loops of the storage

devices to dictate the current sharing of each device. Moreover, supervisory control can also be implemented to ensure efficient and secure operation of ESS keeping the charging and discharging life cycle of the devices in mind. Commonly used control algorithms in such cases are the SOC equalization algorithms which balance the SOC of an individual storage unit by comparing it with the average system SOC [33].

Authors of [34] discuss a hybrid generator with a photovoltaic energy conversion system implemented with supercapacitors and lead-acid batteries in a dc-coupled structure. The objective of this system is to supply the prescribed reactive and active power to the grid. This paper focuses on the strategy, which makes it possible to ensure a high battery state of charge and overcharge security by designing a dedicated local control system that operates on SOC signals from the storage devices. The integration of a short-term energy storage device in a doubly-fed induction generator (DFIG) design is considered to smooth the fast, wind-induced power variations. This storage feature also enhances the low voltage ride-through (LVRT) capability of the system. The authors have also proposed a composite energy storage system (CESS) that contains both high energy density storage batteries and high power density storage ultra-capacitor to meet the aforementioned requirements. A DC link topology is discussed for the storage system and an energy management scheme can actively distribute the power demand among the different energy storage.

The power sharing equations can be written as follows:

$$P_{dc} = V_{dc} I_{dc} \tag{2.1}$$

$$P_{pv} = V_{pv} I_{pv} \tag{2.2}$$

$$P_{ess} = V_{ess} I_{ess} \tag{2.3}$$

$$P_{bat} = V_{bat} I_{bat} \tag{2.4}$$

$$P_{uc} = V_{uc} I_{uc} \tag{2.5}$$

$$P_{ess} = P_{ess} + P_{ess} \tag{2.6}$$

$$P_{mismatch} = P_{dc} - P_{pv} \tag{2.7}$$

$$I_{mismatch} = \frac{P_{dc} - P_{pv}}{V_{dc}} \tag{2.8}$$

$$I_{mismatch} = I_{lf} + I_{hf} \tag{2.9}$$

where, P_{dc}, V_{dc}, I_{dc} are power, voltage and current demand on DC link; P_{pv}, V_{pv}, I_{pv} are PV power, voltage and current; P_{ess}, V_{ess}, I_{ess} are Energy Storage System power, voltage and current; P_{bat}, V_{bat}, I_{bat} battery power, voltage and current; P_{uc}, V_{uc}, I_{uc} are ultra-capacitor power, voltage and current;$P_{mismatch}$ is the difference between the power demanded at DC link and PV power, $I_{mismatch}$ is the mismatch current corresponding to mismatch power, I_{lf} , I_{hf} are the low and high frequency current references for battery and ultra-capacitor respectively.

A system consisting of a Doubly Fed Induction Generator (DFIG), dump load, and mains loads is discussed in [24]. The behavior of a hybrid energy storage unit consisting of battery storage and a supercapacitor is examined. The battery storage is designed to meet the energy requirement of the system while the supercapacitor is used to respond to rapid power fluctuations of the Remote Area Power Supply (RAPS) system. The battery storage is connected to the AC side of the system through an inverter while the supercapacitor is connected to the DC link of the back-to-back converter system of the DFIG via a two-stage bi-directional buck-boost converter. A control strategy is adopted for the hybrid energy storage system in which the operation of the battery is limited to a lower Depth of Discharge (DOD). The dump load is used to absorb excess energy in the system which cannot be utilized by the energy storage system.

Authors in [25] discuss methods to overcome the challenges of real-time simulation

of wind systems, characterized by their complexity and high-frequency switching. A hybrid flow-battery supercapacitor energy storage system (ESS), coupled with a wind turbine generator to smooth wind power is implemented in the DC link topology similar to [32]. The storage system showcases that hybrid ESS has a lower battery cost, higher battery longevity, and improved overall efficiency over its reference ESS.

A standalone ESS system is tested in [26]. This paper also presents an active hybrid energy storage system that comprises a rechargeable battery, a supercapacitor bank, and two corresponding DC/DC power converters working in tandem with a power source. The battery and the super-capacitor may be charged or discharged simultaneously with the current or power appropriately split between them. The battery may be predominant in either the charging or discharging mode. Three different control strategies for power-sharing between them are developed for the hybrid energy storage system, one of them governed by the power ratio shared by each energy storage device. In [35], advantages and drawbacks of three different arrangements for two energy sources, batteries and supercapacitors, using a bidirectional DC-DC converter are discussed. The topologies tested are DC link and Cascade topologies. Two different control solutions based on proportional-integral controllers and a low-pass filter are also discussed.

2.6.9 current and evolving trends in Power and Energy management of DC micro-grid

One article [34] discusses the problem of SOC unbalance leading to unintentional exploitation of charge cycles on storage systems. As we know by now that these storage systems come with a huge manufacturing cost and their sparing utilization is of paramount importance to maintain the operating life and efficiency of the system. The paper claims to limit the deterioration rate of storage system lifespan, especially batteries, by implementing an algorithm that takes SOC equalization into account while generating control signals for power management. The energy storage manage-

ment system based on distributed secondary level control promotes charge/discharge control which alters the energy storage unit's virtual droop resistance by looking at the difference between the micro-grid average SOC and the storage unit SOC. The SOC compensation generated from this structure is then employed in the DC bus for controlling the micro-grid operation. The paper also points to a fail-safe algorithm that ignores the hierarchical control in case of a communication error and may only result in a non-optimal solution instead of a disjoint micro-grid operation. This control structure generates a trade-off between SOC balancing speed and the SOC algorithm interference in the power management set point. Another drawback of such a control algorithm deals with a convergence factor that needs to be tuned to provide faster SOC equalization and compensate for the effects of droop mismatch.

Authors of [36] discuss voltage control of distributed dc power systems by applying droop control to share the loading between different source converters to equalize per unit contribution of power from each converter. It also analyzes the limitation of converter over-modulation as compared to the stability of the system. Stationary and dynamic properties are also investigated during load variations. Ref. [37] uses 3 wires: +170V line, -170 V line, and neutral line on the dc power line and implements load side converters instead of transformers to dispatch power. A voltage-balancer is proposed to supply for transformer-less system on the load side and maintain a high-quality power supply from the dc power line. Ref. [38] This paper investigates a DC Micro-grid configuration featuring good redundancy and high efficiency. Optimization of Micro-grid energy is distinguished between four different modes based on DC bus voltage signal. An automatic controller is proposed which switches between constant voltage operation and MPPT control, thus enabling the PV converters with regulation capabilities for conditions such as islanding mode and fully charged storage systems. The drawback of this control method is that the voltage differences between different modes cannot be too large or too small. This brings in a compromise on the system

design and size for which this control structure would work properly.

Authors of [39] propose an autonomous 3 level control strategy for dc micro-grid. Operating status is determined by monitoring the variation in common dc voltage similar to [38]. The control logic is tested for various operating conditions such as load step, generation fluctuations, islanding, grid connection, load-shedding, and generation curtailment. Article [40] discusses the use of a dc power system to supply sensitive loads and mentions general design issues regarding dc power systems. The use of dc power to supply sensitive electronic loads, which are growing in number as digitization spreads with a global influence, has lower losses in comparison with conventional ac power supply due to fewer power conversion steps. Authors of [10] have controlled the Nano-grid using dc bus signaling (DBS). The paper explains source/storage prioritization by proposing a system-wide control law based on pre-determined charging and discharging threshold realized through variations induced on dc bus voltage due to system changes.

Authors of [41] propose a method for coordination of an autonomous low-voltage direct current micro-grid using powerline signals. The control strategy uses sinusoidal signals of specific frequencies to send communication signals amongst each other. To specify different modes of operation the sinusoidal communication signal properties change and those are received by devices along with the differentiation instruction of the present or new mode of operation that needs to be undertaken. The control system is complex and highly dependent on distinguishing characteristics of the signal for understanding the current state of the system.

2.7 Power and Energy management of AC micro-grid

The management of power and energy on the AC side of the micro-grid is undertaken by power conditioning devices such as inverters. The converters utilized for micro-grid operation can be classified into three types: grid feeding, grid forming, and grid support converters [42]. Grid feeding converters are operated as current source

converters (CSC) capable of injecting real and reactive power to the grid. Voltage source converters (VSC) are used for grid forming or grid support as the amplitude and frequency of the converter voltage are dictated by the utility grid. In islanding mode grid forming converter sets the voltage and frequency references for the micro-grid in the absence of the grid [23]. Grid supporting converter include features of grid forming and grid feeding converters and hence can operate in both grid-connected as well as islanded mode of operation. Key controlling parameters to check and regulate the operation of micro-grid are voltage, frequency, active power, and reactive power. Among these parameters, the frequency can be managed by employing DC-DC converters on a DC link topology in the DC micro-grid as the frequency directly reflects as power differential on the DC side of the micro-grid. Also, all the above-mentioned parameters are conventionally controlled by inverters. Thus the converters in micro-grid are responsible for the following tasks [1], [2]:

- voltage and frequency regulation
- active and reactive power control and proper power-sharing under grid-connected mode
- seamless transition from grid-connected to islanding mode and vice-versa
- track references from optimization algorithms to enable participation in energy markets
- supply of dispatchable power within and outside of DC micro-grid including critical loads
- black start capability during grid failure or contingencies

2.7.1 Control hierarchy of AC micro-grid

AC micro-grid can be classified based on control hierarchy into:

- Primary control
- Secondary control
- Tertiary control

The primary control is responsible to ensure stabilization of the amplitude and frequency of voltage signal. Primary control is also known as local or internal control and is based exclusively on local measurements. It is responsible for adequate active and reactive power-sharing in the micro-grid [43]. The secondary control copes with the voltage and frequency deviations in the micro-grid. It operates slower than the primary control to reduce communication bandwidth and allow enough time for performing complex calculations [44]. Tertiary control manages the power flow in the micro-grid and ensures optimal power flow to enhance the overall performance of the system [45].

2.7.2 Current work in AC micro-grid

Author of [46] takes into account all the connection line parameters, effects of unknown load dynamics, nonlinearities, and unavoidable modeling uncertainties, which make sliding mode control algorithms suitable to solve the considered control problem. A decentralized second-order sliding mode control scheme, based on the suboptimal algorithm is designed for each generating unit. On similar lines, [47] combines model predictive and sliding control for current sharing in the micro-grid. Frequency and root locus-based approaches are discussed in [48]. It presents a practical control approach for efficient tuning of proportional-integral (PI) controllers and leads compensators in islanded hybrid micro-grids. It is used to minimize the frequency deviations of an AC hybrid micro-grid.

In [49], the triple droop control method for AC micro-grids is proposed to enhance the performance of power regulation, which is composed of three parts. The angle

droop and the frequency droop are adopted to control the active power in coordination, while the modified voltage droop is used to control the reactive power.

2.7.3 Evolving trends in AC micro-grid

During a disturbance in the grid, loads can be curtailed to minimize the risk of power failure. Active load management promotes consumer usage depending on prevailing conditions in the power system. Power and frequency fluctuation mitigation is possible through this approach [50]. With the increased number of renewable energy resources, the centralized EMS can provide an optimal solution with reduced complexity in communication. However, an optimal and reliable energy management goal can be met by implementing coordination between the operation of distributed and centralized control structures. Thus there is a need for a hybrid combination of distributed and centralized combination of EMS [14]. Soft switches installed in place of normally open points involve back-to-back VSC, can provide flexible active and reactive power control, voltage regulation, quick isolation from fault, and supply restoration.

CHAPTER 3: SIZING BASED OPTIMAL CONTROL ON ENERGY STORAGE FOR THE PROPOSED DC MICRO-GRID

In the literature review chapter, we discussed the various state-of-the-art control strategies implemented on micro-grids. For regulation of grid frequency using the dispatchable sources in a micro-grid, a majority of control strategies fall under the broader class of frequency-droop approach. The disadvantage of this approach is the need for knowledge of micro-grid droop characteristics. The performance of this approach deteriorates during grid dynamics and fault events as the impedance of the section of micro-grid changes and droop heavily depends on the system R/X ratio staying the same. In this chapter, an architecture that can control Hybrid Energy Storage System (HESS) integrated Photo-Voltaic Distributed Energy Resource (PVDER) (as a DC-microgrid) is proposed and implemented to regulate grid frequency by capturing voltage angle deviations ($\Delta\delta$) at the micro-grid Point of Common Coupling (PCC). The proposed architecture is an optimal controller that augments the conventional bi-directional control of the HESS and serves as a supervisor to ensure optimal dispatch of HESS for inertial support. The architecture is tested on a modified IEEE 123 bus power distribution system, where 3 DC-micro-grids are integrated at different buses using 3-phase d-q Voltage Source Inverters (VSI). It was observed that the proximity of DER from fault instance had an effect on the change in PCC angle ($\Delta\delta$) for each micro-grid and hence coordinated management of multiple DC micro-grids was possible through the proposed approach without the need of frequency-droop information of the system. Both inertial and secondary frequency responses are supported by individual DC micro-grids by locally detected ($\Delta\delta$) deviations and the demonstration shows that the architecture shows an improvement of more than 20% in comparison

to the conventional frequency-droop method.

3.1 Introduction

Due to the threat posed by climate change and global warming, renewable energy resources like wind and Photo-Voltaic (PV) are becoming popular choices where additional energy capacity is required to be installed to fulfill load demand. Renewable sources are characterized by low emission and abundance. However, the intermittent behavior of these sources introduces major operational challenges concerning grid resilience, flexibility, and power quality. To make renewable sources dispatchable, Energy Storage Sources (ESS) are introduced and operated in conjunction with them [51]. ESS together with DERs can be implemented anywhere in the grid and provide grid support functionalities such as grid ancillary services and peak load shaving [52], [53]. A range of other grid support services includes black start, energy arbitrage, voltage and frequency regulation, harmonic mitigation, non-spinning reserve, etc. [54–57]. To fulfill these functionalities the selection of energy storage must be carried out based on characteristics such as power and energy density, discharge time, response time, life, and cycle time [58–61]. Hybrid Energy Storage System (HESS) is a combination of energy storage devices that enhances the operational capabilities of an individual storage device by providing both high power and energy density. HESS can thus be used for applications such as frequency regulation. The frequency regulation curve during grid support operation can be classified into two sections: Primary frequency response (or inertial response) requiring high power density supply and Secondary frequency response (or droop response) requiring high energy density supply. The high power density supply for inertial response generally lasts for 5-20 seconds whereas the secondary response lasts between 30 seconds and 30 minutes. A combination of high power density ultra-capacitor (UC) and high energy density battery device is an ideal HESS combination to serve this purpose [62, 63].

For micro-grids, DC link topology is found to be more favorable from power-sharing

flexibility and DER integration viewpoint. [18]. It is a viable option especially when DER comprises a lot of DC sources and loads. A single inverter sufficiently integrates the entire bus to the larger grid. Studies performed with frequency regulation using DER involve a wide range of frequency-droop variants and optimization to enhance the droop action. For example, authors of [64] have a coordinated control strategy on a wind farm using energy stored in the DC capacitor for a Single Machine Infinite Bus (SMIB) system. Virtual inertia is emulated by rotor-side converter capacitance. In another work, similar inertia emulation on the DC link capacitor for a PV farm and HESS islanded micro-grid is illustrated in [65]. Whereas, in [66], virtual inertia emulation of DFIG setup commits MPPT (Maximum Power Point Tracking) reserve capacity for frequency regulation. An improved particle swarm optimization (PSO) algorithm proposed in [67] optimizes the parameters of coupling compensation and inertia for $P-\omega$ and $Q-V$ droop approach even though approximated mathematical models for micro-grid are used in these works. In [68], a decoupled frequency and voltage control approach is proposed which augments the conventional frequency-droop control for power-sharing in a stand-alone micro-grid. Battery Energy Storage System (BESS) can also be used for providing frequency damping capability and improve inertia support from PV farms along with State-Of-Charge (SOC) management cost function [69]. Electrical coupling of DC link voltage and AC frequency is discussed in [70, 71] as unified droop control where ESS supplies for dynamics on both DC link and AC link for a DC-AC micro-grid. In our earlier work, we proposed a PCC angle-based frequency regulation approach using a PVDER consisting of HESS [72]. However, that approach was based on conventional Proportional-Integral (PI) control tasked with control of the rate-of-change of the PCC voltage angle. The control method was tested for a single micro-grid and compared with the default system response.

In this chapter, a multiple DC microgrid coordinated control architecture is pro-

posed, evolved from our previous work to provide PCC angle sensitivity-based power-sharing. The approach is a novel angle minimization architecture that can provide optimal dispatch of HESS towards frequency regulation based on the proximity of unbalances or fault from the micro-grid under discussion. This approach supports both inertia and secondary frequency without requiring the knowledge of the system frequency-droop characteristics. The approach has the following advantages in comparison to the state-of-the-art frequency-droop method:

- Frequency regulation can be achieved without requiring the knowledge of micro-grid droop characteristics.
- Supports inertial and secondary frequency using locally detected voltage angle deviations.
- Proposed approach exhibits improved secondary frequency response in terms of settling time when compared with the conventional droop approach.
- Proposed approach inherently and optimally shares power among multiple DERs.
- The architecture performs well during changing grid dynamics and is sensitive to the proximity of fault location.
- Proposed architecture adopts DC-link topology and hence favorable for implementation in DC-AC hybrid systems.

The proposed approach is validated with a medium-size modified IEEE 123 bus power distribution system with 3 DERs at different locations. Two cases are studied, namely L-L-G and L-L-L-G fault. Each case is simulated at 3 different locations, bus 51, bus 18, and bus 67, respectively, and the frequency support from DERs is recorded for the proposed approach and the conventional droop approach. The chapter concludes with a quantitative summary comparing the performance of both approaches.

Table 3.1: PV model: Parameters and Specifications

Parameter	Value	Unit
Rated PV farm power	2	MW
Module Open Circuit Voltage	64.2	V
Module Vmpp	54.7	V
Module Short Circuit Current	5.96	A
Module Impp	5.58	A
Series Connected Modules	11	per string
Number of Parallel Strings	596	strings

3.2 Design of Proposed DC Micro-grid

The design and modeling details of the energy sources in the proposed micro-grid include a 2 MW PV farm, 1.2 MWh Lithium-Ion battery bank, and an 800 kW, 16 MegaJoules (MJ) ultra-capacitor, are explained below.

3.2.1 PV farm design

For the PV farm, the model of SunPower SPR-205NE-WHT-D, a 305 W PV module is used. Eleven series and 596 parallel combinations of such PV modules result in 600 V, 3.33 kA, 2MW is the PV farm. Temperature and Irradiation profiles can be given as input to the PV farm to simulate related dynamics based on real measurements. For this chapter, we only consider variations in irradiance and assume temperature to be a standard 25°C. PV module parameters used for this chapter are discussed in Table 3.1. For device-level controller design equivalent electrical circuit diagram for a PV cell is modeled as a controlled current source.

3.2.2 Battery Storage System design

The battery system used in this chapter is a 1.2 kWh battery of Lithium-Ion battery, configured for a nominal pack voltage of 600 V and 1200 Ah rated capacity. The initial state of charge is specified at 90%. The battery system is designed to be 60% of the PV farm size. The battery discharge characteristics are determined from the nominal

Table 3.2: Battery discharge characteristics

Parameter	Value	Unit
Maximum Capacity	2000	Ah
Cut-off Voltage	450	V
Fully Charged Voltage	698.39	V
Internal resistance	0.003	Ohms
Capacity at Nominal Voltage	1808.69	Ah

voltage and current parameters and shown in Table 3.2.

3.2.3 Ultra-capacitor Storage System design

An Electric Double Layered Capacitor (ELDC) is used as ultra-capacitor storage and modeled in Matlab/Simulink. The parameters are specified to define the Stern model of ultra-capacitor. In this chapter, the UC is designed for 800 kW peak instantaneous power for up to 20 seconds. UC bank is designed to 600 V of the terminal voltage. The capacitor cell selected has 12 milliohms and operates at 25°C temperature. 223 such capacitors are arranged in series to obtain a bank rating of 600 V at a total capacitance of 95 F. The energy calculation for UC amounts to 16 Mega Joules (MJ). The control voltage source E_{uc} is derived using the Stern model.

3.3 Proposed Architecture

Fig. 3.1 shows the overall architecture of the proposed Micro-grid with PV farm and energy storage sources. The power from the PV farm is managed by a unidirectional DC-DC boost converter operating in input voltage control mode. This allows the PV farm to operate at MPP and extract an efficient amount of power for the available irradiance. The boost converter also steps up the output side voltage to near 1200 V which is the DC bus. Since the micro-grid is realized in DC-link topology, we have four power converters connecting to the DC bus, namely, the PV converter discussed above, two bidirectional DC-DC converters (BDC), and a 3-phase $d-q$ Grid-Connected Voltage Source Inverter (GCVSI). The BDCs are used to regulate

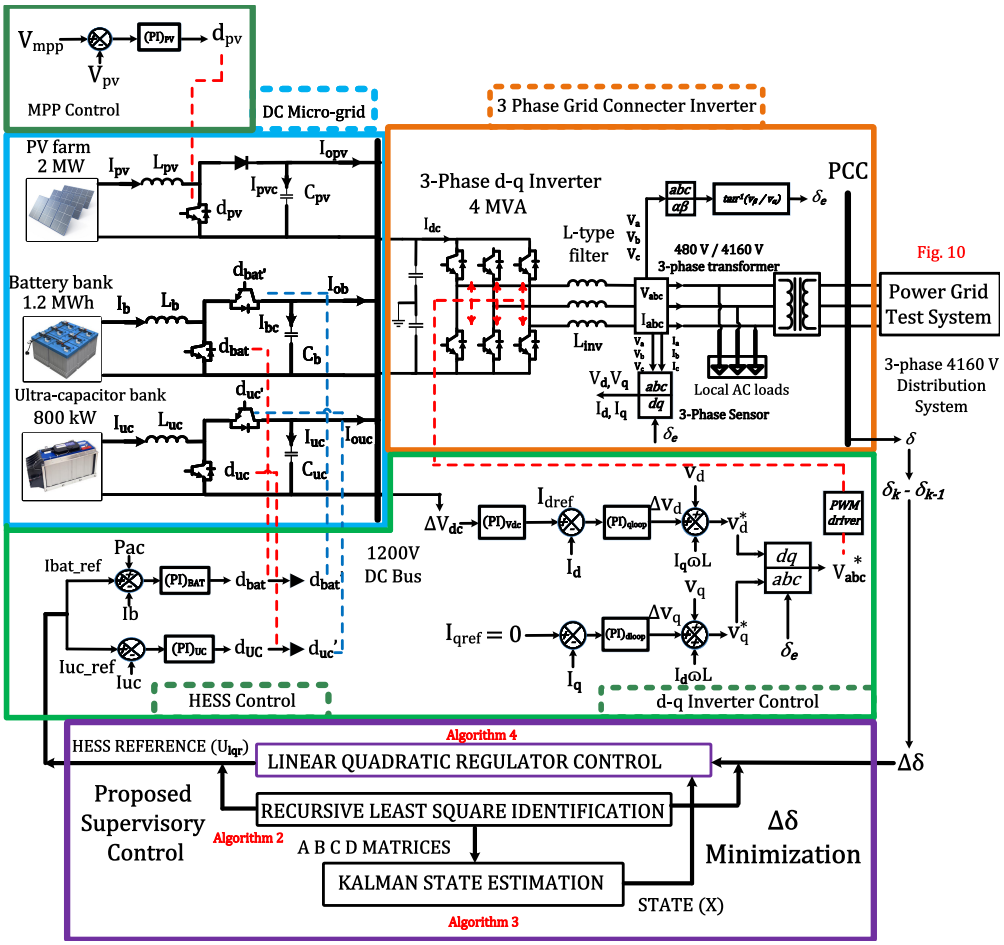

Figure 3.1: Proposed DC micro-grid.

the power flowing from HESS into the DC bus based on the outer loop grid frequency regulation. One of the advantages of operating HESS in a fully active configuration is that each source can be independently controlled and operated at optimal set-points that avoid converter throttling due to maxing of converter ramp-rate. The purpose of selecting 1200 V as DC bus rating is to enable connection of 3-phase inverter at the interfacing end. Also, the current flowing through a higher rated DC bus is lower and this contributes to a smaller size of cables and losses. Application-dependent voltage levels of local loads can also be supported by using step-down DC-DC buck converters. Three-phase GCVSI regulates the DC bus voltage at the rated 1200 V.

3.3.1 Primary level Control of Proposed DC Micro-grid

The proposed inner-loop control architecture of the DC Micro-grid is shown in fig 3.1. It consists of a 3-phase $d-q$ inverter primary level control and a hybrid energy storage system secondary level control. The control on PV farms is directed towards the successful extraction of MPP power.

3.3.1.1 Control of Non-dispatchable Source: PV farm

A PV farm is a current source and to maximize its output we use Maximum Power Point (MPP) as a reference. To achieve this we need to drive the PV plant at the Voltage (V_{MPP}) corresponding MPP using an input voltage controlled $DC-DC$ converter. A $DC-DC$ converter comprises of two filter elements and hence is defined as a second order system. Based on the volt$-$second and capacitor$-$charge balance equations for the converter the state space representation is given as

$$\begin{bmatrix} \dot{\overline{i_{pv}}} \\ \dot{\overline{V_o}} \end{bmatrix} = \begin{bmatrix} 0 & \frac{-d'_{pv}}{L} \\ \frac{d'_{pv}}{C} & \frac{-1}{RC} \end{bmatrix} \begin{bmatrix} \overline{i_{pv}} \\ \overline{V_o} \end{bmatrix} + \begin{bmatrix} \frac{1}{L} & 0 & \frac{V_o}{L} \\ 0 & \frac{-1}{C} & \frac{i_{pv}}{C} \end{bmatrix} \begin{bmatrix} \overline{V_{pv}} \\ \overline{i_o} \\ \overline{d_{pv}} \end{bmatrix} \tag{3.1}$$

$$\begin{bmatrix} V_o \\ i_{pv} \end{bmatrix} = \begin{bmatrix} 0 & 1 \\ 1 & 0 \end{bmatrix} \begin{bmatrix} \overline{i_{pv}} \\ \overline{V_o} \end{bmatrix} \tag{3.2}$$

where $\overline{V_{pv}}$ is the input side Voltage, $\overline{i_o}$ is the output side current and $\overline{d_{pv}}$ is the duty cycle input to the converter for boost operation, $\overline{i_{pv}}$, $\overline{V_{pv}}$ and $\overline{V_o}$ are inductor current, input voltage and output voltage respectively, and the states of the converter. L, C and d'_{pv} are the inductor, capacitor and the duty cycle for buck operation of the converter.

The Control-to-Input Voltage transfer function for DC-DC boost converter of the

PV farm can be derived as

$$\frac{\overline{V_{pv}}(s)}{\overline{d_{pv}}(s)} = \frac{(1-d_{pv})^2 V_o - (1-d_{pv}) L I_l s}{(LC)s^2 + (\frac{L}{R})s + (1-d_{pv})^2} \tag{3.3}$$

where V_{pv} is the small signal Input voltage, d_{pv} is the small signal duty cycle, L,C are the DC-DC converter design elements and R is the load resistance. PV control diagram from the perspective of overall architecture on DC micro-grid is shown in Fig. 3.1. Considering an uncompensated bode plot it was observed that the system has phase margin (PM) of -89.8 degrees and a negative gain margin (GM) of -55.6 dB. To exercise control a PI compensation given by equation (3.4) is derived. The PI controller transfer function is given as

$$G_c(s) = -1.5 - \frac{7}{s} \tag{3.4}$$

If we write (5.3) transfer function as a gain $G_{pv}(s)$, the closed loop PV boost converter along with the PI control can be given as

$$G_{clpv}(s) = \frac{G_{cpv}(s) G_{pv}(s)}{1 + G_{cpv}(s) G_{pv}(s)} \tag{3.5}$$

$$G_{clpv}(s) = \frac{7s^2 - 422s - 1800}{0.0001215s^3 + 7.008s^2 - 421.7s - 1800} \tag{3.6}$$

where $G_{clpv}(s)$ is the closed loop gain of the compensated system, $G_{cpv}(s)$ is the controller gain in the forward path, $G_{pv}(s)$ is the plant gain represented by transfer function given in equation (5.3). The step response showed acceptable characteristics.

3.3.1.2 Primary Level of Control - Inverter

The objective of the primary level of Control is to regulate the DC bus to its rated 1200 V set point. This is realized with the implementation of a 3-phase Grid-Connected Voltage Source Inverter (GCVSI) with a power rating of 4 MVA at the

Point of Common Coupling (PCC). The size of the inverter is calculated based on the maximum power rating of DC devices in the micro-grid such that the inverter is capable of sending through all the available DC power in the event of total DC discharge. The inverter is operated based on a $d-q$ control. Inverter angle (δ_e) and frequency information is obtained using Phase-Locked-Loop (PLL) at the grid-connected mode. The output of PLL (δ_e) is used to synchronize the ABC to d-q transformation and is shown in Fig. 3.1. The voltage balance equations for an L-type inverter can be written in state-space form and $d-q$ framework as

$$\begin{bmatrix} \dot{i_d} \\ \dot{i_q} \end{bmatrix} = \begin{bmatrix} 0 & \omega \\ -\omega & 0 \end{bmatrix} \begin{bmatrix} i_d \\ i_q \end{bmatrix} + \begin{bmatrix} \frac{1}{L_{inv}} & 0 \\ 0 & \frac{1}{L_{inv}} \end{bmatrix} \begin{bmatrix} (V_{dl} - V_d) \\ (V_{ql} - V_q) \end{bmatrix} \tag{3.7}$$

where V_{dl},V_{ql} are d-axis and q-axis voltages across inductor L_{inv}, ω is the angular frequency of the supply voltage, L is the inductance of the L-type filter, i_d, i_q and V_d, V_q are the d-axis and q-axis inverter output current and voltages respectively [73]. Active and reactive power output of the Grid Connected Inverter (GCI) can be given in $d-q$ domain as

$$\begin{bmatrix} P_{inv} \\ Q_{inv} \end{bmatrix} = \begin{bmatrix} V_d & V_q \\ V_q & -V_d \end{bmatrix} \begin{bmatrix} i_d \\ i_q \end{bmatrix} \tag{3.8}$$

During steady state grid operation we can consider voltage magnitude of grid, V_d, to be a constant. Thus the active and reactive power of the GCVSI can be controlled by controlling i_d and i_q. The transfer function of d-axis current ($\overline{i_d}$) versus ($\overline{\Delta V_d}$) can be given in Laplace domain as:

$$\frac{\overline{i_d}(s)}{\overline{\Delta V_d}(s)} = \frac{s}{L_{inv} V_d} \left(\frac{V_d + V_q}{s^2 + \omega^2} \right) \tag{3.9}$$

where ΔV_d is $V_{dl} - V_d$, s is the Laplace operator. For the specific design, the inverter transfer function can be derived as

$$G_{inv}(s) = \frac{\overline{i_d}(s)}{\overline{\Delta V_d}(s)} = \frac{s}{5.246s^2 + 5.246} \tag{3.10}$$

For the inner loop PI controller design, first the transfer function is converted into discrete (z) domain using a zero order hold (ZOH) for a simulation time step of 400 μsec. Then the system parameters are per unitized on the base of rated values. The per unitized transfer function shown in equation (3.10) is used for PI tuning to get satisfactory step response. The obtained values are K_p and K_i values of 0.86 and 0.6 respectively. The equivalent PI controller is designed as

$$G_{cinv}(s) = 0.86 + \frac{0.6}{s} \tag{3.11}$$

The closed loop transfer function will then be

$$G_{clinv}(s) = \frac{0.86s + 0.6}{5.246s^2 + 0.86s + 5.846} \tag{3.12}$$

where $G_{clinv}(s)$ is the closed loop gain of the compensated inverter system, $G_{cinv}(s)$ is the inverter controller gain in the forward path, $G_{inv}(s)$ is the inverter transfer function.

For the outer loop, (14) is used. Fig. 3.1 showcases the $d - q$ control structure applied on the inverter to exercise control on the active and reactive power of GCI.

3.3.1.3 Primary Level of Control - HESS

The HESS is modeled in a fully active configuration with separate bidirectional converters for each of its components [74]. The HESS is connected in a DC link topology along with the PV farm through DC-DC converters at 1200V DC bus. The battery is designed for a 900 kW, 1.2 MWh rating, which is 60% of the PV size,

whereas the ultra-capacitor is designed for 800 kW peak instantaneous power for up to 20 seconds. The primary level controller design is based on the state-space modeling of the DC-DC converter represented as

$$\begin{bmatrix} \dot{\bar{i}} \\ \overline{\dot{V}_{dc}} \end{bmatrix} = \begin{bmatrix} 0 & \frac{-d'_{bat}}{L} \\ \frac{d'_{bat}}{C} & \frac{-1}{RC} \end{bmatrix} \begin{bmatrix} \bar{i} \\ \overline{V_{dc}} \end{bmatrix} + \begin{bmatrix} \frac{1}{L} & 0 & \frac{V}{L} \\ 0 & \frac{-1}{C} & \frac{i}{C} \end{bmatrix} \begin{bmatrix} \overline{V_{bat}} \\ \overline{i_{dc}} \\ \overline{d_{bat}} \end{bmatrix} \tag{3.13}$$

$$\begin{bmatrix} V_{dc} \\ i \end{bmatrix} = \begin{bmatrix} 0 & 1 \\ 1 & 0 \end{bmatrix} \begin{bmatrix} \bar{i} \\ \overline{V_{dc}} \end{bmatrix} \tag{3.14}$$

where $\overline{V_{bat}}$ is the input side Voltage, $\overline{i_{dc}}$ is the output side current and $\overline{d_{bat}}$ is the duty cycle input to the converter for boost operation, $\bar{i}$, $\overline{V_{bat}}$ and $\overline{V}$ are inductor current, input voltage and output voltage respectively, and the states of the converter. L, C and d'_{bat} are the inductor, capacitor and the duty cycle for buck operation of the converter. From the above, we can obtain the transfer function of Control-to-Input Side Current as

$$\frac{\bar{i}(s)}{\overline{d_{bat}}(s)} = \frac{s\frac{V}{L} + \frac{V}{RLC} + \frac{id'_{bat}}{C^2}}{s^2 + \frac{s}{RC} + \frac{d'^2_{bat}}{LC}} \tag{3.15}$$

where $\bar{i}(s)$ is I_b and $\overline{d_{bat}}(s)$ is d_{bat} from fig 3.1. The per unit transfer function of (3.15) can be represented as

$$G_{bat}(s) = \frac{\bar{i}(s)}{\overline{d_{bat}}(s)} = \frac{s + 1.5}{s^2 + s + 0.25} \tag{3.16}$$

It was found that the above system has an infinite gain margin (GM) and 82.8 degree phase margin (PM). The system is stable by default but the step response settles to 0.856 per unit. Based on this the PI controller is desgined as

$$G_{cbat}(s) = 1.3 + \frac{3}{s} \tag{3.17}$$

Table 3.3: Controller gains after design and tuning

Control Loop	k_p	k_i
HESS Current/Power	1.3	3
Inverter d-axis current/Active Power	0.86	0.6
Inverter q-axis current/Reactive Power	-0.86	-0.6
PV MPPT	-1.5	-7
Inverter DC link regulation	-0.9	-3

The closed loop DC-DC converter plant along with the PI control can be given as

$$G_{clbat}(s) = \frac{1.3s^2 + 4.95s + 4.5}{4.3s^2 + 7.95s + 5.25} \tag{3.18}$$

where $G_{clbat}(s)$ is the closed loop gain of the compensated battery converter system, $G_{cbat}(s)$ is the controller gain, and $G_{bat}(s)$ is the battery converter transfer function. The control design is summarized in Table 3.3.

3.4 Proposed Supervisory Control

The supervisory controller in this work is designed such that the HESS delivers additional power to maintain frequency imbalances of the grid by monitoring the changes in the voltage angle ($\Delta\delta$). During power grid dynamics, frequency deviations are observed in the electrical network. In this architecture HESS and the inverter coordinate to provide additional active power to maintain the frequency. Generally, such controllers are designed through frequency-droop known as frequency regulation for both primary and secondary level responses. However, the droop approach requires considerable knowledge of micro-grid capacity and dynamics. Such a control loop heavily depends upon the appropriateness of the droop constant and they are static (gains cannot be changed with system dynamics). The proposed approach utilizes error minimization on inverter voltage angle deviations which in turn help regulate frequency. To arrive at the open-loop transfer function we will first discuss a couple

of assumptions regarding efficiencies of the power converters used in the micro-grid, namely BDCs and 3-phase d-q inverter. Considering BDC's are lossless DC power can be written as

$$P_{dc} = P_b + P_{uc}, P_{inv} = P_{dc}, V_{dc}I_{dc} = V_bI_b + V_{uc}I_{uc} \tag{3.19}$$

where P_{dc} is the total power output from BDCs at DC bus, P_b is the power input to battery BDC, P_{uc} is the power input to UC BDC, P_{inv} is the active power at the inverter output, V_{dc} is the DC bus Voltage, I_{dc} is the DC bus current, V_b is the input-side converter Voltage across battery source (battery terminal voltage), V_{uc} is the input-side converter Voltage across ultra-capacitor source (UC terminal voltage), I_b is the input-side converter current from battery source (battery terminal current) and I_{uc} is the input-side converter current from ultra-capacitor source (UC terminal current). The power transfer through an inductive line, assuming $sin(\delta) \approx \delta$ can be written as

$$P_{inv} = \frac{V_1V_2\delta}{X} \tag{3.20}$$

where P_{inv} is the 3-phase AC Active Power, V_1 is the sending end Voltage, V_2 is the receiving end Voltage, δ is the Voltage angle difference between V_1 and V_2 and X is the inductive reactance between the sending and receiving end. The state space representation of the DC-DC boost converter discussed in Section 5.3.1 gives us the relationship between Output-side Voltage and Input-side current as

$$\frac{V_{dc}(s)}{I_{bat}(s)} = \frac{s\frac{I_{in}}{C} - \frac{V_{dc}D'}{L}}{s\frac{V_{dc}}{L} + \frac{V_{dc}}{RLC} + \frac{I_{in}D'}{C^2}} \tag{3.21}$$

Using (3.19), (3.20) and (3.21) we get

$$\frac{\Delta\delta(s)}{Ibat\_ref(s)} = \frac{s\frac{XI_{dc}I_{in}}{C} + \frac{P_{dc}XD'}{L}}{s\frac{V_{dc}V_1V_2}{L} + \frac{V_{dc}V_1V_2}{RLC} + \frac{I_{in}D'V_1V_2}{C^2}} \tag{3.22}$$

where $Ibat\_ref$ is battery current reference and $\Delta\delta$ is PCC angle deviation represented in Fig. 3.1.

From the above, an eight order aggregated closed-loop transfer function is derived which can then be represented as

$$\frac{y(k)}{u(k)} = \frac{\Delta\delta(k)}{Ibat\_ref(k)} = C_{ss}(zI - A_{ss})^{-1}B_{ss} \tag{3.23}$$

where C_{ss} is the Output matrix, z is the discrete domain operator, I is the 8^{th} order Identity matrix, A_{ss} is the State Transition matrix and B_{ss} is the Input matrix of the closed loop state space representation.

3.4.1 Behavior of voltage angles during dynamics

To understand how voltage angle at the PCC changes during grid dynamics we simulate step-loading and L-G fault conditions on a modified IEEE 123 bus system. From Fig. 3.2 it can be observed that the angle (δ) at PCC decreases with increased loading on the system. Simultaneously, the grid frequency also drops. This implies that the primary and secondary response of frequency can be controlled by minimizing the rate of change of angle ($\Delta\delta$) during grid dynamics by providing power from the micro-grid. Algorithm 1 provides an overall integration methodology.

Algorithm 1 Frequency based LQR output reset

Step: 1 Collect PCC voltage angles $\delta(k)$ and $\delta(k-1)$ for current and previous time step

Step: 2 Collect grid frequency measurement at PCC, f

Step: 3 Collect Control output, U_{lqr}

If $\delta(k) \neq \delta(k-1)$ and $59.995 \geq f \geq 60.005$
Then, $U_{lqr} = U_{lqr}$
Else,
Apply 20% down the ramp on controller output,
U_{lqr} = U_{lqr} - $0.2U_{lqr}$

From the above, it can be seen that the supervisory loop is dormant when there is

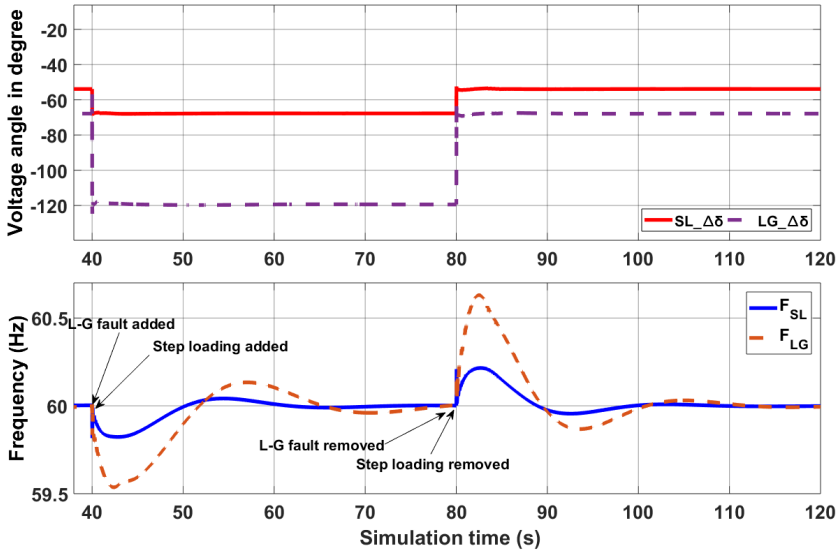

Figure 3.2: Voltage angle response to grid dynamics on Modified 123 bus system.

Algorithm 2 Recursive Least Square Identification

Step: 1 Populate matrix $X_{ls}[N \times 2n]$ with past inputs $(Ibat\_ref)$ and outputs $(\Delta\delta)$ for the observable sample window

Step: 2 Select the latest $(Ibat\_ref)$ and $(\Delta\delta)$ samples for processing in matrix $x_{ls}[1 \times 2n]$.

Step: 3 Populate Φ as matrix with output samples $(\Delta\delta)$

Step: 4 Initialize Matrices P_{ls}, K_{ls} and Θ and constant γ.

Step: 5 Calculate

$$P_{ls}(k) = \frac{[I - K_{ls}(k)x'_{ls}(k)]\, P_{ls}(k-1)}{\gamma}$$

Step: 6 Calculate

$$K_{ls}(k) = \frac{P_{ls}(k-1)x_{ls}(k)}{\gamma + x'_{ls}(k)P_{ls}(k-1)x_{ls}(k)}$$

Step: 7 Update

$$\Theta(k) = \Theta(k-1) + K_{ls}(k)\,[\Phi(k) - x'_{ls}(k)\Theta(k-1)]$$

Algorithm 3 Kalman State Estimation

Step: 1 Initialize Matrices $\hat{X_{ke}}$, P_{ke}, Q_{ke}, K_{ke}, R_{ke}, Res

Step: 2 Collect $(Ibat\_ref)$ and $(\Delta\delta)$ samples and arrange in Matrices U and y respectively, include the RLS identified state space matrices A_{ss}, B_{ss}, C_{ss}

Step: 3 Calculate the initial estimate of states $\hat{X_{ke}}$

$$\hat{X_{ke}}(k) = A_{ss}(k) \cdot \hat{X_{ke}}(k-1) + B_{ss}(k) \cdot U(k)$$

Step: 4 Calculate the Error Co-variance Estimate

$$P_{ke}(k) = A_{ss}(k) \cdot P_{ke}(k-1) \cdot A_{ss}^{T}(k) + Q_{ke}$$

Step: 5 Calculate the Kalman Gain :

$$K_{ke}(k) = \frac{P_{ke}(k) \cdot C_{ss}^{T}(k)}{C_{ss}(k) \cdot P_{ke}(k) \cdot C_{ss}^{T}(k) + R_{ke}}$$

Step: 6 Calculate the measurement residue

$$Res(k) = y(k) - C_{ss}(k) * \hat{X_{ke}}(k)$$

Step: 7 Update the Error Co-variance Estimate

$$P_{ke}(k) = [I - K_{ke}(k) \cdot C_{ss}(k)] \cdot P_{ke}(k)$$

Step: 8 Update the State Co-variance Estimate

$$\hat{X_{ke}}(k) = \hat{X_{ke}}(k) + K_{ke}(k) \cdot Res(k)$$

Algorithm 4 Linear Quadratic Regulator Control

Step: 1 Extract RLS identified state space matrices A_{ss}, B_{ss}, C_{ss} and Kalman Estimate $\hat{X_{ke}}$

Step: 2 Set $Q_{lqr}(k) = 20 \cdot C_{ss}^{T} C_{ss}$, $R_{lqr} = 0.1$ and initialize Algebraic Riccati Solution $P_{lqr}(k-1)$ and the time period of the LQR call function in simulation, T_c

Step: 3 Solve for Algebraic Riccati Equation

$$\begin{aligned} P_{lqr}(k) = [P_{lqr}(k-1) \cdot A_{ss}(k) + A_{ss}^{T}(k) \cdot P_{lqr}(k-1) \\ - P_{lqr}(k-1) \cdot B_{ss}(k) \cdot R_{lqr}^{-1}(k) \cdot B_{ss}^{T}(k) \\ \cdot P_{lqr}(k-1) + Q_{lqr}(k)] \cdot T_c + P_{lqr}(k-1) \end{aligned}$$

Step: 4 Find LQR gain K_{lqr} for k^{th} time

$$K_{lqr}(k) = R_{lqr}^{-1} \cdot B_{ss}^{T}(k) \cdot P_{lqr}(k)$$

Step: 5 The optimal control output $Ibat\_ref$ is given by:

$$Ibat\_ref(k) = -K_{lqr}(k) \cdot \hat{X_{ke}}(k)$$

no change in angle. The reset operation on the integrator is also a trigger dependent on whether grid frequency is close to regulation. To achieve an optimal solution for energy storage set point with a view of minimizing the rate of change of δ, an optimal controller evolved from the Linear Quadratic Regulator (LQR) is designed.

3.4.2 Optimal Supervisory Controller Design

Optimal controller design consists of identifying the discrete form of the transfer function in equation (30) using a measurement-based identifier and then developing a state-space representation of the power grid dynamics.

3.4.2.1 Grid Identification

Equation (3.24) is a generalized form of the 8^{th} order transfer function relationship that is identified by the Recursive Least Square Identification.

$$\frac{y(k)}{u(k)} = \frac{b_1 z^{-1} + b_2 z^{-2} + \cdots + b_n z^{-n}}{1 + a_1 z^{-1} + a_2 z^{-2} + \cdots + a_n z^{-n}} \tag{3.24}$$

where $a's$ and $b's$ are the denominator and numerator coefficients of the transfer function respectively. The numerator and denominator polynomials in terms of a's and b's from (3.24) are used to generate the A, B and C matrices (3.23) that constitute the closed-loop micro-grid state space.

Important parameters regarding the identification process that need to be chosen are the order of the system (n) to be identified and the length of the observable window (N) for which inputs and outputs need to be populated and held.

$$N = 2 \cdot n \tag{3.25}$$

where N is the length of the observable window in terms of the number of samples and n is the order of the system.

To estimate the transfer function of $\Delta\delta(k)$ with respect to LQR output $Ibat\_ref(k)$ we need to include the dynamics of BDCs and the 3-phase inverter. One BDC can be captured using a 2^{nd} order system whereas a 3-phase inverter is a 2^{nd} order system. Since we have individual BDCs for each energy storage device in our HESS, an 8^{th} order identification process should not only suffice but also be successful in capturing unknown system dynamics for the test system under study. The algorithm is shown in 2.

3.4.2.2 Grid State estimation

Grid state estimation develops the state information based on the grid identification. For an eighth-order identification, grid state estimation provides eight states. This is performed based on the Kalman State Estimation algorithm. The details of Kalman-based state estimation are illustrated in algorithm 9.

3.4.2.3 Optimal Controller

In the proposed optimal control, the discrete LQR formulation specific to our control problem is shown below:

$$J = \sum_{0}^{\infty} (\Delta\delta^T(k) \cdot Q(k) \cdot \Delta\delta(k) + Ibat\_ref^T(k) \cdot R \cdot Ibat\_ref(k)) \tag{3.26}$$

$$Q(k) = 20 * C'(k) \cdot C(k) \tag{3.27}$$

where J, is the linear-quadratic function, $\Delta\delta^T(k)$ is the transpose of the dynamically changing state of interest, Q is the static penalty factor associated with the state, $Ibat\_ref^T(k)$ is the transpose of the recursively generated optimal control and input to the plant in a closed-loop, $R = 0.1$ is the static penalty factor associated with the input, $Q(k)$ is the penalty factor for state. To implement a controller based on such dynamic quadratic optimization we need to utilize system state space that captures system parameters dynamically. This is provided by a least square-based identification process that recursively estimates and updates the state space of the system.

At the end of Algorithm 2 we get the Θ matrix which consists of dynamically changing a's and b's that form the transfer function as shown in equation (3.24). The state-space deduced using this transfer function is used to run the optimization discussed in 3.4.2 obtained from state-space representation where $A_{ss}(k)$, $B_{ss}(k)$ and

$C_{ss}(k)$ are the state transition, input and output matrices respectively. Algorithm 9 details the step-wise process of estimating the state of interest ($\Delta\delta$) from the RLS identified system. The state estimate from Algorithm 9 is used to calculate the optimal control output of LQR. LQR gain (K_{LQR}) for every sample is calculated using a 2-step process given in Algorithm 10, which gives the optimal control output, $Ibat\_ref$. The summary of the closed-loop multi-level control structure is given by frequency domain loop gain as shown in (4.26).

$$G(s) = \frac{\Delta\delta(s)}{Ib_{ref}(s)} * \frac{Ib_{ref}(s)}{d(s)} * \frac{d(s)}{Vdc(s)} * \frac{Vdc(s)}{i_d^{ref}(s)} * \frac{i_d^{ref}(s)}{\Delta V_d(s)} \tag{3.28}$$

where $\frac{Vdc(s)}{i_d^{ref}(s)} * \frac{i_d^{ref}(s)}{\Delta V_d(s)}$ represents the inverter d-q control (primary level), $\frac{Ib_{ref}(s)}{d(s)}$ is the battery current control applied by BDC in DC micro-grid, $\frac{d(s)}{Vdc(s)}$ represents the effect of input side current control on DC bus voltage and $\frac{\Delta\delta(s)}{Ib_{ref}(s)}$ describes the gain for the supervisory controller.

3.5 Proof-of-Concept Study

For the proof-of-concept study, a modified IEEE 13 bus system [75], with the proposed micro-grid with control architecture and a synchronous generator model as a source in Matlab-Simulink environment is designed. The micro-grid structure is integrated at bus 634. Fig 3.3 shows the modified IEEE 13 bus system and the Point of Common Coupling (PCC) for micro-grid. Bus 634 of the modified test system operates at 480V which makes micro-grid integration favorable. GCI is designed for a 4 MVA rating and operates at 480V at its output. Also, a synchronous generator is added with a governor control to emulate the inertial response of the generator to fault or power mismatch as shown in Fig. 3.4. fault or power mismatch. Two cases are studied. In Case 1, lines between bus 671 and 692 from Fig 3.3 are closed at 100 second simulation time to add 800 kW of 3 phase unbalanced loads. The step change in loading on the modified 13 bus system is simulated as a power mismatch. In Case

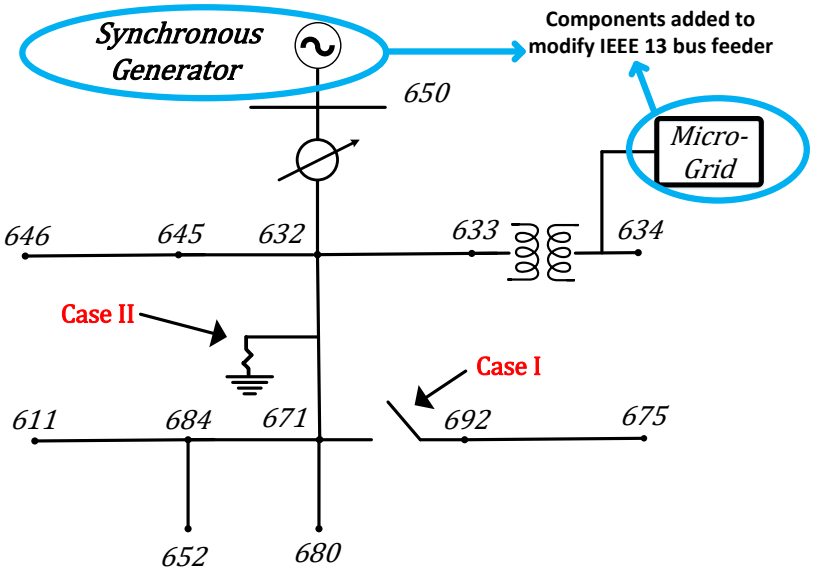

Figure 3.3: Modified IEEE 13 bus system with micro-grid and synchronous generator model.

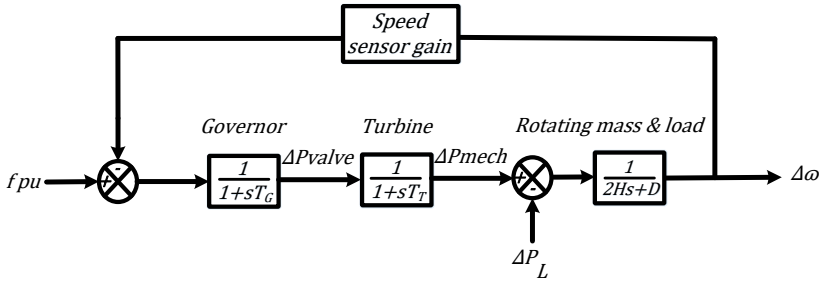

Figure 3.4: Speed Governor Control for Synchronous Generator.

2, a Line-to-Ground (L-G) fault as shown in Fig 3.3 at bus 671 is initiated.

Frequency response to LLG (Case I): In this case when a 10% step change in load is injected into the system the frequency nadir reaches 59.8 Hz for the modified 13 bus system with synchronous generator. The secondary response took about 166 seconds to settle. With the proposed micro-grid integrated architecture the frequency nadir improves to 59.87 Hz. The secondary response settles at 125 seconds, a significant improvement compared to the modified 13 bus system. In comparison to this, the HESS system reduces frequency nadir to 59.91 Hz with a settling time similar to BESS. A performance comparison between HESS and BESS indicated that the contribution of UC in reducing the frequency nadir.

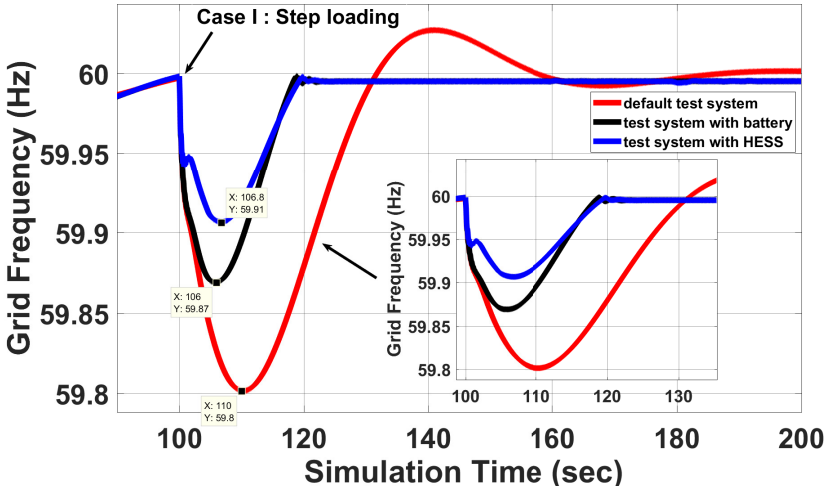

Figure 3.5: Case I : Frequency regulation for (800 kW / 10%) LLG @ 100s.

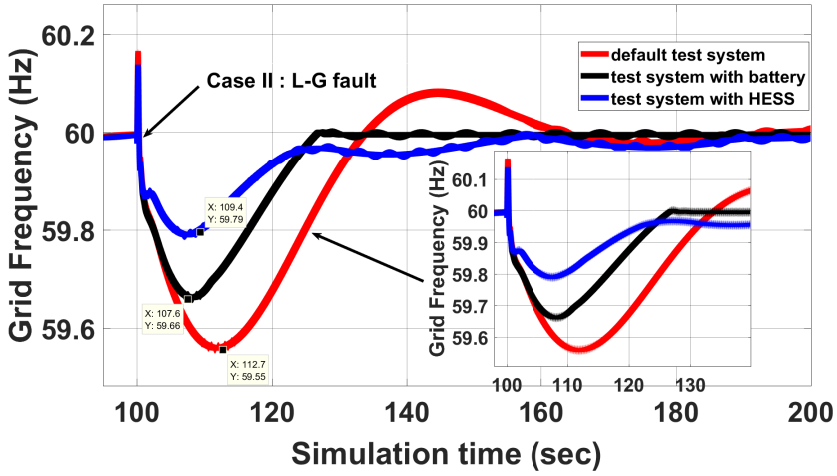

Figure 3.6: Case II : Primary and secondary frequency response for the system.

Table 3.4: Results on Modified 13 bus network

	Parameter	MBS	MBS + HESS	Imp Vs MBS
Case I	Nadir (Hz)	59.8	59.91	55%
	Settl. time (s)	166	125	41
Case II	Nadir (Hz)	59.55	59.79	53.33%
	Settl. time (s)	183	160	23

Table 3.5: Results on Modified 123 bus network

Case	Par.	MBS	MBSPA	Imp.	MBSDA	Imp.
I-A	FN (Hz)	59.52	59.58	12.5%	59.6	16.66%
bus 51	ST (s)	106	45.84	60.16	71.88	34.12
I-B	FN (Hz)	59.46	59.54	9.61%	59.55	15.38%
bus 18	ST (s)	110	46.92	63.08	69	41
I-C	FN (Hz)	59.52	59.58	12.5%	59.6	16.66%
bus 67	ST (s)	108	45.37	62.63	75	33
II-A	FN (Hz)	59.33	59.48	22.38%	59.46	19.4%
bus 51	ST (s)	120	48	72	71.91	48.09
II-B	FN (Hz)	59.32	59.48	25%	59.46	19.11%
bus 18	ST (s)	118	47.16	70.84	72	46
II-C	FN (Hz)	59.32	59.49	25%	59.45	19.11%
bus 67	ST (s)	116	47.66	68.34	69.42	46.58

Frequency response to L-G Fault (Case II): The severity of the L-G fault on the power grid is evident in Fig 3.6, where the frequency nadir is seen dropping as low as 59.55 Hz for the modified 13 bus system. The addition of HESS slightly improves frequency to 59.79 Hz as opposed to 59.66 Hz for the BESS case. The settling time for the modified 13 bus system is around 183 seconds compared to 160 seconds after HESS addition. BESS case frequency settles the earliest at about 125 seconds. Table 3.4 summarizes the case study performed on the modified 13 bus system. The following abbreviations are used during the formulation of the table: MBS is Modified Bus System; Imp. is Improvement Versus Modified Bus System. Abbreviations for Table 3.5 are: MBS is Modified Bus System, Imp. is Improvement Versus Modified Bus System, Par. is Parameter, FN is Frequency Nadir, ST is settling time, MBSPA is Proposed Approach, MBSDA is Droop Approach.

3.6 Real-Time Architecture Validation on Modified IEEE 123 bus network

The scalability of the proposed structure is tested using an IEEE 123 bus feeder [75]. This test feeder is a medium-size network with multiple load regulators and shunt

capacitors. It is characterized by spot, unbalanced loading, and switches to alternate the power-flow path. For this work, a modified IEEE 123 bus system, involving 3 micro-grids and a synchronous generator model is designed in a Matlab-Simulink environment and simulated in real-time using OPAL-RT, RT-LAB environment. The synchronous generator is added with a governor control as described in section 3.5 at bus 149 and micro-grids are integrated at buses 21, 86, and 300.

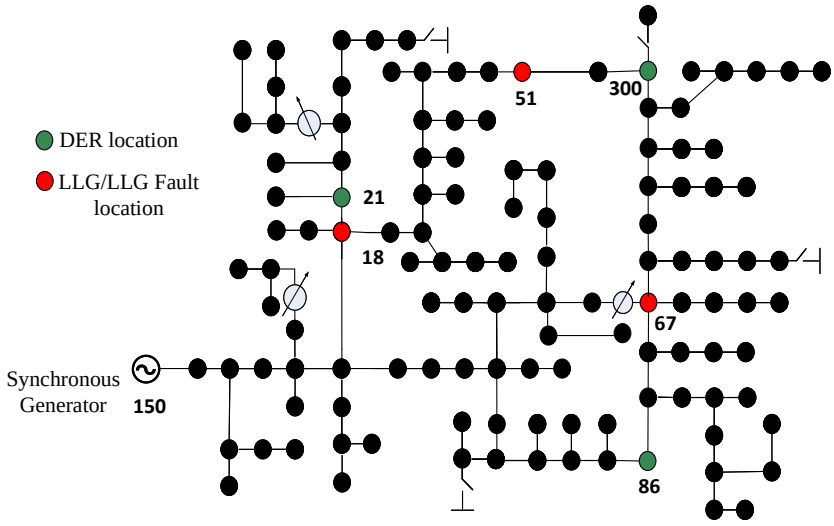

Figure 3.7: Micro-grid integration study for a 123 bus feeder

LLG (Case I) and LLLG fault (Case II) events are simulated to study the response of the proposed architecture and the power-sharing it provides for DERs. Subcases for buses 51, 18, and 67 will be defined with alphabetical suffixes A, B, and C, respectively. For each of the subcases, the effect of LLG (Case I) and LLLG fault (Case II) will be observed on ($\Delta\delta$) for every micro-grid. Further, the response of the supervisory LQR control will be recorded for each micro-grid. Thus, the contribution of micro-grids towards frequency regulation can be determined based on the proximity of the fault location. Fig 3.7 shows test cases I-A, I-B, I-C, II-A, II-B, and II-C performed on the modified 123 bus system.

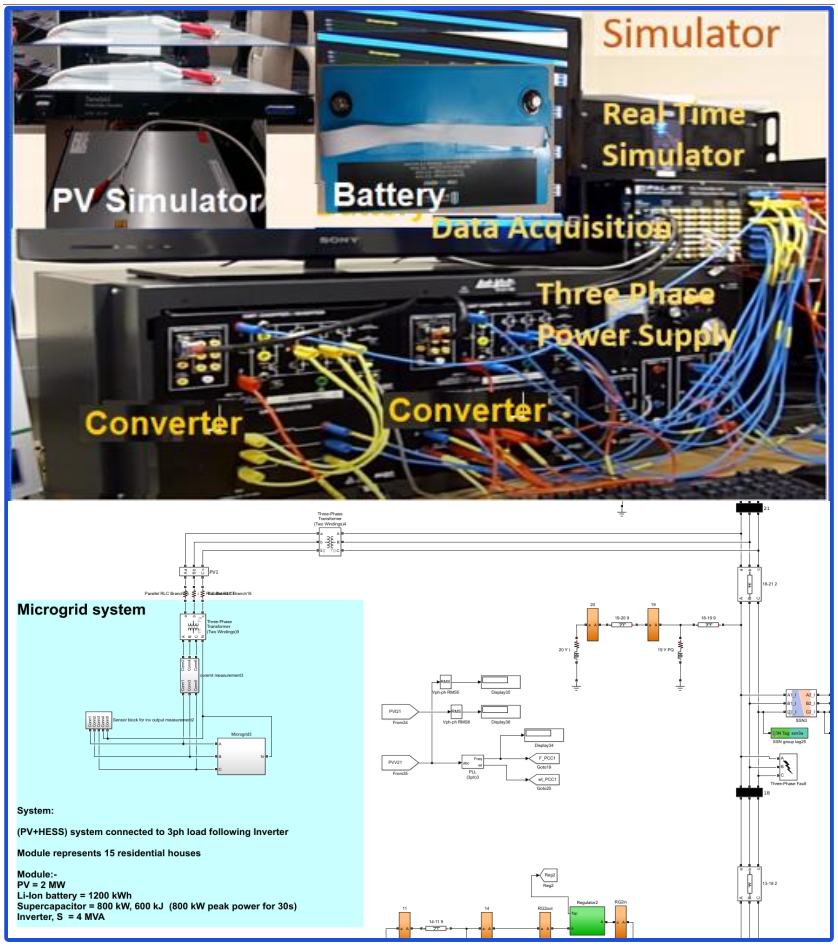

Figure 3.8: Real-Time Experimental Test-Bed.

3.6.1 Frequency response to LLG (Case I)

3.6.1.1 Fault location 51 (Case I-A)

Fig 3.9 discusses the response of the 3 micro-grids to the LLG fault on bus 51. The fault is created at 40 seconds and removed within 0.18 seconds. The first subplot shows the graphs of the rate of change of $\Delta\delta$ with respect to time on the individual micro-grid buses. It can be observed that the $\Delta\delta$ shows the maximum change for bus 300 as a reaction to the LLG fault. This is because bus 300 is closest to the fault location as compared to the other two buses. Thus, the micro-grid connected at bus 300 supplies the maximum power of 0.3775 P.U. as seen in fig 3.9. Micro-grid at bus 86 is the next closest and supplies a peak power of 0.2524 P.U. on the base of the dispatch-

able HESS which is rated at 1700 kW. Micro-grid at bus 21 is the farthest away and contributes 0.2275 P.U. power to frequency regulation. As a result of frequency support from HESS, the frequency nadir improves to 59.58 Hz in comparison to 59.52 Hz for the default system response with the synchronous generator (shown in fig 3.10). The conventional frequency-droop approach performs the best with a frequency nadir of 59.6 Hz. Whereas, the $\Delta\delta$ minimization-based PI control approach exhibits a frequency nadir of 59.56 Hz. The settling time for frequency was recorded at 106 seconds for the default system. The proposed architecture settles the fastest at 45.84 seconds whereas the conventional frequency droop settles at 71.88 seconds and the $\Delta\delta$ minimization-based PI control settles in 103 seconds. To summarize case I-A, we can state that the proposed $\Delta\delta$ minimization-based approach performs a power-sharing based on the proximity of fault location to the source supporting frequency regulation. The frequency nadirs of the proposed approach and frequency droop approach are more or less similar. But the proposed approach settles the frequency fastest.

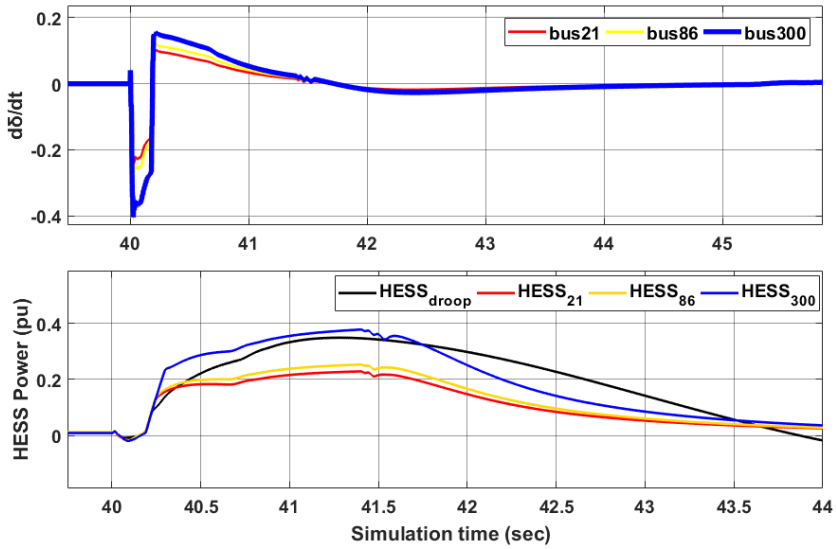

Figure 3.9: Case I-A : DER HESS Power sharing based on $\Delta\delta$ minimization

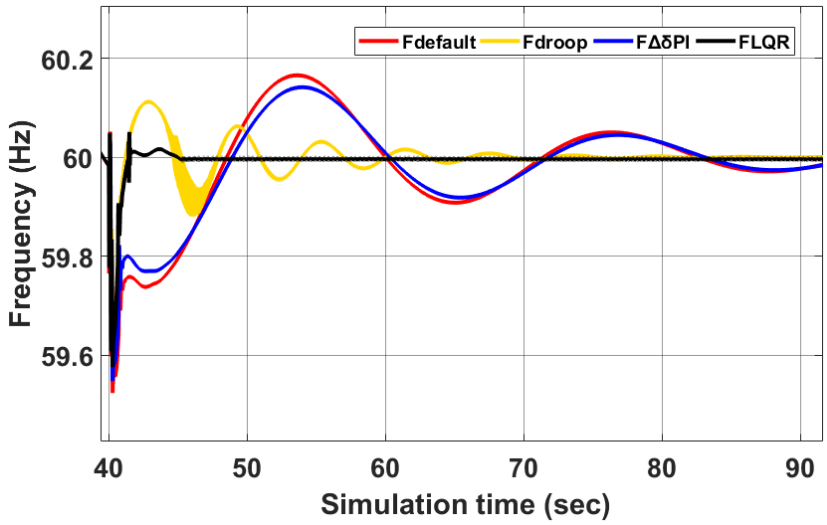

Figure 3.10: Case I-A : Primary and Secondary Frequency Response for various control approaches

3.6.1.2 Fault location 18 (Case I-B)

For Case I-B, a fault is initiated on bus 18 at 40 seconds of simulation time. The response recorded for the micro-grids and the frequency responses for the default system, conventional frequency-droop, and $\Delta\delta$ based PI and LQR approach is detailed in 3.10. The effect of the fault on bus 18 is the least on the rate of change $\Delta\delta$ of bus 86 and the most on $\Delta\delta$ of bus 21. Consequently, the micro-grid on bus 21 supplies the maximum 0.32 P.U power whereas the micro-grid at bus 86 commits the least of them with 0.2404 P.U. of peak power for frequency regulation. After supporting the inertial response the proposed LQR approach gradually reduces the power contribution from all the micro-grid as soon as the frequency reaches close of regulation. As a result of which the settling time for the secondary response is fastest at 46.92 seconds. Fig 3.10 shows settling time for frequency for different approaches. The conventional frequency-droop approach settles second fastest in 69.42 seconds, whereas, the $\Delta\delta$ based PI control takes 102 seconds. The default system settling time due to synchronous generator inertia is 110 seconds.

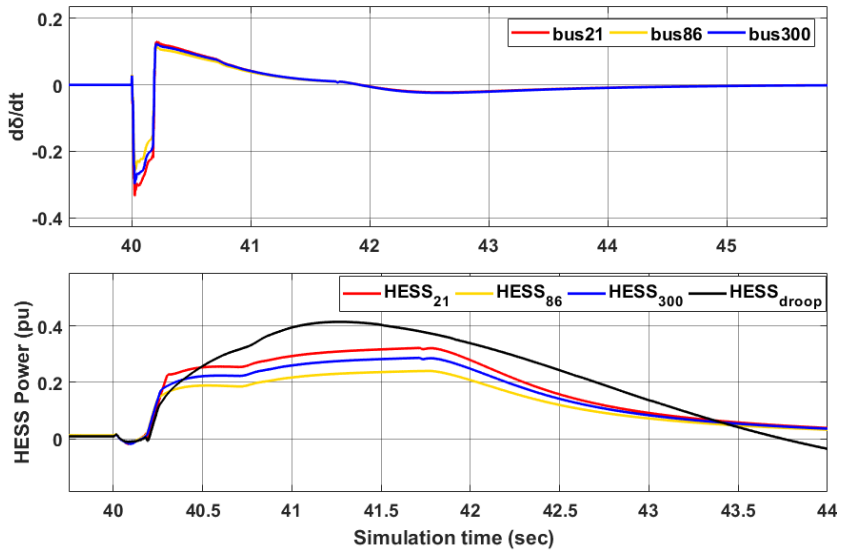

Figure 3.11: Case I-B :DER HESS Power sharing based on $\Delta\delta$ minimization

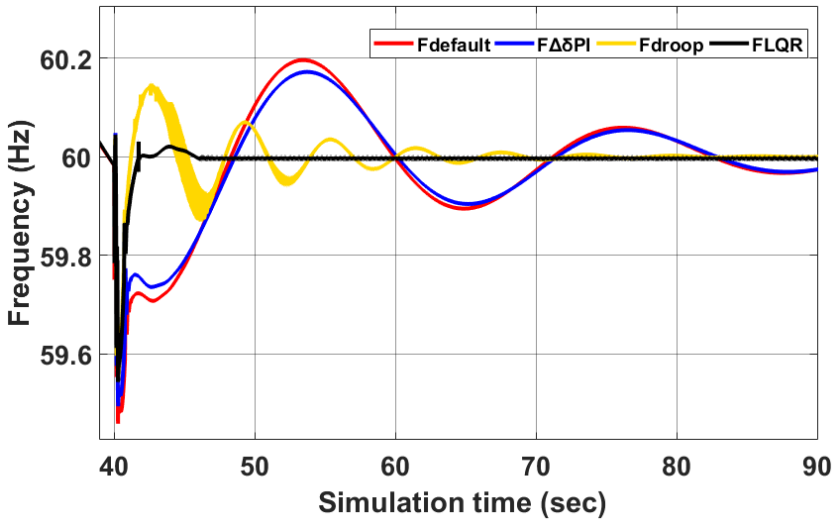

Figure 3.12: Case I-B : Primary and Secondary Frequency Response for various control approaches

3.6.1.3 Fault location 67 (Case I-C)

In this case, the micro-grids at buses 86 and 300 experience a greater effect of the fault as compared to the micro-grid on bus 21. However, this time the fault location is farther away from bus 21 than that in case II-B. As a result of this, the micro-grid supplies 0.2 P.U. power while contributing to frequency regulation from bus 21. The maximum power of 0.34 P.U. and 0.29 P.U. is committed by buses to 86 and 300 respectively due to their proximity to the fault location. Frequency nadir for the conventional frequency-droop approach shows the best result at 59.6 Hz, whereas that for the proposed approach improves to 59.54 Hz. Based on this result the frequency-droop approach performs better for this case. However, the settling time for the proposed approach is recorded at 45.37 seconds whereas the frequency-droop approach settles 20 seconds later at 75 seconds. The default inertial response of the synchronous generator settles the slowest at 108 seconds.

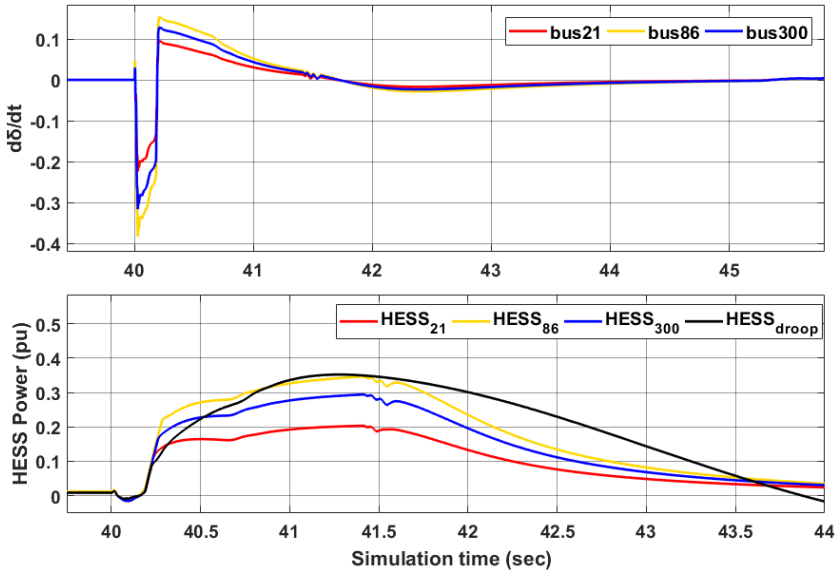

Figure 3.13: Case I-C :DER HESS Power sharing based on $\Delta\delta$ minimization

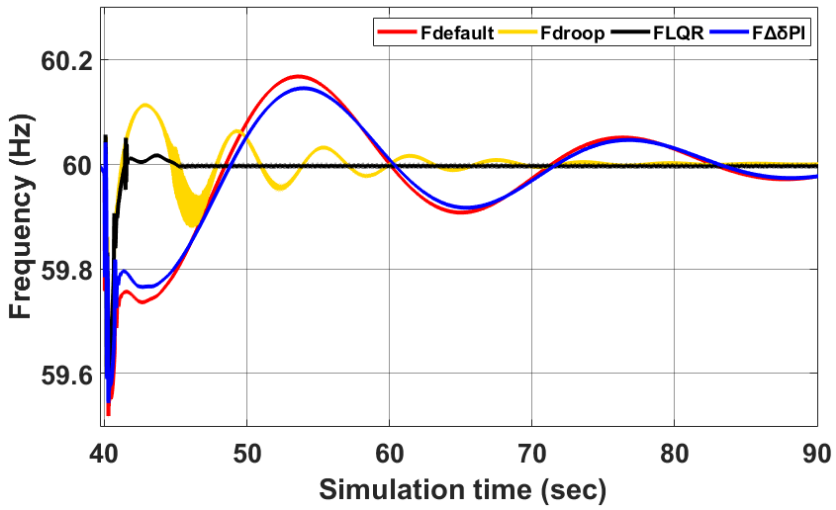

Figure 3.14: Case I-C : Primary and Secondary Frequency Response for various control approaches

3.6.2 Frequency response to LLLG fault (Case II)

3.6.2.1 Fault location 51 (Case II-A)

Fig 3.16 discusses the response of the 3 micro-grids to LLLG fault on bus 51. The fault is created at 40 seconds and removed within 0.18 seconds. The first subplot shows the graphs of the rate of change of $\Delta\delta$ with respect to time on the individual micro-grid buses. It can be observed that the $\Delta\delta$ shows the maximum change for bus 300 as a reaction to the LLLG fault. This is because bus 300 is closest to the fault location as compared to the other two buses. Thus, the micro-grid connected at bus 300 supplies the maximum power of 0.99 P.U. as seen in fig 3.16. Micro-grid at bus 86 is the next closest and supplies a peak power of 0.8522 P.U. on the base of the dispatchable HESS which is rated at 1700 kW. Micro-grid at bus 21 is the farthest away and contributes 0.62 P.U. power to frequency regulation. As a result of frequency support from HESS, the frequency nadir improves to 59.48 Hz in comparison to 59.33 Hz for the default system response with the synchronous generator. The conventional frequency-droop approach results in a frequency nadir of 59.46 Hz. Whereas, the $\Delta\delta$ minimization-based PI control approach exhibits a frequency nadir of 59.44 Hz.

The settling time for frequency was recorded at 120 seconds for the default system. The proposed architecture settles the fastest at 48 seconds whereas the conventional frequency droop settles at 72 seconds and the $\Delta\delta$ minimization-based PI control settles in 84 seconds. To summarize case II-A, we can state that the proposed $\Delta\delta$ minimization-based approach performs a power-sharing based on the proximity of fault location to the source supporting frequency regulation. The frequency nadirs of the proposed approach and frequency droop approach are more or less similar. But the proposed approach settles the frequency fastest.

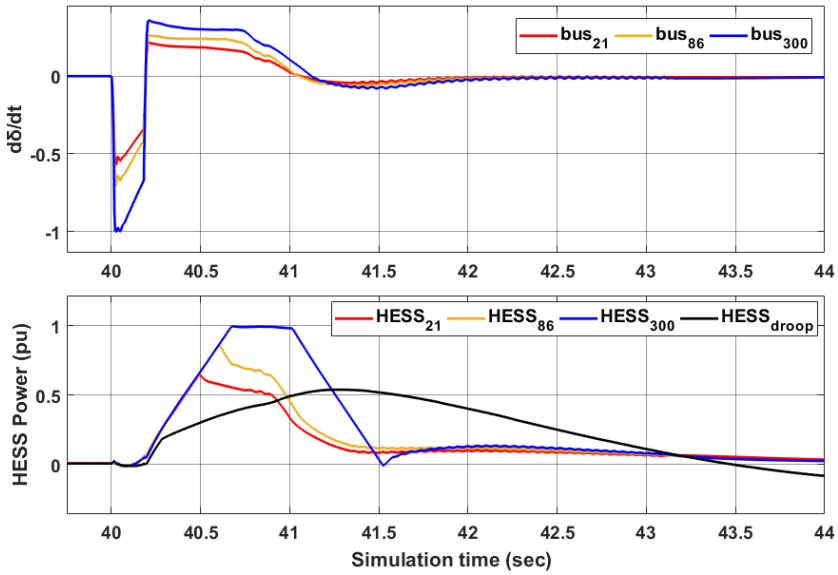

Figure 3.15: Case II-A :DER HESS Power sharing based on $\Delta\delta$ minimization

3.6.2.2 Fault location 18 (Case II-B)

For Case II-B, a fault is initiated on bus 18 at 40 seconds of simulation time. The response recorded for the micro-grids and the frequency responses for the default system, conventional frequency-droop, and $\Delta\delta$ based PI and LQR approach is detailed in fig 3.16. The effect of the fault on bus 18 is the least on the rate of change $\Delta\delta$ of bus 86 and the most on $\Delta\delta$ of bus 21. Consequently, the micro-grid on bus 21 supplies the maximum 0.9858 P.U power whereas the micro-grid at bus 86 commits the least of them with 0.6721 P.U. of peak power for frequency regulation. After

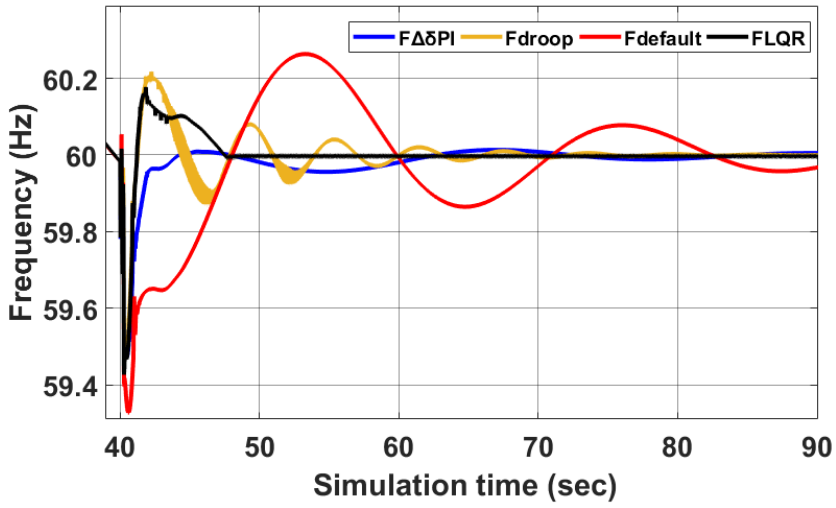

Figure 3.16: Case II-A : a) Primary and Secondary Frequency Response

supporting the inertial response the proposed LQR approach gradually reduces the power contribution from all the micro-grid as soon as the frequency reaches close of regulation. As a result of which the settling time for the secondary response is fastest at 47.16 seconds. Fig 3.16 shows settling time for frequency for different approaches. The conventional frequency-droop approach settles second fastest in 72 seconds, whereas, the $\Delta\delta$ based PI control takes 102 seconds. The default system settling time due to synchronous generator inertia is 118 seconds.

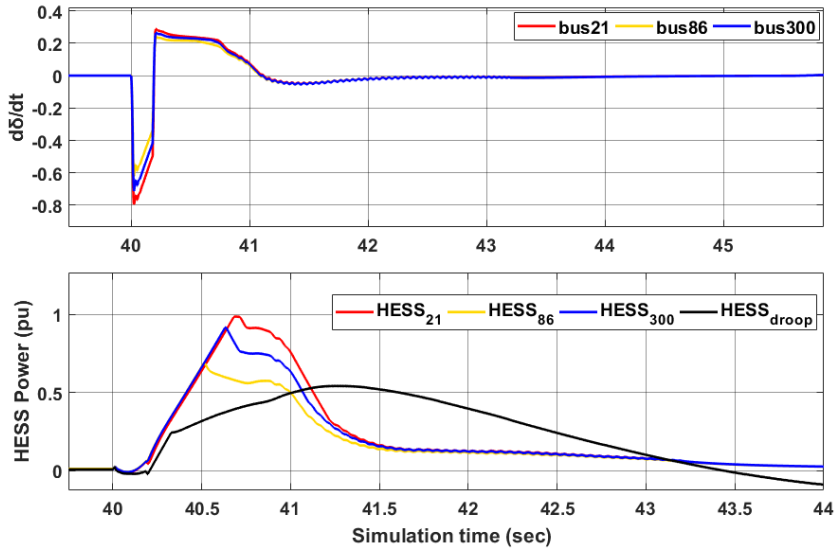

Figure 3.17: Case II-B :DER HESS Power sharing based on $\Delta\delta$ minimization

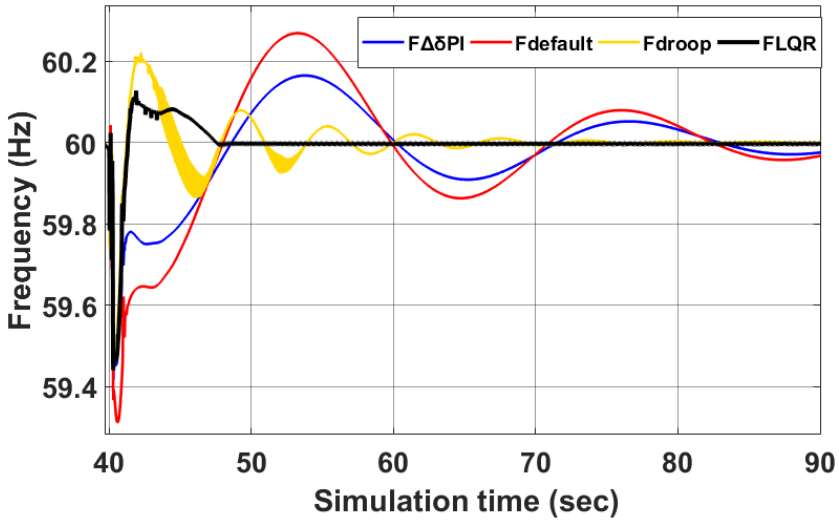

Figure 3.18: Case II-B : Primary and Secondary Frequency Response for various control approaches

3.6.2.3 Fault location 67 (Case II-C)

Fig 3.19 and fig 3.20 summarize the response of various control approaches to a fault at bus 67. In this case, the micro-grids at buses 86 and 300 experience a greater effect of the fault as compared to the micro-grid on bus 21. However, this time the fault location is farther away from bus 21 than that in case II-B. As a result of this, the micro-grid supplies 0.536 P.U. power while contributing to frequency regulation from bus 21. The maximum power of 0.937 P.U. and 0.93 P.U. is committed by buses 86 and 300 respectively due to their proximity to the fault location. Frequency nadir for the proposed approach shows the best result at 59.49 Hz, whereas that for the frequency-droop approach improves to 59.45 Hz. Based on this result the performance for both approaches is comparable. However, the settling time for the proposed approach is recorded at 47.66 seconds whereas the frequency-droop approach settles 22 seconds later at 69.42 seconds. The default inertial response of the synchronous generator settles the slowest at 116 seconds.

To summarize, it can be noted that the proposed approach does power-sharing based on fault proximity. The conventional frequency-droop approach shares power

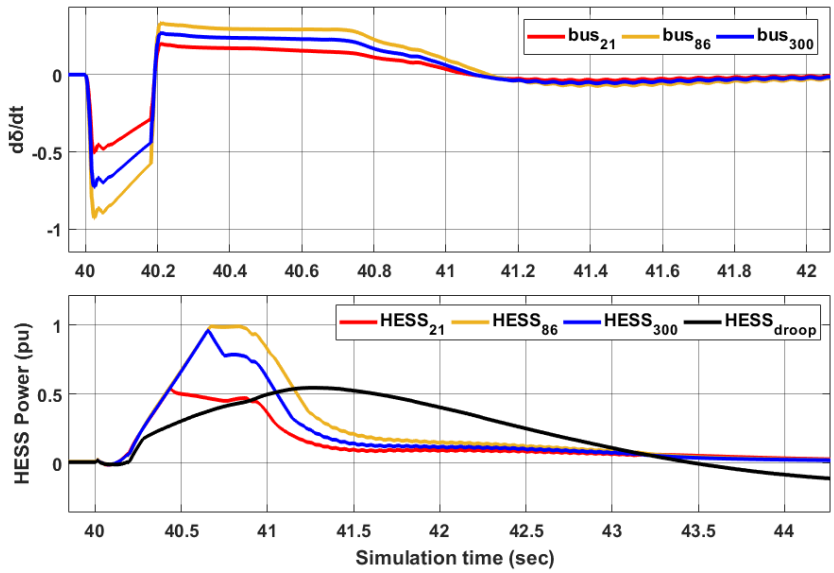

Figure 3.19: Case II-C :DER HESS Power sharing based on $\Delta\delta$ minimization

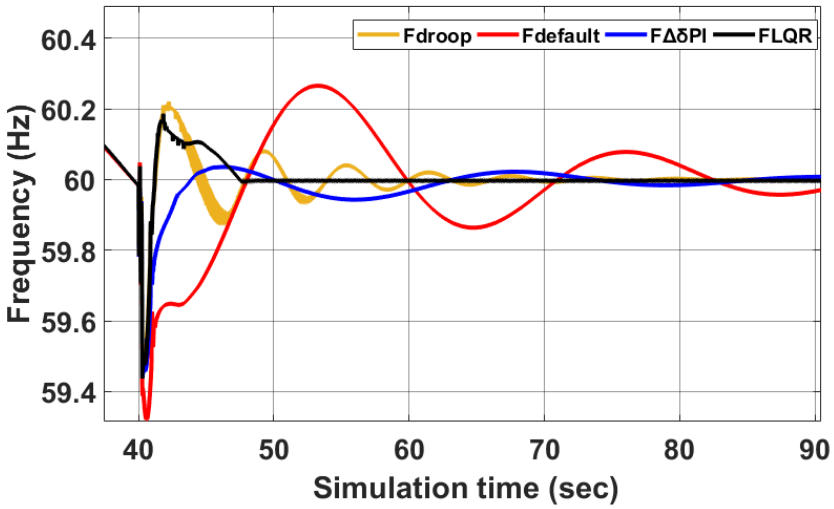

Figure 3.20: Case II-C : Primary and Secondary Frequency Response for various control approaches

equally as it uses frequency which is common throughout the distribution system. Frequency nadir is comparable for both approaches. However, the proposed approach has a faster settling time due to a more optimized power-sharing between micro-grids that comes inherently with the approach. Table 5.1 showcases the result for the modified 123 bus system. The medium size test system performs well for all the cases with the proposed approach with the added advantage of fault proximity-based optimum power-sharing and faster settling time.

3.7 Summary of Sizing Based Optimal Control on HESS

This chapter highlights the advantages of the proposed control architecture and validates its real-time implementation and scalability on the modified IEEE 123 bus system. The proposed DER control topology enables dispatch-able operation using a 3-phase load following GCI for improved inertial and secondary frequency response. The ancillary service for frequency regulation provided by the architecture only needs the rate of change of PCC angle to determine the contribution of micro-grid connected at PCC. Power-sharing determined by the minimization routine is based on the relative angle sensitivity at PCC. Unlike, frequency-droop approach the proposed architecture shares power depending on the proximity of fault/dynamics location from the micro-grid of interest. The inertial response of both approaches was found to be comparable but the proposed architecture shows an improvement in the frequency settling response. Such architecture is favorable for multiple DERs connected in DC-AC topology due to the inherent power-sharing capability of the approach and also with the added advantage that the control signals of individual micro-grids are invulnerable to external network dynamics.

CHAPTER 4: INVERTER ANGLE MINIMIZATION BASED CONTROL APPROACH FOR DISPATCH OF DISTRIBUTED ENERGY RESOURCES WITH FULLY ACTIVE HYBRID ENERGY STORAGE SYSTEM

This chapter proposes a novel frequency regulation approach that is based on Point of Common Coupling (PCC) voltage angle minimization for Distributed Energy Resources (DERs) connected in a micro-grid. The proposed DER micro-grid system consists of a Photo-Voltaic (PV) DER comprising of a fully active Hybrid Energy Storage System (HESS) comprising of battery and ultra-capacitor. All the devices of the DER are connected in a DC topology with a common DC link that feeds into a three-phase d-q controlled voltage source inverter (VSI). The VSI is further connected to a modified IEEE 123 bus distribution system. The proposed method is capable of identifying and differentiating grid dynamics from the steady-state condition by looking at the deviation of voltage angle at DER interconnection bus ($\Delta\delta$). It further distributes power setpoints amongst the available dispatch-able resources based on their proximity to the grid dynamic location. To implement control using this concept, an optimal control approach of the Linear Quadratic Regulator (LQR) is used. The optimal control quality function is aimed at minimizing $\Delta\delta$ during grid dynamic conditions. In this process, the controller provides optimal dispatch of HESS with the objective of regulating grid frequency. The proposed approach support inertial and secondary frequency response through locally controlled PV DERs and without requiring the knowledge of the distribution system's frequency-droop characteristics.

4.1 Introduction

The dramatic rise of renewable energy technology has paved the way for smart grid operations using distributed energy resources. Technologies harnessing solar and wind energy are at the forefront of this energy industry revolution. These technologies, however, come with the drawback of being intermittent and costly. To enable customer participation in smart grid operations, energy storage device augmentation to the distributed renewable energy sources like solar and wind has proved to be an immediate solution for intermittence. Thus energy storage devices have become a key component in the planning and installation of renewable energy technology. The choice of Energy Storage Systems (ESS) depends on the type of service they operated for. Design of ESS can also be dictated by two distinct frequency regulation operations: Inertial response of grid frequency (primary response) [76] and steady-state frequency regulation (secondary response) [77]. HESS has an advantage over conventional storage systems because they can support a wide range of load demands and hence can be effective in supplying for primary and secondary frequency regulation [78].

Control of such dispatch-able HESS devices can be achieved by a variety of control approaches. One such widely used control approach is the least square-based error minimization. The Linear Quadratic Regulator (LQR) falls in this category. LQRs are generally implemented in multi-structure and complex environments where multiple parameters determine the state of operation of the system. Some applications also see LQRs implemented on a single non-complex system, but the output is required in a control action that depends on a set of functions. These function sets form the quality function that needs to be minimized. For example: [79] presents a multi-functional single-stage residential photovoltaic power supply based on a linear quadratic regulator (LQR). The system makes use of a single-phase power converter connected to the grid through an LCL filter. A robust LQR with added integral

action (LQRI) controller is designed to incorporate added functions such as a power line conditioner, an active power regulator, and a voltage stabilizer. LQR designs are also prominent among automated systems. Authors of [80] discuss the design of the LQR controller for intelligent control of Quadrotor helicopter. They emphasized the linearized state modeling of the quadrotor helicopter, the system's performance index (weighting matrices), the feedback gain matrix (K), and the tuning based on these gains. General applications of LQR deal with Multi-Agent Systems (MAS). LQR based consensus scheme for state updates of heterogeneous multi-agent robotic systems (MASs) for the cooperative accomplishment of tasks is proposed in [81]. Articles [82], [83], [84] and [85] are some other variants of LQR (MAS) applications. Thus LQR approaches are favorable for the control of multiple ESS devices within a HESS structure.

DC link topology enjoys the advantages of being flexible for power-sharing amongst multiple DERs and their easy integration into the micro-grid [18]. Similarly, HESS can also be integrated into a common inverter in conjunction with DERs. Literature review related to frequency regulation discusses the relationship between power and phase angle (P$-\delta$) [86] using the concept of self-synchronized $d-q$ inverter. A drawback of such an approach is the reliance on frequency-droop characteristics which change with dynamics in the distribution system. On similar lines, active power-frequency control (P$-\omega$) [87] and reactive power-voltage control (Q$-V$) [88] are heavily reliant on successfully identifying the frequency-droop response of the DERs.

Article [89] discusses a reduced-order-based wind turbine control. Examples of droop control using Virtual Synchronous Generator (VSG) based inverter representation for frequency-droop control can be studied in [90] and [91] for multi-level converter operation. Even HESS has been used with VSG for inertial response [92], but that study has been done in islanded condition.

4.2 Research Contributions

The approach proposed in this optimal control manages multiple DERs by observing and controlling voltage angle deviations ($\Delta\delta$) at each DER PCC. It has the following advantages due to the way this architecture is implemented:

- Balance and regulation of frequency is achieved by managing multiple HESS
- Regulates grid frequency by controlling PCC voltage angle deviations ($\Delta\delta$) for each DER.
- Assigns power setpoints between dispatch-able devices based on their proximity to the grid dynamic location
- Works locally and independent of distribution system's droop information, thus equally effective even after changes in micro-grid impedance.

4.3 Proposed DC Micro-grid Design

DER is sized for a maximum instantaneous power of 3.7 MW. It comprises a 2 MW SunPower SPR-205NE-WHT-D PV farm. HESS is made up of a 1.2 MWh Lithium-Ion battery as the energy density device and an 800 kW, 16 (MJ) capacity ultra-capacitor (UC) bank as the power density device. The UC is designed based on Stern model specifications such that it is capable of providing 800 kW peak instantaneous power for a maximum of 20 consecutive seconds. All the devices are designed for 600 V terminal voltages. Each device has its DC-DC converter to exercise fully independent control of power from each one of them. The output side of all converters is rated at 1200 V DC and they feed power to a common DC bus. A 3-phase $d-q$ Grid-Connected Voltage Source Inverter (GCVSI) interfaces the DER to the modified 123 bus distribution system.

Fig. 4.1 presents the design and control architecture of the micro-grid. The micro-grid is designed in a DC topology. The DC bus connects to 3 power converters.

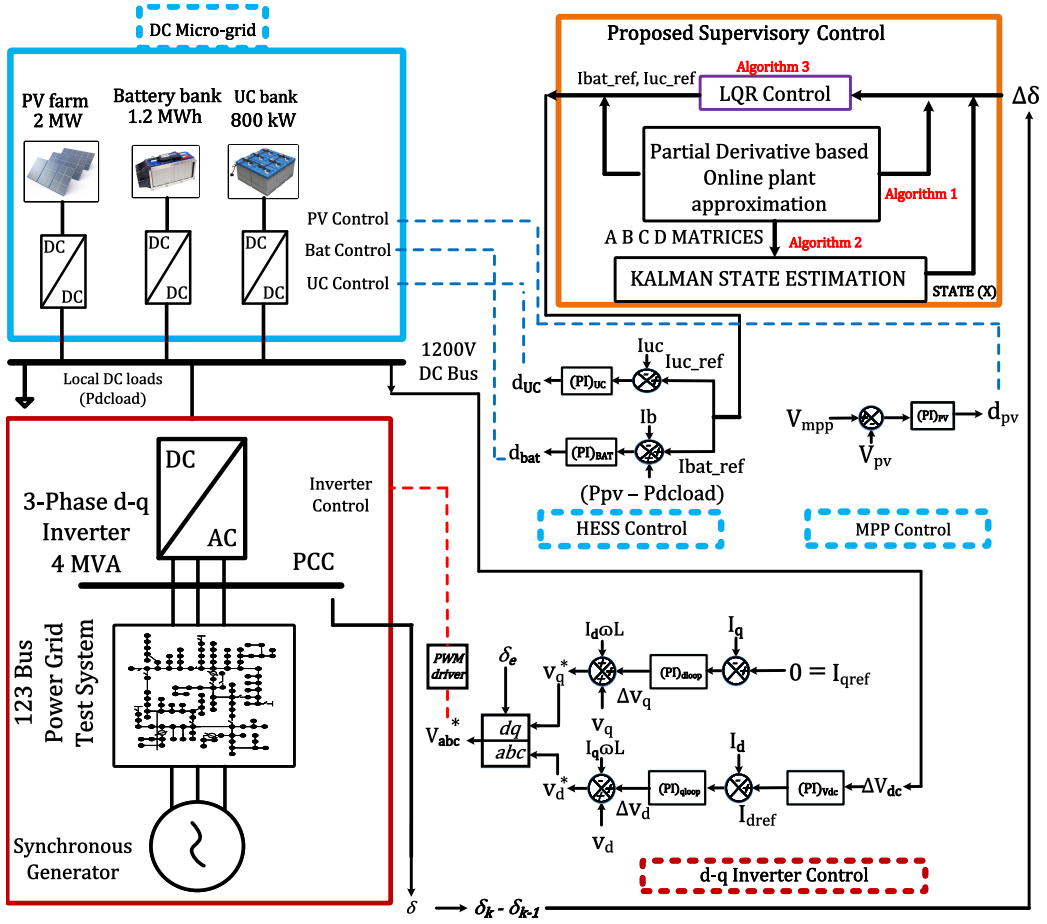

Figure 4.1: Proposed DC micro-grid and Control Architecture.

A uni-directional boost converter is operated in input-side voltage control mode to enable PV farm track maximum power (MPPT) based on its input irradiance. This operation simultaneously steps up the PV terminal voltage from 600 V to 1200 V at the converter output side for DC bus integration. Non-isolated bidirectional DC-DC converters each for battery and ultra-capacitors (UC) are operated in input current control mode to allow control of power output from individual storage devices. The 3-phase $d-q$ GCVSI is responsible for maintaining DC bus Voltage at 1200 V. The proposed supervisory control is based on LQR control. The states for LQR control are identified online using a partial derivative-based plant approximation. This approach makes use of online measurement values from DER systems. The measurement values replace the variables in the theoretical equations of the state

space and their partial derivatives help us approximate the state space of the system online. LQR minimization develops a quality function that aims at mitigating the PCC voltage angle deviations ($\Delta\delta$) during grid dynamics. The supervisory control produces optimal set-points for micro-grid power dispatch that ensures frequency regulation and power-sharing based on the proximity of each DER from the grid dynamic location.

4.3.1 Control of PV farm

The micro-grid PV farm is considered as a conventional PV source (current source with Maximum Power Point (MPP) as a reference). A small signal model of the PV farm can be represented as follows:

$$\begin{bmatrix} \dot{\overline{i}} \\ \dot{\overline{V}} \end{bmatrix} = \begin{bmatrix} 0 & \frac{-D'}{L} \\ \frac{D'}{C} & \frac{-1}{RC} \end{bmatrix} \begin{bmatrix} \overline{i} \\ \overline{V} \end{bmatrix} + \begin{bmatrix} \frac{1}{L} & 0 & \frac{V}{L} \\ 0 & \frac{-1}{C} & \frac{i}{C} \end{bmatrix} \begin{bmatrix} \overline{V_{pv}} \\ \overline{i_o} \\ \overline{D_{mpp}} \end{bmatrix} \tag{4.1}$$

$$\begin{bmatrix} V \\ i \end{bmatrix} = \begin{bmatrix} 0 & 1 \\ 1 & 0 \end{bmatrix} \begin{bmatrix} \overline{i} \\ \overline{V} \end{bmatrix} \tag{4.2}$$

MPP control design can be performed based on the control-to-input voltage transfer function for DC-DC boost converter of the PV farm as follows

$$G_{pv}(s) = \frac{\overline{V_{pv}}(s)}{\overline{D_{mpp}}(s)} = \frac{(1 - D_{mpp})^2 V_o - (1 - D_{mpp}) L I_l s}{(LC)s^2 + (\frac{L}{R})s + (1 - D_{mpp})^2} \tag{4.3}$$

where V_{pv} is the small signal Input voltage, D_{mpp} is the small signal duty cycle, L, C are the DC-DC converter design elements and R is the load resistance. A closed loop transfer function with controller as a $G_{cpv}(s)$, can be represented as

$$G_{clpv}(s) = \frac{G_{cpv}(s) G_{pv}(s)}{1 + G_{cpv}(s) G_{pv}(s)} \tag{4.4}$$

where $G_{clpv}(s)$ is the closed loop gain, $G_{cpv}(s)$ is the PV controller gain, $G_{pv}(s)$ is the plant gain represented in equation (4.3). From (4.4), the MPP controller can be designed.

4.3.2 Control of dispatch-able HESS

The HESS is modeled in a fully active configuration [74]. They are connected to the DC bus along with the PV farm through DC-DC converters. The energy storage converters link DC micro-grid devices and inverter. HESS employs bi-directional converters to control the power outputs from each of the dispatchable devices.

The transfer function for battery primary level control is given in equation (4.5).

$$\frac{\bar{i}(s)}{\overline{d}(s)} = \frac{s\frac{V}{L} + \frac{V}{RLC} + \frac{iD'}{C^2}}{s^2 + \frac{s}{RC} + \frac{D'^2}{LC}} \tag{4.5}$$

Power control loop for HESS is detailed in Fig. 4.1. Table 4.1 summarizes the tuned controller values for the inner loops of DER converters.

4.3.3 3- Phase $d-q$ Inverter Control

Primary level inverter control is assigned to regulate the DC bus to 1200 V. The inverter is sized depending upon the maximum instantaneous power capacity of DC devices in the micro-grid such that the inverter can send through all the available DC power in the event of total DC discharge. The inverter is operated using $d-q$ control law. Inverter angle (δ_e) and frequency information is obtained using a Phase-Locked-Loop (PLL). PCC voltage used for generation of PLL angle is added with a random measurement noise (maximum of 5%) and the PLL operation is tested before and after the fault. It was found that the PLL angle remains unaffected despite adding measurement noise to PCC voltage. Also, the PLL output did not show any variation to the unbalanced fault condition. Fig 4.2 shows the test result on PLL. PLL output (δ_e) is used to synchronize the abc to d-q transformation. The PLL system is shown in Fig. 4.3.

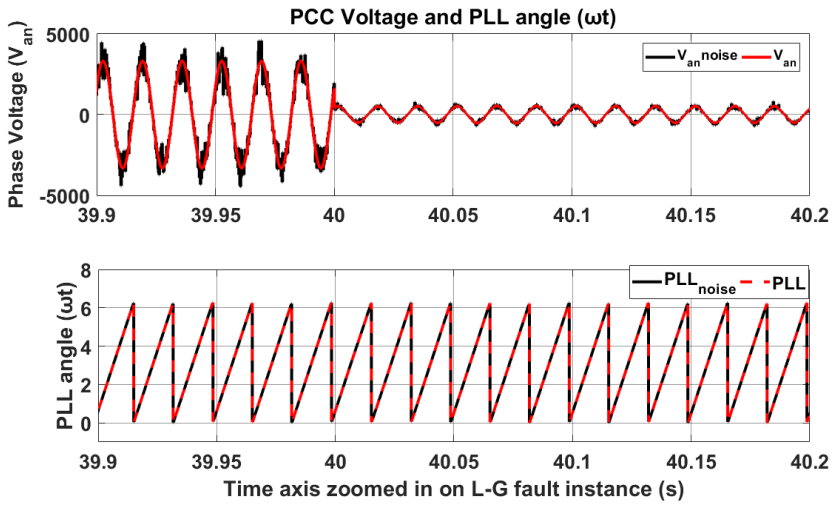

Figure 4.2: Graph demonstrating PLL operation remains unaffected by measurement noise and fault dynamics.

The closed loop inverter state-space along with PLL equations can be shown as follows:

$$\begin{bmatrix} \dot{i}_d \\ \dot{i}_q \\ \dot{\delta}_e \\ \dot{\Delta\omega} \end{bmatrix} = \begin{bmatrix} -\frac{K_p^d}{L_{inv}} - \frac{K_i^d}{sL_{inv}} & \omega & 0 & 0 \\ -\omega & -\frac{K_p^q}{L_{inv}} - \frac{K_i^q}{sL_{inv}} & 0 & 0 \\ 0 & 0 & 0 & 1 \\ 0 & 0 & 0 & 0 \end{bmatrix} \begin{bmatrix} i_d \\ i_q \\ \delta_e \\ \Delta\omega \end{bmatrix} + \begin{bmatrix} \frac{K_p^d}{L_{inv}} + \frac{K_i^d}{sL_{inv}} & 0 & 0 & 0 \\ 0 & \frac{K_p^q}{L_{inv}} + \frac{K_i^q}{sL_{inv}} & 0 & 0 \\ 0 & 0 & 0 & 0 \\ 0 & 0 & 0 & K_p^{PLL}V_q + K_i^{PLL} \end{bmatrix} \begin{bmatrix} I_d^{ref} \\ I_q^{ref} \\ V_d \\ V_q \end{bmatrix} \tag{4.6}$$

$$\begin{bmatrix} P_{ac} \\ Q_{ac} \end{bmatrix} = \begin{bmatrix} V_d & V_q \\ -V_q & V_d \end{bmatrix} \begin{bmatrix} i_d \\ i_q \end{bmatrix} \tag{4.7}$$

Table 4.1: Controller gains after design and tuning

Control Loop	k_p	k_i
HESS Current/Power	1.3	3
Inverter d-axis current/Active Power	0.86	0.6
Inverter q-axis current/Reactive Power	-0.86	-0.6
PV MPPT	-1.5	-7

where K_p^d ,K_i^d and K_p^q, K_p^q are the proportional and integral gains of the closed loop control for P and Q loops respectively which can be found in Table 4.1.

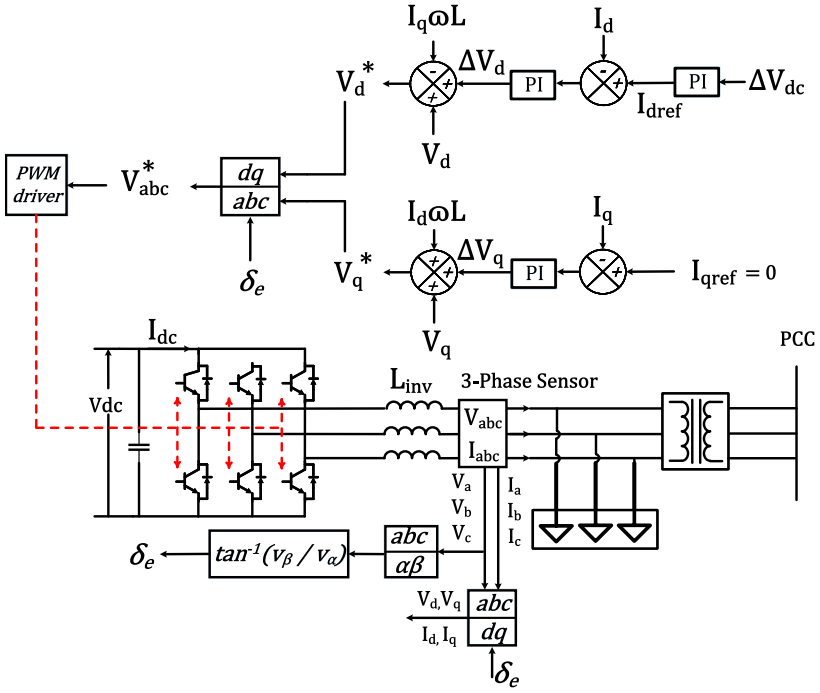

Figure 4.3: Control diagram of 3-phase $d-q$ inverter.

4.4 Proposed Supervisory Controller Design

For a steady-state distribution system, the voltage angle (δ) at DER PCC is constant. When a fault or loading occurs there is a deviation from the steady state PCC angle ($\Delta\delta$) consistent to the change in loads experienced in the distribution system.

The ($\Delta\delta$) can be defined as follows:

$$\Delta\delta = \delta_k - \delta_{k-1} \tag{4.8}$$

where, δ_k is the PCC angle is the steady state angle and δ_{k-1} is the PCC angle during the fault/dynamic condition. The objective of the supervisory level control is to minimize ($\Delta\delta$) by supplying power from DC micro-grid. The proposed approach detects ($\Delta\delta$) and compensates for grid dynamics, thus stabilizing frequency. For deriving the open loop transfer function for DC-DC converters it is assumed that they are lossless. Thus

$$P_{dc} = P_{bat}, V_{dc}I_{dc} = V_{bat}I_{bat}, P_{ac} = P_{dc} \tag{4.9}$$

where P_{dc} is the power output from battery converter at DC bus, P_{bat} is the power input to the converter from the battery source and P_{ac} is the Active Power at the inverter output, V_{dc} is the DC bus Voltage, I_{dc} is the DC bus current, V_{bat} is the input-side converter Voltage and I_{bat} is the input-side converter current. Also, the power transfer through an inductive line, assuming $sin(\Delta\delta) \approx \Delta\delta$ can be written as

$$P_{ac} = \frac{V_1 V_2 \Delta\delta}{X} \tag{4.10}$$

where P_{ac} is the 3-phase AC Active Power, V_1 is the sending end Voltage, V_2 is the receiving end Voltage, $\Delta\delta$ is the Voltage angle difference between V_1 and V_2 and X is the inductive reactance between the sending and receiving end.

The state space representation of the DC-DC boost converter discussed in Section 4.3.1 and (4.9) and (4.10) can be used to derive

$$\frac{\Delta\delta(s)}{Ibat\_ref(s)} = \frac{s\frac{XI_{dc}I_{in}}{C} + \frac{P_{dc}XD'}{L}}{s\frac{V_{dc}V_1V_2}{L} + \frac{V_{dc}V_1V_2}{RLC} + \frac{I_{in}D'V_1V_2}{C^2}} \tag{4.11}$$

where $Ibat\_ref$ is battery current reference from Fig. 4.1.

Equation (4.11) shows that the voltage angle deviations at the inverter PCC can be controlled by supplying or absorbing power from the dispatch-able energy storage devices, battery and ultra-capacitor. Minimizing (4.11) with multiple HESS can be achieved using an optimal controller.

The LQR formulation specific to our control problem is shown below:

$$J = \int_0^\infty (\Delta\delta^T(t) \cdot Q \cdot \Delta\delta(t) + U^T(t) \cdot R \cdot U(t))dt \tag{4.12}$$

where $Q(t) = 20 * C'(t) \cdot C(t)$, $R = 0.1$, J is the linear quadratic function, $\Delta\delta^T(t)$ is the transpose of the dynamically changing state of interest, Q is the static penalty factor associated with the state, $U^T(t)$ is the transpose of the recursively generated optimal control and input to the plant in closed loop, $Q(t)$ and R are the penalty factors for state and input respectively.

To implement a controller based on such dynamic quadratic optimization we need to utilize system state space that captures system parameters dynamically.

4.4.1 Partial derivative based real-time plant approximation using measurement data

Consider that the power grid can be represented as

$$\Delta\delta_{t+1} = \Delta f(\delta_t^*, U_t^*) + \frac{\partial f}{\partial \delta}(\delta_t^*, U_t^*)\Delta\delta_t + \frac{\partial f}{\partial U}(\delta_t^*, U_t^*)\Delta U_t \tag{4.13}$$

where $\Delta\delta_{t+1} = \delta_{t+1} - \delta_{t+1}^*$, $\Delta\delta_t = \delta_t - \delta_t^i$, $\Delta U_t = U_t - U_t^i$ From the above we can write in discrete form

$$\Delta\delta_{k+1} = A_k\Delta\delta_k + B_k\Delta U_k \tag{4.14}$$

where $A_k = \frac{\partial f}{\partial \delta}(\delta_k^i, U_k^i)$ and $B_k = \frac{\partial f}{\partial U}(\delta_k^i, U_k^i)$. Let, $z_k = \Delta x_{k+1}$ and $u_k = \Delta U_t$, then

$$z_{t+1} = A_k z_t + B_k v_t \tag{4.15}$$

Where, z_{t+1} is the state matrix for future time step, A_t is the state transition matrix, B_t is the Output matrix and u_t is the Output of the state space that is being approximated.

To approximate the state (z) we apply linearization for the plant function $f(z, u)$ around the operating point (z_t, u_t). The solution can be found using the Taylor series on $f(z, u)$ [approximated up to first order]. The expansion is given below:

$$\begin{aligned} Z(t+1) = f(Z(t), U(t)) + \\ \frac{\partial f}{\partial Z}(Z(t), U(t))(Z(t) - Z_{t-1}) + \\ \frac{\partial f}{\partial U}(Z(t), U(t))(U(t) - U_{t-1}) \end{aligned} \tag{4.16}$$

Where, Z_{t-1} is the state and U_{t-1} is the Input from the past time step, respectively. Arranging equation (4.16) in the standard state space format we get,

$$\begin{aligned} \begin{bmatrix} Z(t+1) \\ 1 \end{bmatrix} = \begin{bmatrix} \frac{\delta f}{\delta Z}(Z(t), U(t)) & f(Z(t), U(t)) \\ 0 & 1 \end{bmatrix} \\ \begin{bmatrix} \Delta Z(t) \\ 1 \end{bmatrix} + \begin{bmatrix} \frac{\delta f}{\delta U}(Z(t), U(t)) \\ 1 \end{bmatrix} \begin{bmatrix} \Delta U(t) \end{bmatrix} \end{aligned} \tag{4.17}$$

Equations (4.13)-(4.17) are for general form of the state space. For the system

specific to Fig. 4.1 we have the following:

$$\Delta\delta = f(I_{dc}, I_{in}, V_{dc}, V_1, V_2, I_{bat\_ref}) \cdot I_{bat\_ref} \tag{4.18}$$

Where, Z is now a matrix comprising of previously defined states I_{dc}, I_{in}, V_{dc}, V_1 and V_2 and U is the input to the system, I_{bat_ref}.

Thus, the Taylor series approximation for each element of the state matrix (Z) can be given by the following equations:

$$\begin{aligned} I_{dc}(t+1) = f(Z(t), U(t)) + \\ \frac{\delta f}{\delta I_{dc}}(Z(t), U(t))(I_{dc}(t) - I_{dct-1}) + \\ \frac{\delta f}{\delta U}(Z(t), U(t))(U(t) - U_{t-1}) \end{aligned} \tag{4.19}$$

$$\begin{aligned} I_{in}(t+1) = f(Z(t), U(t)) + \\ \frac{\delta f}{\delta I_{in}}(Z(t), U(t))(I_{in}(t) - I_{int-1}) + \\ \frac{\delta f}{\delta U}(Z(t), U(t))(U(t) - U_{t-1}) \end{aligned} \tag{4.20}$$

$$\begin{aligned} V_{dc}(t+1) = f(Z(t), U(t)) + \\ \frac{\delta f}{\delta V_{dc}}(Z(t), U(t))(V_{dc}(t) - V_{dct-1}) + \\ \frac{\delta f}{\delta U}(Z(t), U(t))(U(t) - U_{t-1}) \end{aligned} \tag{4.21}$$

$$V_1(t+1) = f(Z(t),U(t))+ \frac{\delta f}{\delta V_1}(Z(t),U(t))(V_1(t)-V_{1t-1})+ \frac{\delta f}{\delta U}(Z(t),U(t))(U(t)-U_{t-1}) \quad (4.22)$$

$$V_2(t+1) = f(Z(t),U(t))+ \frac{\delta f}{\delta V_2}(Z(t),U(t))(V_2(t)-V_{2t-1})+ \frac{\delta f}{\delta U}(Z(t),U(t))(U(t)-U_{t-1}) \quad (4.23)$$

The above set of equations can be aggregated into the state space representation as:

$$\begin{bmatrix} cI_{dc}(t+1) \\ I_{in}(t+1) \\ V_{dc}(t+1) \\ V_1(t+1) \\ V_2(t+1) \\ 1 \end{bmatrix} = \begin{bmatrix} O_{11} & 0 & 0 & 0 & 0 & O_{15} \\ 0 & O_{22} & 0 & 0 & 0 & O_{25} \\ 1 & 0 & O_{33} & 0 & 0 & O_{35} \\ 0 & 0 & 0 & O_{44} & 0 & O_{45} \\ 0 & 0 & 0 & 0 & O_{55} & O_{55} \\ 0 & 0 & 0 & 0 & 0 & 1 \end{bmatrix} \begin{bmatrix} \Delta I_{dc}(t) \\ \Delta I_{in}(t) \\ \Delta V_{dc}(t) \\ \Delta V_1(t) \\ \Delta V_2(t) \\ 1 \end{bmatrix} + \begin{bmatrix} \frac{\delta f}{\delta U}(Z(t),U(t)) \\ \frac{\delta f}{\delta U}(Z(t),U(t)) \\ \frac{\delta f}{\delta U}(Z(t),U(t)) \\ \frac{\delta f}{\delta U}(Z(t),U(t)) \\ \frac{\delta f}{\delta U}(Z(t),U(t)) \\ 1 \end{bmatrix} \begin{bmatrix} \Delta U(t) \end{bmatrix} \quad (4.24)$$

$$\begin{bmatrix} \Delta\delta(t+1) \end{bmatrix} = \begin{bmatrix} 0 & 0 & 0 & 0 & 0 & 0 \\ 0 & \frac{V_{in}X}{V_1V_2} & 0 & 0 & 0 & 0 \\ 0 & 0 & 0 & 0 & 0 & 0 \\ 0 & 0 & 0 & 0 & 0 & 0 \\ 0 & 0 & 0 & 0 & 0 & 0 \\ 0 & 0 & 0 & 0 & 0 & 0 \end{bmatrix} \begin{bmatrix} \Delta I_{dc}(t) \\ \Delta I_{in}(t) \\ \Delta V_{dc}(t) \\ \Delta V_1(t) \\ \Delta V_2(t) \\ 1 \end{bmatrix} \quad (4.25)$$

Where, $\frac{\delta f}{\delta I_{dc}}(Z(t),U(t))$ is O_{11}, $\frac{\delta f}{\delta I_{in}}(Z(t),U(t))$ is O_{22}, $\frac{\delta f}{\delta V_{dc}}(Z(t),U(t))$ is O_{33},

$\frac{\delta f}{\delta V_1}(Z(t), U(t))$ is O_{44}, $\frac{\delta f}{\delta V_2}(Z(t), U(t))$ is O_{55},

$f(Z(t), U(t))$ is O_{15}, O_{25}, O_{35}, O_{45}, O_{55}, $\Delta I_{dc}(t)$ is $I_{dc}(t) - I_{dc}(t-1)$,

$\Delta U(t)$ is $U(t) - U(t-1)$ and so on.

All the elements from the approximated state-space shown above can be measured online from the model. The function $f(z_t, u_t)$ is simply the ratio of the plant output measurement, $\Delta\delta_t$, and plant input measurement, $Ibat\_ref$. Partial derivatives can be approximated as finding the rate of change of the plant function $f(z_t, u_t)$ with respect to the rate of change of the state of interest.

The process of approximating the state space using partial derivatives of the various measurement data can be summarized by the algorithm 5:

Algorithm 5 Measurement data based state space approximation

Step: 1 Collect measurement data of all the elements of the input and output vector for identification.plant model from Fig. (4.1) for the current and previous time step

Step: 2 Calculate the partial derivative of the plant model with respect to the states of interest to populate the state transition matrix (A_{ss}) from equation (4.24)

Step: 3 Calculate the partial derivative of the plant model with respect to the input to populate the output matrix (B_{ss}) from equation (4.25)

Step: 4 Similarly calculate C_{ss} matrix using measurement data from the online model

This method provides the user with an online approximation of the dynamically changing state space using the available measurement data. A_{ss}, B_{ss} and C_{ss} matrices ($D_{ss} = 0$) obtained as a result of this method can be further utilized to calculate the optimal gain.

To obtain the dynamic state vector, X(k), we use Kalman estimation online. Algorithm 9 details the step-wise process of estimating the state of interest ($\Delta\delta$) from the dynamic state space. The state estimate from Algorithm 9 is used to calculate the optimal control output. The controller gain (K_{LQR}) for every sample is calculated

using a 2-step process given in Algorithm 10, which gives the optimal control output, $Ibat\_ref$.

Algorithm 6 Kalman State Estimation

Step: 1 Initialize Matrices $\hat{X_{ke}}$, P_{ke}, Q_{ke}, K_{ke}, R_{ke}, Res

Step: 2 Collect ($Ibat\_ref$) and ($\Delta\delta$) samples and arrange in Matrices U and y respectively, include the RLS identified state space matrices A_{ss}, B_{ss}, C_{ss}

Step: 3 Calculate the initial estimate of states $\hat{X_{ke}}$

$$\hat{X_{ke}}(k) = A_{ss}(k) \cdot \hat{X_{ke}}(k-1) + B_{ss}(k) \cdot U(k)$$

Step: 4 Calculate the Error Co-variance Estimate

$$P_{ke}(k) = A_{ss}(k) \cdot P_{ke}(k-1) \cdot A_{ss}^{T}(k) + Q_{ke}$$

Step: 5 Calculate the Kalman Gain :

$$K_{ke}(k) = \frac{P_{ke}(k) \cdot C_{ss}^{T}(k)}{C_{ss}(k) \cdot P_{ke}(k) \cdot C_{ss}^{T}(k) + R_{ke}}$$

Step: 6 Calculate the measurement residue

$$Res(k) = y(k) - C_{ss}(k) * \hat{X_{ke}}(k)$$

Step: 7 Update the Error Co-variance Estimate

$$P_{ke}(k) = [I - K_{ke}(k) \cdot C_{ss}(k)] \cdot P_{ke}(k)$$

Step: 8 Update the State Co-variance Estimate

$$\hat{X_{ke}}(k) = \hat{X_{ke}}(k) + K_{ke}(k) \cdot Res(k)$$

The optimal HESS inner loop reference, $Ibat\_ref(k)$, is ensures that ($\Delta\delta$) is minimized. The optimal set-point drives the closed-loop form, shown in (4.5), of the battery converter in duty cycle control mode.

The summary of the multi-level control structure is given by loop gain as shown in (4.26).

Algorithm 7 Linear Quadratic Regulator Control

Step: 1 Extract RLS identified state space matrices A_{ss}, B_{ss}, C_{ss} and Kalman Estimate $\hat{X_{ke}}$

Step: 2 Set $Q_{lqr}(k) = 20 \cdot C_{ss}^T \, C_{ss}$, $R_{lqr} = 0.1$ and initialize Algebraic Riccati Solution $P_{lqr}(k-1)$ and the time period of the LQR call function in simulation, T_c

Step: 3 Solve for Algebraic Riccati Equation

$$\begin{aligned} P_{lqr}(k) = [P_{lqr}(k-1) \cdot A_{ss}(k) + A_{ss}^T(k) \cdot P_{lqr}(k-1) \\ - P_{lqr}(k-1) \cdot B_{ss}(k) \cdot R_{lqr}^{-1}(k) \cdot B_{ss}^T(k) \\ \cdot P_{lqr}(k-1) + Q_{lqr}(k)] \cdot T_c + P_{lqr}(k-1) \end{aligned}$$

Step: 4 Find LQR gain K_{lqr} for k^{th} time

$$K_{lqr}(k) = R_{lqr}^{-1} \cdot B_{ss}^T(k) \cdot P_{lqr}(k)$$

Step: 5 The optimal control output $Ibat\_ref$ is given by:

$$Ibat\_ref(k) = -K_{lqr}(k) \cdot \hat{X_{ke}}(k)$$

$$G(s) = \frac{\Delta\delta(s)}{Ibat(s)} \cdot \frac{Ibat(s)}{d(s)} \cdot \frac{d(s)}{V_{dc}(s)} \cdot \frac{V_{dc}(s)}{i_d(s)} \cdot \frac{i_d(s)}{\Delta V_d(s)} \tag{4.26}$$

where $\frac{V_{dc}(s)}{i_d(s)} \cdot \frac{i_d(s)}{\Delta V_d(s)}$ represents the inverter d-q control (primary level), $\frac{Ibat(s)}{d(s)}$ is the battery current control applied on the DC micro-grid, $\frac{d(s)}{V_{dc}(s)}$ represents the effect of input side current control on DC bus voltage and $\frac{\Delta\delta(s)}{Ibat(s)}$ describes the gain produced by the LQR minimization based proposed supervisory control loop.

4.5 Validity and scalability study on Modified IEEE 123 bus system

To test the proposed architecture for validity and modularity, case studies are performed on the modified 123 bus distribution system [75] shown in Fig. 4.4. This test system is a medium-sized power grid network with multiple load regulators and shunt capacitors. Unbalanced loading and alternate power-flow paths are also some of their characteristics. The test system is modified by adding a synchronous generator

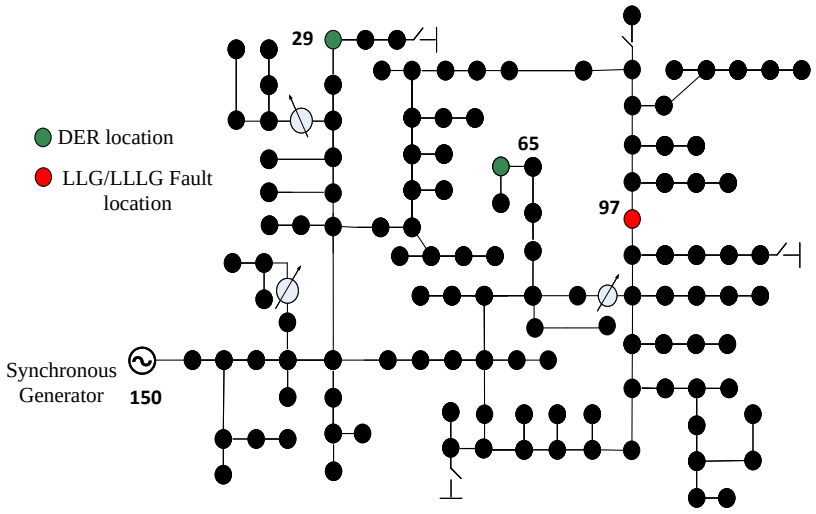

Figure 4.4: Micro-grid integration study for a 123 bus feeder.

on bus 149 such that it can act autonomously to regulate the grid dynamics that can be initiated by the user. This will serve as a base case for the analysis and validation of the proposed architecture. Two cases of grid dynamics are studied, namely, Line-Line-to-Ground fault (LLG) (Case I) and Line-Line-Line-to-Ground fault (LLLG) (Case II) to understand the response of the proposed architecture. The study is performed by observing the effect of grid dynamics at the PCC bus of 2 identical micro-grids consisting of DER and controller shown in Fig. 4.1. Fig. 4.4 micro-grids are connected on buses 29 and 65. This study is aimed at analyzing the impact of grid dynamics on PCC angle deviations ($\Delta\delta$) for each micro-grid. For Case I, a Line-to-Ground Fault (LG) is simulated for 0.18 seconds on bus 97 between phase A and ground with fault and ground resistance both being 1 Ω. Case II is the study of the effect of a LLLG fault applied at bus 97 with the micro-grid locations similar to Case I. Please note that for both cases the pre-fault and post-fault conditions are the same.

4.5.1 Frequency response for LLG fault (Case I)

Fig. 4.5 presents frequency, micro-grid angles, and PU power-sharing from each micro-grid in response to the LLG fault on the modified 123 bus system. The fault

Table 4.2: Results on Modified 123 bus system

	Parameter	MBS	MBS + FD	Imp Vs MBS	MBS + LQR	Imp Vs MBS
Case I	FN (Hz) ST (s)	59.52 112	59.53 104	2.08% 8	59.55 55.17	6.25% 56.83
Case II	FN (Hz) ST (s)	59.32 119.5	59.36 114	5.85% 5.5	59.38 70.86	8.79% 48.64

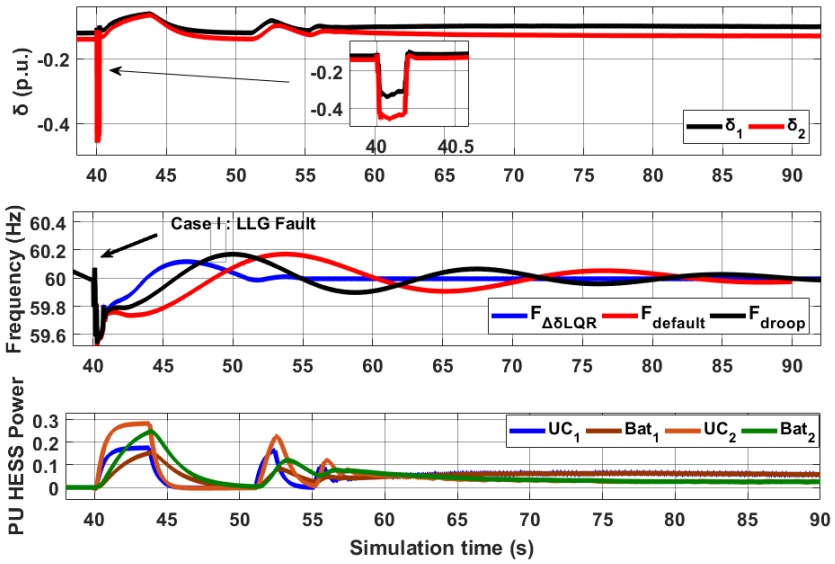

Figure 4.5: Case I : Frequency regulation [default system Vs $\Delta\delta$ minimization using LQR Vs Frequency-droop].

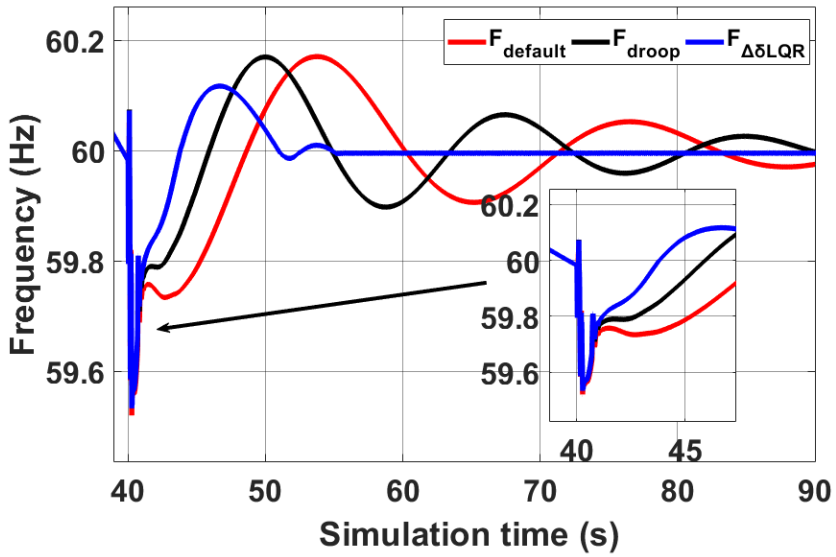

Figure 4.6: Case I : Frequency regulation graph

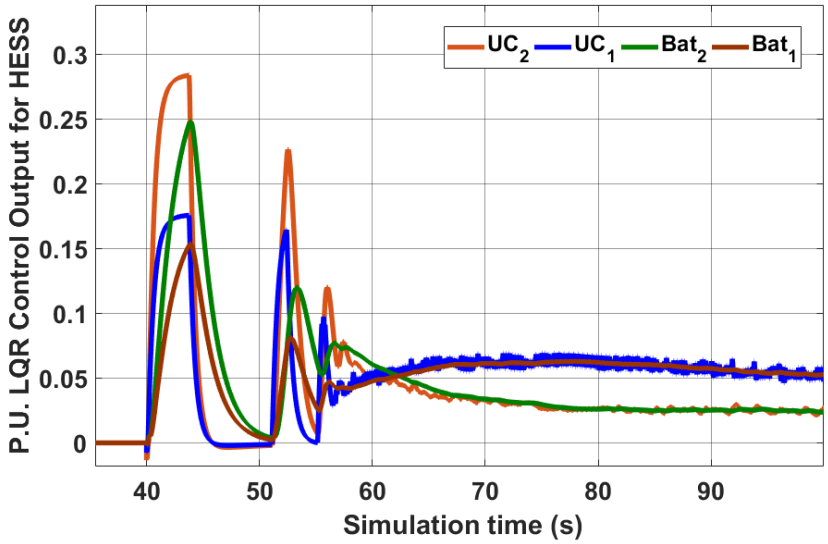

Figure 4.7: Case I : LQR Control Output for HESS

event is initiated at 40 seconds and removed after 0.18 seconds in simulation). The frequency drops to 59.52 Hz with the default 123 bus response. For the frequency-droop approach, the frequency nadir improves to 59.53 Hz. The proposed architecture slightly improves the inertial response with nadir reaching 59.55 Hz for the LLG fault case. The default 123 bus system with synchronous generator settles in 112 seconds, whereas that for LQR and frequency-droop approach is 55.17 seconds and 104 seconds respectively. Unlike the frequency nadir study, the settling time for the system is significantly improved due to the application of the proposed approach. Fig. 4.6 showcases the primary and secondary response of the system for the various approaches mentioned above. Fig. 4.7 discusses the power-sharing by the dispatchable hybrid energy storage system within the micro-grids located at bus 29 (Bat_1, UC_1) and bus 65 (Bat_2, UC_2). The figure shows that sources closest to the fault location (Bat_2, UC_2) contribute more power compared those (Bat_1, UC_1) located. This is because the PCC angle deviations to fault are more pronounced at bus 65 than bus 29 due to its proximity. For Case I, the proposed LQR approach improves the settling time of the system significantly as compared to the frequency-droop approach. But as seen from Fig. 4.5 subplot 1, the angle deviation due to LLG fault persists only

for a few seconds, and the system is quickly brought back to nominal conditions post fault. Thus, the proposed approach does not contribute significantly to improvement in frequency nadir. However, the proposed approach shares power amongst DERs based on their proximity to the fault location.

4.5.2 Frequency response to LLLG Fault (Case II)

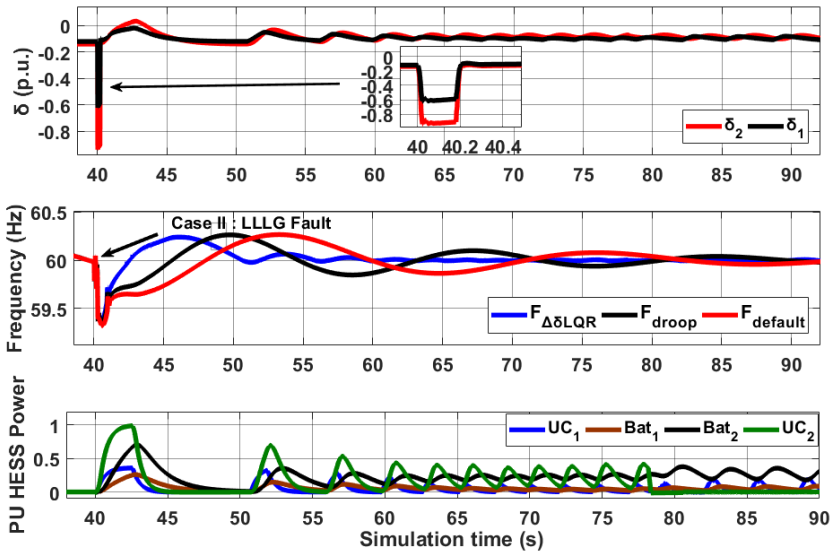

Figure 4.8: Case II : Frequency regulation [default system Vs $\Delta\delta$ minimization using LQR Vs Frequency-droop].

The effect of the LLLG fault on the modified 123 bus system is severe in terms of frequency nadir and its effect on PCC angles. The frequency nadir drops to 59.32 Hz for the default modified 123 bus distribution system. As shown in Fig. 4.8, the LQR approach displays a better performance compared to frequency-droop control with an improvement of 0.02 Hz. For the secondary response characteristics, the proposed LQR minimization performs the best, settling at 70.86 seconds. The frequency-droop response is 44 seconds slower as shown in Fig. 4.9. The default frequency regulation by the virtual of the synchronous generator alone is the slowest to normalize in 119.5 seconds. Micro-grid 2 connected at bus 65 is closer to the fault location (bus 97) than micro-grid 1 and thus, the optimal control routine observes a larger effect on $(\Delta\delta_2)$ than $(\Delta\delta_1)$. Consequently, the optimal control set-points for DER at bus 65

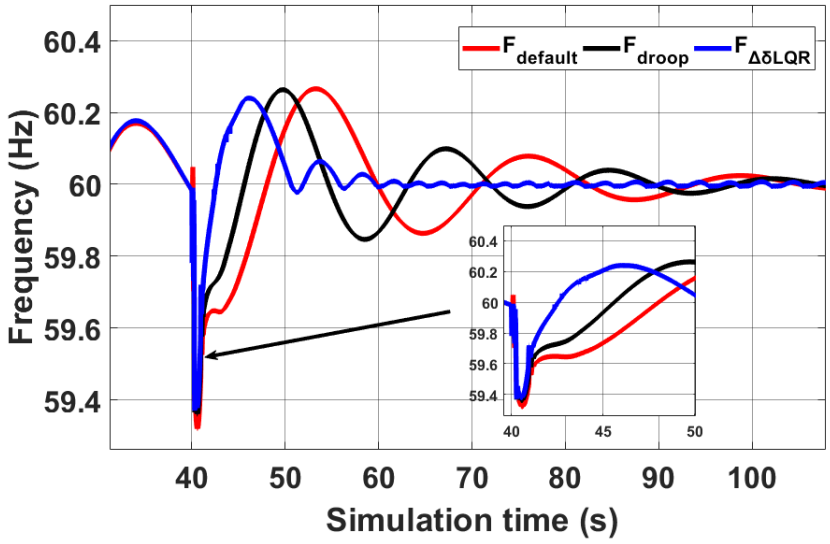

Figure 4.9: Case II : Frequency regulation graph

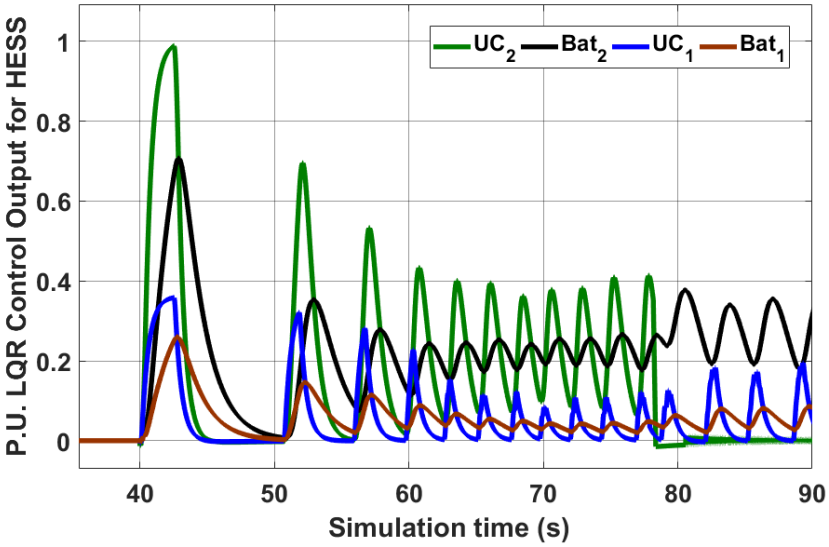

Figure 4.10: Case II : LQR Control Output for HESS

are higher than that at bus 29.

Table 4.2 summarizes the result for Case I and Case II on the modified 123 bus system for various control approaches. The following abbreviations are used : FN is Frequency Nadir, ST is Settling Time, FD is Frequency-Droop approach, MBS is Modified Bus System, Imp Vs MBS is Improvement Versus Modified Bus System. The proposed architecture performs well for the secondary response with faster settling times. However, as observed from the frequency graphs (Fig. 4.6 and Fig. 4.9), there is not much improvement in the inertial response in the case of the proposed architecture when compared to the default distribution system response and the frequency-droop approach.

4.6 Summary of Proposed Inverter Angle Minimization Based Optimal Control Approach

This chapter proposes a novel design approach for frequency regulation by managing multiple HESS. it also quantifies a comparison base between the proposed architecture and the frequency-droop approach for the inertial and secondary response for an IEEE medium-size distribution system. In the proposed architecture, the power-sharing is performed by individual micro-grids depending on their location and proximity to the fault. As the intensity of fault was increased from LLG to LLLG fault, the power distribution amongst the micro-grids was also observed to increase. This increase was proportional to the angle deviations experienced by individual micro-grid PCCs. The settling time for the secondary frequency response improves significantly when compared with the conventional frequency-droop approach. However, due to the nature of the fault studied and its removal after 0.18 seconds, the proposed architecture, like the conventional frequency-droop approach, does not improve frequency nadir that much. Some of the advantages of the proposed control architecture are that it provides a better secondary response for frequency regulation for bolted faults. The proposed DER control topology operates for improved frequency response without the

need for frequency-droop information of the system. The architecture is favorable for DERs connected in DC link topology as it works autonomously by measuring locally detected dynamics at PCC. Thus, the approach aims at mitigating the local effects of grid dynamics and operates independently from other micro-grids in the network.

CHAPTER 5: CONTROL OUTPUT UNCERTAINTY BASED OPTIMAL ROBUST CONTROLLER DESIGN FOR MULTI-MICRO-GRIDS

In the previous chapter, we discussed an optimal control approach based on grid angle minimization quality function. The penalty factors for achieving the minimum of the quality function Q and R were static values generated based on settling time and steady-state error on PCC frequency which is a function of the state space output $\Delta\delta$. Also, battery and ultra-capacitor storage systems received the same set-points from the LQR routine. That approach was based on the sizing of each component of HESS which is sub-optimal.

5.1 Introduction

Linear Quadratic Regulator (Optimal Control) theory is utilized in a wide range of operations depending on system and control requirements. For example, a comprehensive method for computing a Linear Quadratic controller with Optimal Reference Tracking (LQR-ORT) for a three-phase inverter is presented in [93], whereas a linear matrix inequality quadratic regulator (LMI-LQR) approach is proposed in [94]. In [95], a bumpless-compensator is proposed which reduces the error between the outputs of two controllers during the off-grid-on-grid transition by optimally reducing an error measure based on LQR theory. Authors of [96] have implemented a data-driven solution to the discrete-time infinite-horizon linear quadratic regulator (LQR) on an uninterruptible power supply plant. State-space-based design of the control system for a boost converter can be enhanced with a linear quadratic regulator (LQR) optimization, that can configure the converter loss equation as cost function [97]. H_∞ control is another popular LQR approach. The disadvantages of H_∞ techniques in-

clude the level of mathematical understanding needed to apply them successfully and the need for a reasonably good model of the system. Ref. [98] proposes a coordinated control scheme on a coal-fired power unit model using the linear-quadratic regulator (LQR). The method is used to ensure control performance based on reasonable scheduling of distributed equipment; the LQR is applied to limit the control actions to meet the actuator saturation constraints. The optimal state feedback gain of a virtual synchronous converter is determined to adaptively adjust the emulated inertia and damping constants for renewable resources [99]. Earlier we have proposed integrated control architecture and the [100–102]

Authors of [103] have discussed a full-state observer-based linear-quadratic regulator (LQR) for damping of subsynchronous interaction (SSI) in doubly-fed induction generator (DFIG)-based wind farms. LQRs have also been applied to grid-connected inverters. An example can be seen in [94], where a linear matrix inequality-linear quadratic regulator (LMI-LQR) approach is proposed for polytopic uncertainties in the LCL filter parameters of a grid-connected inverter. Another example of LQR is seen in [79] which presents a multi-functional single-stage residential photovoltaic power supply based on a linear quadratic regulator (LQR). The system makes use of a single-phase power converter connected to the grid through an LCL filter. On similar lines, active power and voltage management of power distribution systems are based on an optimal control architecture for single-phase inverters in [104]. Article [105] discusses a method of designing Wide Area Control based on a discrete Linear Quadratic Regulator (LQR) and Kalman filtering based state-estimation that can be applied for real-time damping of inter-area oscillations of wind integrated power grid. In other applications, authors of [80] discuss the design of the LQR controller for intelligent control of a quadrotor helicopter where they have emphasized the linearized state modeling of the system. High level consensus schemes for management of heterogeneous multi-agent robotic systems (MAS) are proposed using LQR

in [81], [82], [83], [84] and [85].

An optimal robust controller is proposed in this chapter that provides setpoints for each device of HESS based on their sensitivity to the minimization function. The minimization of angular deviation ($\Delta\delta$) at the micro-grid Point of Common Coupling (PCC) during grid dynamics results in improved frequency regulation. This approach can work independent of frequency-droop information [72]. The proposed optimal Control limits the penalty factor R based on the uncertainty of control output. Due to heavy reliance on guesswork to determine conventional LQR penalty factors, the control output may not result in an optimal one. This approach recursively provides an update on the control output penalty factor R such that the uncertainty on control output U is minimized. The final solution of optimal Control is still aimed at minimizing $\Delta\delta$, which is the output state, but the dynamically updated penalty factor ensures that sub-optimal set points due to uncertain outputs are avoided.

5.2 Research Contributions

This chapter proposes an improved algorithm for LQR based minimization. Key highlights of the algorithm are:

- This algorithm initializes the control penalty factor (R) gains based on assumed maximum control uncertainty that the regulator might have due to the use of inappropriate penalty factor gains.
- The algorithm recursively updates the ARE solution (P) and state penalty (Q) for each iteration, thus leading to a faster response from the system.
- optimal Control updates the control penalty factors (R) for individual energy storage devices based on the effect they create in frequency in grid support mode.
- Due to ramp-rate-based control update, battery, and ultra-capacitor set-points

can be optimized automatically depending on their respective power and energy densities.

5.3 Design and Control of Proposed DC Micro-grid

The proposed DC Micro-grid architecture is detailed in Fig. 5.1. It consists of a 2 MW PV farm and a Hybrid Energy Storage System (HESS) comprising of 1.2 MWh battery and 800 kW Ultra-capacitor banks. The PV Distributed Energy Resource (DER) is connected in a DC-link topology with HESS. Each storage device of HESS is controlled by their bi-directional DC-DC converters. DC-link is rated at 1200 V and is regulated by the active power control loop of the 3-phase $d-q$ inverter. Inverter $d-q$ control and HESS primary control is summarized in Fig. 5.1.

5.3.1 Design and Control of PV farm

A PV farm is a current source and to maximize its output we use Maximum Power Point (MPP) as a reference. To achieve this we need to drive the PV plant at the Voltage (V_{MPP}) corresponding MPP. A $DC-DC$ converter comprises two filter elements and hence is defined as a second-order system. The equations based on the volt$-$second and capacitor$-$charge balance for the converter the state space representation can be derived as

$$\begin{bmatrix} \dot{\bar{i}} \\ \dot{\overline{V}} \end{bmatrix} = \begin{bmatrix} 0 & \frac{-D'}{L} \\ \frac{D'}{C} & \frac{-1}{RC} \end{bmatrix} \begin{bmatrix} \bar{i} \\ \overline{V} \end{bmatrix} + \begin{bmatrix} \frac{1}{L} & 0 & \frac{V}{L} \\ 0 & \frac{-1}{C} & \frac{i}{C} \end{bmatrix} \begin{bmatrix} \overline{V_{pv}} \\ \overline{i_o} \\ \overline{D_{mpp}} \end{bmatrix} \tag{5.1}$$

$$\begin{bmatrix} V \\ i \end{bmatrix} = \begin{bmatrix} 0 & 1 \\ 1 & 0 \end{bmatrix} \begin{bmatrix} \bar{i} \\ \overline{V} \end{bmatrix} \tag{5.2}$$

where $\overline{V_{pv}}$ is the input side Voltage, $\overline{i_o}$ is the output side current and $\overline{D_{mpp}}$ is the duty cycle input to the converter for boost operation, $\bar{i}$, $\overline{V_g}$ and $\overline{V}$ are inductor current, input voltage and output voltage respectively, and the states of the converter. L,

C and D' are the inductor, capacitor and the duty cycle for buck operation of the converter.

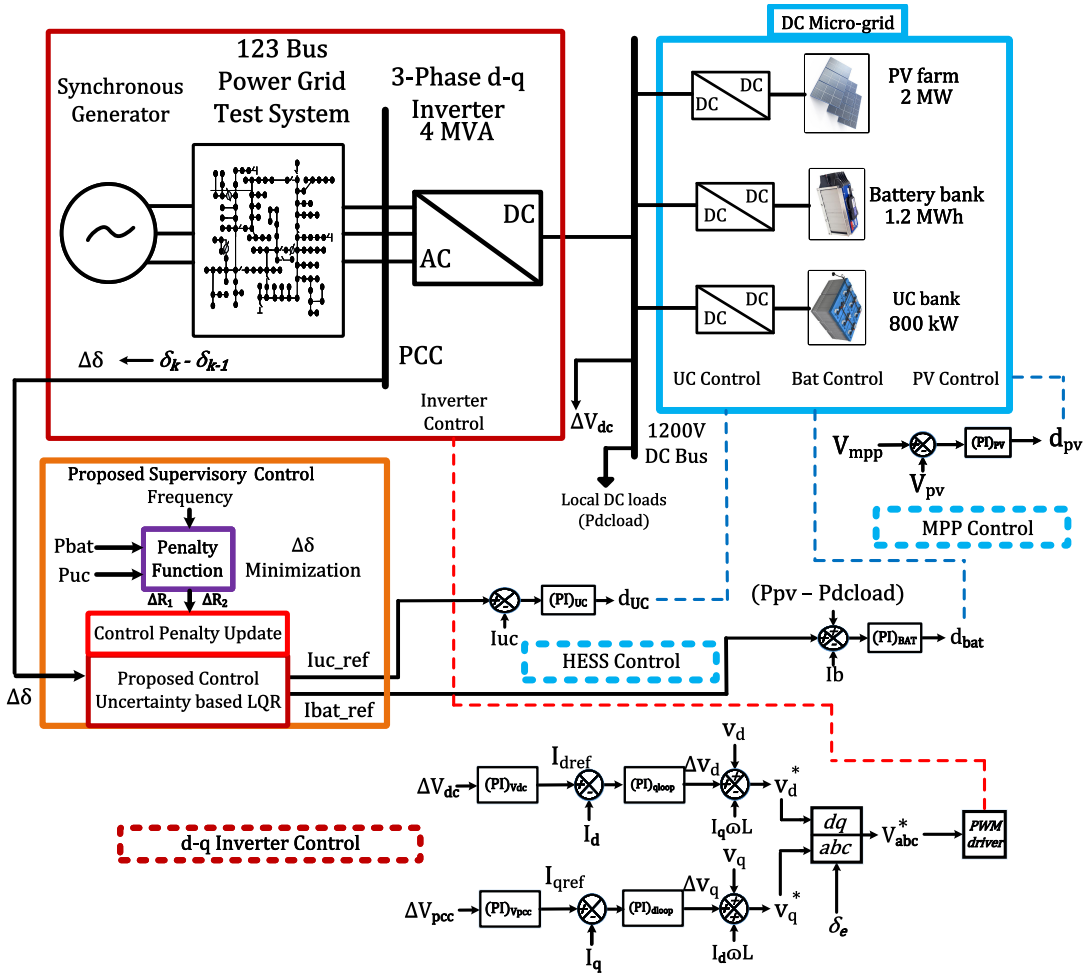

Figure 5.1: Proposed DC micro-grid and Control Architecture.

The PV farm is designed for 2 MW power and employs a look-up table-based MPPT control. The look-up table is used to find the PV farm output voltage corresponding to the maximum power point at the given irradiance. This voltage is used as a reference for a PI controller which generates a duty pulse required to maintain the PV farm voltage at the Maximum Power Point. The control-to-Input voltage transfer function for the DC-DC boost converter can be derived as

$$\frac{\overline{V_{pv}}(s)}{\overline{D_{mpp}}(s)} = \frac{(1-D_{mpp})^2 V_o - (1-D_{mpp}) L I_l s}{(LC)s^2 + (\frac{L}{R_l})s + (1-D_{mpp})^2} \tag{5.3}$$

where $\overline{V_{pv}}$ is the small-signal Input voltage, $\overline{D_{mpp}}$ is the small-signal duty cycle, L,C are the DC-DC converter design elements and R_l is the load resistance. The control architecture for the PV farm is shown in Fig. 5.1. The DC bus is regulated by an inverter. To smooth PV intermittence a battery inner loop control, shown in Fig. 5.1, is designed to absorb all PV farm output power by a negative gain to the per-unit equivalent of PV farm output current on the base of battery capacity and setting that as an added reference value for the battery inner loop control. Additionally, since the battery size is smaller than PV capacity, we assume that the local DC load (shown in Fig. 5.1.) equivalent to the difference between the battery bank and PV size is constantly fed by PV farm. This way the battery control smooth PV dynamics. The result validating successful mitigation of PV dynamics is shown below in Fig. 5.2.

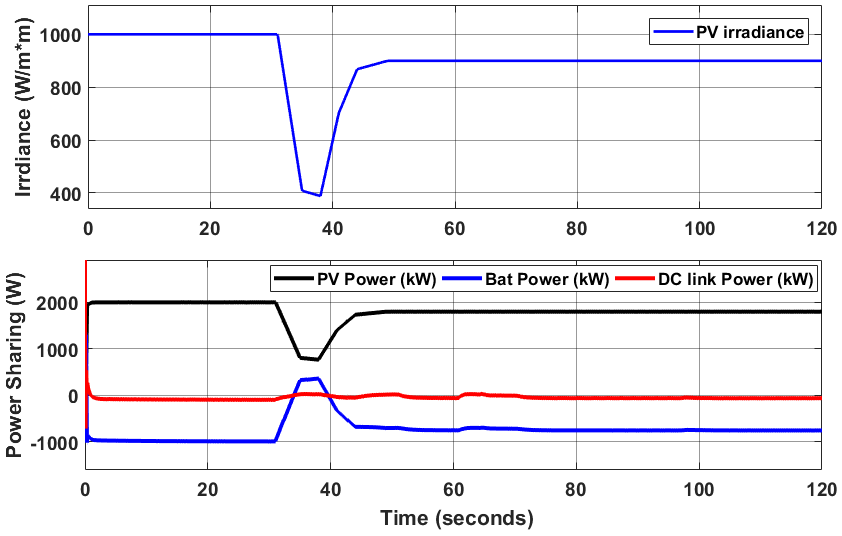

Figure 5.2: Power sharing between PVDER and BESS for smoothing.

5.3.2 Design and Control of Inverter

Fig. 5.3 shows the $d-q$ control implemented on the 3-phase GCI that interfaces DER to the distribution system. All the DC power produced at the DC-link is relayed to the distribution system through the active power loop. Whereas, the reactive power loop is assigned to regulate the PCC AC voltage at 1 p.u. for the proposed approach. The Phase-Locked-Loop (PLL) logic applied to execute the control in the $d-q$ domain

uses the PCC angle information (δ_e). The voltage balance for an L-type inverter can be written in the $d-q$ framework as

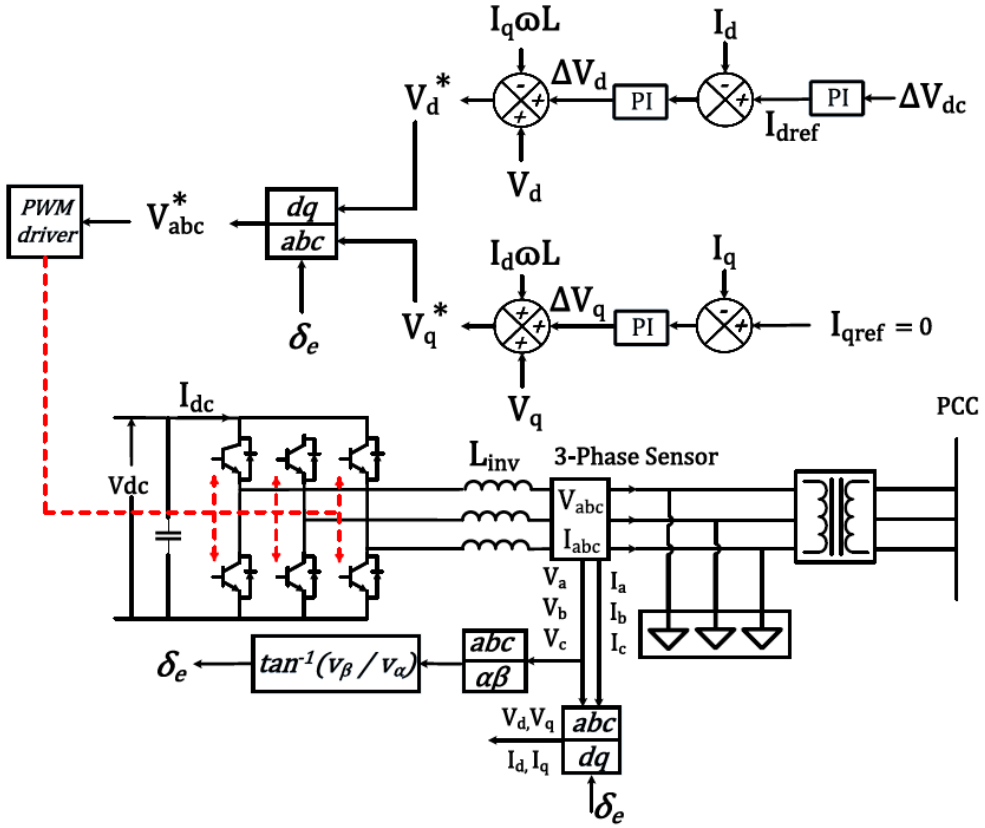

Figure 5.3: d-q architecture of 3-phase inverter.

$$\begin{bmatrix} \dot{i_d} \\ \dot{i_q} \end{bmatrix} = \begin{bmatrix} 0 & \omega \\ \omega & 0 \end{bmatrix} \begin{bmatrix} i_d \\ i_q \end{bmatrix} + \begin{bmatrix} \frac{1}{L_{inv}} & 0 \\ 0 & \frac{1}{L_{inv}} \end{bmatrix} \begin{bmatrix} (v_{dl} - v_d) \\ (v_{ql} - v_q) \end{bmatrix} \tag{5.4}$$

$$\begin{bmatrix} P_{ac} \\ Q_{ac} \end{bmatrix} = \begin{bmatrix} v_d & v_q \\ -v_q & v_d \end{bmatrix} \begin{bmatrix} i_d \\ i_q \end{bmatrix} \tag{5.5}$$

Active power control of 3-phase inverter can be exercised by utilizing the following Laplace domain equation:

$$\frac{\overline{i_d}(s)}{\overline{\Delta v_d}(s)} = \frac{s}{L_{inv} v_d} \left(\frac{v_d + v_q}{s^2 - \omega^2} \right) \tag{5.6}$$

where Δv_d is $v_{dl} - v_d$, s is the Laplace operator.

Reactive power control of 3-phase inverter can be exercised by utilizing the following Laplace domain equation:

$$\frac{Q_{ac}}{\overline{\Delta v_q}(s)} = \frac{sV_d + \omega Vq}{L_{inv}} \left(\frac{1}{s^2 - \omega^2} \right) \tag{5.7}$$

The reactive power through a power line can be represented as:

$$Q_{ac} = \frac{V_{pcc} V_{grid}}{X_l} \left(cos\delta_g - \frac{V_{pcc}}{V_{grid}} \right) \tag{5.8}$$

where V_{pcc} is the PCC voltage, V_{grid} is the grid voltage, X_l is the inductive reactance between PCC and the grid and δ_g is the voltage angle between the PCC and grid. Combining equations (5.7) and (5.8) we get:

$$\frac{V_{pcc}}{\overline{\Delta v_q}(s)} = \left(\frac{X_l}{V_{grid} cos\delta_g - V_{pcc}} \right) \frac{sV_d + \omega Vq}{L_{inv}} \left(\frac{1}{s^2 - \omega^2} \right) \tag{5.9}$$

The above equation governs the regulation of PCC voltage by supplying reactive power, Q_{ac}, using the inverter interface.

5.4 The Proposed Control Architecture

The general form of state space representation can be written as

$$\dot{X} = AX + BU + g + w_k \tag{5.10}$$

$$Y = CX + DU \tag{5.11}$$

where X is a state vector, A is the state transition matrix, B is the input matrix, C is the output matrix, g is the linear component of the plant model that represents affinity in the system, w_k is a discrete noise component. Y is the output vector, U is the control (or input) vector, the feedforward matrix D. g and w_k represent the

components that make the system affine and stochastic, respectively.

The quadratic quality function for affine system remains unchanged. We incorporate the linear component of the system into the state transition matrix as shown below:

$$\underbrace{\begin{bmatrix}\hat{\dot{X}}\\ 1\end{bmatrix}}_{X'_{k+1}} = \underbrace{\begin{bmatrix}A & g\\ 0 & 1\end{bmatrix}}_{A'_k}\underbrace{\begin{bmatrix}\hat{X}\\ 1\end{bmatrix}}_{X'_k} + \underbrace{\begin{bmatrix}B\\ 0\end{bmatrix}}_{B_k}\underbrace{\begin{bmatrix}U\end{bmatrix}}_{U_k} + w_k \tag{5.12}$$

$$\begin{bmatrix}Y\\ 1\end{bmatrix} = \begin{bmatrix}C & 0\\ 0 & 1\end{bmatrix}\begin{bmatrix}\hat{X}\\ 1\end{bmatrix} + \begin{bmatrix}D\\ 0\end{bmatrix}\begin{bmatrix}U\end{bmatrix} \tag{5.13}$$

where A, B, C are represented in (21), $\hat{X}$ is the kalman estimated state vector and U is the control output, $g = f(z_k, u_k)$ which is $\Delta\delta_k/Ibat_{ref}$, ω_k being the noise component represented as uncertainty, and D considered as zero. The optimal control policy with stochastic component can then be written as

$$\sum_{k=1}^{\infty}(X_k'^T \cdot Q'_k \cdot X'_k + U_k^T \cdot R_k \cdot U_k + \omega_k) \tag{5.14}$$

where Q'_k is the augmented state penalty factor corresponding to augmented state vector X'_k, and ω_k is the variance matrix of the stochastic noise component of the system.

5.4.1 Treatment of Uncertainty and Initial Calculation of B_k

Let us consider that there exist a certain amount of uncertainty in the control output U. We can account that to a sub-optimal LQR gains, Q'_k and R_k. If we decide to transfer all control uncertainties into the input vector, B_k. we can re-write the input vector as a sum of nominal input vector B_k^N and uncertain input vector B_k^U :

Hence, input matrix becomes:

$$B_k = B_k^N + B_k^U \tag{5.15}$$

Thus, the state vector equation can be written as:

$$X'_{k+1} = A'_k X'_k + B_k^N U_k + B_k^U U_k \tag{5.16}$$

Using the concept of Pseudo-Inverse, uncertainty control projections can be impressed into the range of input vector, B as follows:

$$B_k^U = B_k B_k^+ \tag{5.17}$$

$$B_k^N = B_k - B_k B_k^+ \tag{5.18}$$

where B_k^+ is $(B_k^T B_k)^{-1} B_k^T$. The uncertainty projections help us to determine the maximum limit of the control penalty factor, R. Whereas, the weighting factor on the output sets the minimum limit of the state penalty factor, Q.

5.4.2 Initialization of Penalty Factors, and Optimal Gain K

The pseudo-inverse of the input vector, B^+, shown above is used to initialize the control penalty factors of the HESS. Each storage device of HESS will have its penalty factor and will be updated based on their sensitivity to changes in PCC frequency as follows

$$(Z^{max})^T (B^+)^T B^+ (Z^{max}) \geq R_1, R_2 \tag{5.19}$$

where Z^{max} is the matrix of maximum control uncertainty which is considered as 100% and C is the output matrix of the state space, R_1 and R_2 are the penalty factors based on control uncertainty. Equation (5.19) initializes the penalty factors R_1 for battery and R_2 for ultra-capacitor storage systems, respectively. The penalty

factors can be arranged in the penalty matrix format as shown below:

$$R = \begin{bmatrix} R_1 & 0 \\ 0 & R_2 \end{bmatrix} \tag{5.20}$$

For (5.21) to (5.26), depending on the energy storage system that we are interested to solve the optimal control problem, the term R_k will updated with R_1 or R_2. Also, the state-space matrices (A_k, B_k, C_k) and $\hat{X}_k$ will change accordingly. Thus, to solve the optimal control problem for the entire HESS, two separate instances are performed. The algebraic Riccati solution is first initialized to an Identity matrix with an order equal to A_k.

$$P_{k-1} = I(n, n) \tag{5.21}$$

where n is the order A_k. Next, the state penalty factor, Q_k is initialized,

$$Q_{gain} C'^T C' \leq Q_k \tag{5.22}$$

where Q_{gain} is the output penalty gain. Algebraic Riccati solution is updated as

$$P_k = [P_{k-1} \cdot A_k + A_k^T \cdot P_{k-1} - P_{k-1} \cdot B_k \cdot R_k^{-1} \cdot B_k^T \cdot P_{k-1} + Q_k] \cdot T_c + P_{k-1} \tag{5.23}$$

where P_k is the discrete derivative of the Algebraic Riccati Solution matrix, A'_k, B_k and C_k are the state transition, input and output matrices respectively. K_k is calculated as

$$K_k = R_k^{-1} \cdot B_k^T \cdot P_k \tag{5.24}$$

and the feedback control law will be

$$U_k = -K_k X'_k \tag{5.25}$$

The closed loop system based on the feedback control law is

$$\dot{X}'_k = A'_k X'_k - (B_k^N + B_k^U) K_k X'_k \tag{5.26}$$

5.4.3 Updates on Penalty Factors

The state penalty factor is updated using P_k as

$$\Delta Q = -\dot{P}_k - P_k A_k - A_k^T P_k + P_k B_k R_k^{-1} B_k^T P_k \tag{5.27}$$

$$Q_{k+1} = Q_k + \Delta Q \tag{5.28}$$

where ΔQ is the state penalty factor update and Q_{k+1} is the penalty factor for next time step.

Updates on control penalty factors for each of the dispatch-able HESS devices are deduced by a function of grid frequency sensitivity to the rate of change of power from each energy storage device (ramp rate). Thus R_1 and R_2 initialized in (5.19) are updated as follows:

$$\frac{df_{pcc}}{dP_{bat}} = \frac{f_{pcc}(k) - f_{pcc}(k-1)}{P_{bat}(k) - P_{bat}(k-1)} \tag{5.29}$$

$$\frac{df_{pcc}}{dP_{uc}} = \frac{f_{pcc}(k) - f_{pcc}(k-1)}{P_{uc}(k) - P_{uc}(k-1)} \tag{5.30}$$

$$\Delta R_1 = \mid \frac{df_{pcc}}{dP_{bat}} \mid \tag{5.31}$$

$$\Delta R_2 = \mid \frac{df_{pcc}}{dP_{uc}} \mid \tag{5.32}$$

$$R_1 = R_1 \mp \Delta R_1, \quad \text{when} \quad \frac{d \mid \frac{df_{pcc}}{dP_{bat}} \mid}{dt} \neq 0 \tag{5.33}$$

$$R_2 = R_2 \mp \Delta R_2, \quad \text{when} \quad \frac{d \mid \frac{df_{pcc}}{dP_{uc}} \mid}{dt} \neq 0 \tag{5.34}$$

where $f_{pcc}(k)$ and $f_{pcc}(k-1)$ are the frequency values at PCC at a discrete time-steps k and $k-1$, respectively, $P_{bat}(k)$ and $P_{bat}(k-1)$ are the battery power values at a discrete time-steps k and $k-1$, respectively and so on. $\mid \frac{df_{pcc}}{dP_{bat}} \mid$ is the absolute sensitivity of PCC frequency to battery energy storage power output and $\mid \frac{df_{pcc}}{dP_{uc}} \mid$ is the absolute sensitivity of PCC frequency to ultra-capacitor energy storage power output. This represent a generic form of uncertain optimal control.

5.5 Simulation Results and Discussions

Simulation is performed on the IEEE 123 bus test feeder. This test feeder is a medium-size network with multiple load regulators and shunt capacitors. It is characterized by unbalanced loading, and switches to alternate the power-flow path. The details of the power grid are discussed in [75]. A modified IEEE 123 bus distribution system that consists of a synchronous generator model as a slack bus, and two DC microgrids as shown in Fig. 5.4 is used as a test system to draw a comparison of results with the conventional frequency-droop approach and optimal control based on non-updating gains. Four different grid events are studied to document a comprehensive case study for the proposed architecture. Figure 5.4 showcases bus 51 with a red marker where the events are tested. The 4 cases are itemized as follows:

- Case I: Line-to-Ground Fault (LG)
- Case II: Line-to-Line-to-Ground Fault (LLG)
- Case III: Line-to-Line-to-Line-to-Ground Fault (LLLG)
- Case IV: Step loading (Step)

Cases I-III from Fig. 5.4 are simulated for 0.18 seconds on bus 51 between phase and ground with fault and ground resistance both being 1 Ω. Please note that for this case the pre-fault and post-fault conditions are the same. As shown in Fig. 5.4. with green markers, micro-grids are placed at bus 300 and bus 86 respectively. The

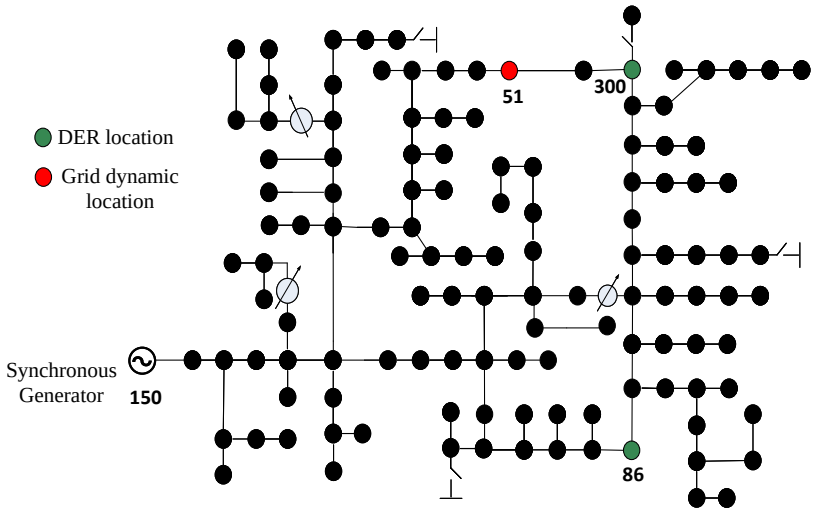

Figure 5.4: Modified IEEE 123 bus test bench for robust optimal control.

scattered placement of the micro-grids is to study the effect of fault events on the voltage angle (δ) at the PCC of the respective micro-grids.

The voltage angle at PCC (δ) changes for each micro-grid in response to the grid dynamics induced by the fault event. The proposed approach operates to minimize the angle deviation ($\Delta\delta$) using a dynamic optimal control.

Case studies for various grid dynamics show a comparison of the inertial and secondary frequency response of 4 different approaches. For all the graphs depicting case results, $Fdefault$ represents the default frequency response of the 123 bus synchronous generator. $Fdroop$ is the frequency-droop response for the combined effect of micro-grids at bus 300 (considered micro-grid 1 for denotation) and 86 (considered micro-grid 2 for denotation). $FstaticLQR$ is the conventional minimization-based optimal control response for 2-micro-grid simulation, whereas, $FdynLQR$ is the frequency regulation obtained by using dynamically updating optimal control solution matrix P and ramp function based optimal control penalty factor R.

5.5.1 Case I : Line-to-Ground Fault (LG)

The simulation results for the LG case can be observed from Fig. 5.5-5.7. Fig. 5.5 shows that utilization of uncertainty-based robust optimal control improves the settling time of secondary response by 21 seconds when compared to the result from conventional optimal control and by 46 seconds against the conventional frequency-droop approach. Similarly, the proposed approach performs the best by allowing frequency nadir to drop only to 59.96 Hz. This is a 0.1 Hz improvement when compared to the conventional LQR approach. The conventional droop approach showcases the second-best inertial response at 59.89 Hz whereas the default system nadir drops the most. Subplot 1 of Fig. 5.5 shows the PCC angles of micro-grids post-fault close to its pre-fault value. The proposed approach's eventual objective is frequency regulation which is shown in subplot 2 of Fig. 5.5. As soon as the frequency comes close to regulation the control quickly prioritizes frequency regulation instead of error minimization. Fig. 5.6 and Fig. 5.7 showcase the performance contribution of dynamically updated parameters of optimal control. The control penalty factor for battery and UC update is based on the sensitivity of the individual dispatch-able device to changes in frequency. Fig. 5.6 summarizes the comparison of the per-unit control outputs using all the frequency regulation approaches tested for the system under study. Fig. 5.7 shows the penalty factor updates for battery and ultra-capacitor systems operating through bus 300 ($R1_{BAT}$, $R1_{UC}$) and bus 86 ($R2_{BAT}$, $R2_{UC}$). It can be observed that the ultra-capacitor systems for both micro-grids ramps at a similar rate and hence have the same penalty factor update. The effect of this is evident in Fig. 5.6, where $UC1DL$ and $UC2DL$ (the two ultra-capacitor systems) have the same output. In the case of the battery systems, the one connected in the micro-grid at bus 86 has higher sensitivity to changing frequency as compared to the one connected at bus 300. This can also be seen in the per-unit control outputs in Fig. 5.6.

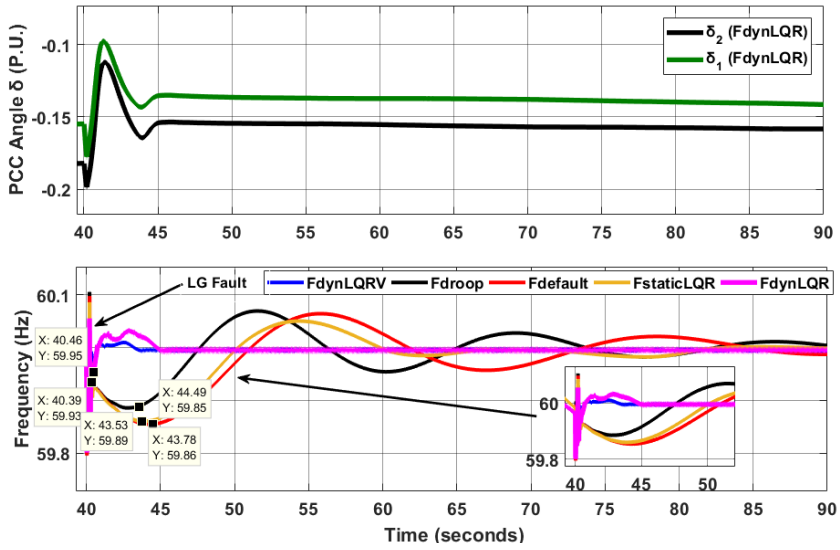

Figure 5.5: Frequency and δ for LG fault a) PCC angle b) Frequency.

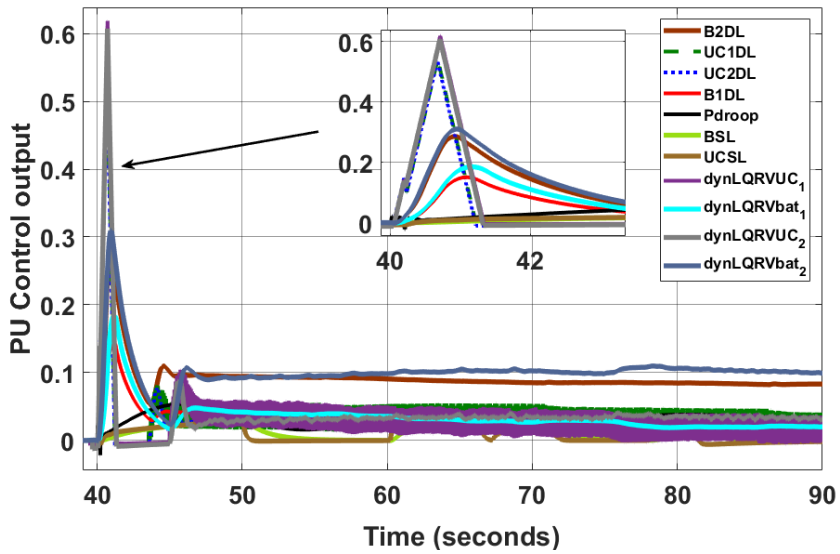

Figure 5.6: Per Unit control output for various frequency regulation approaches.

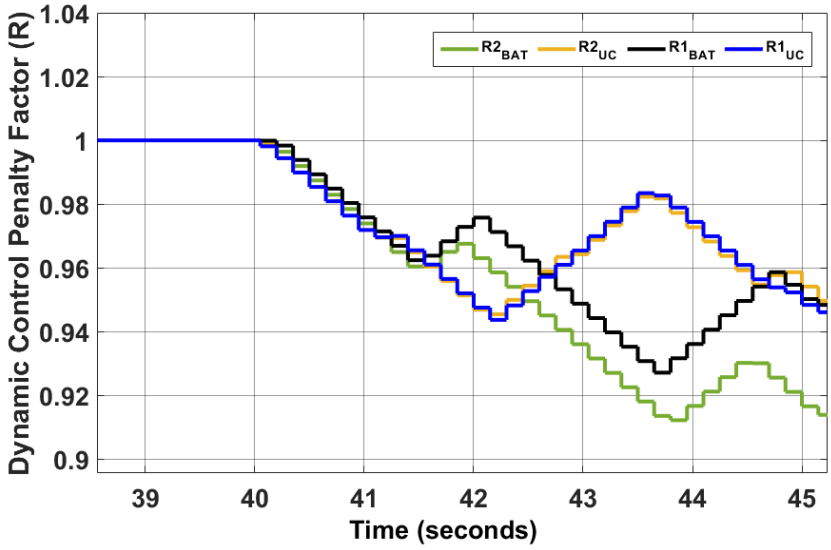

Figure 5.7: Ramp function based control penalty factor R for LG fault case

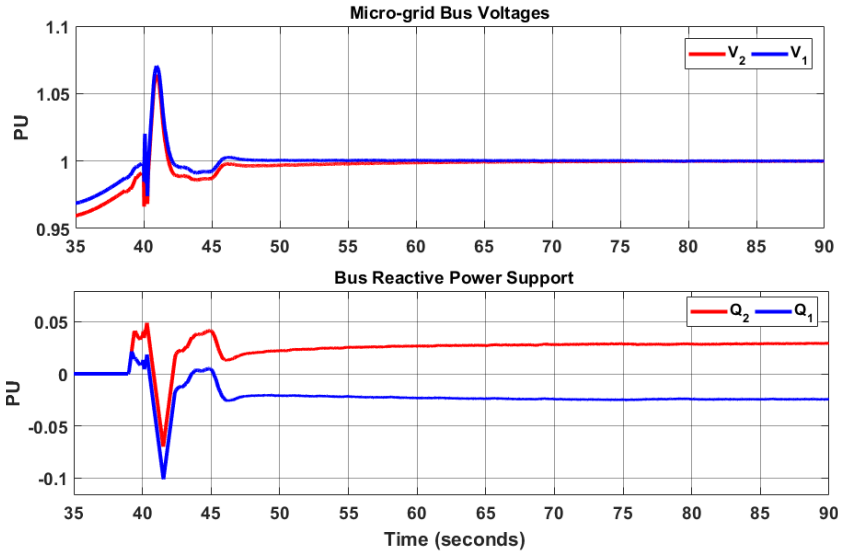

Figure 5.8: Reactive Power support using PCC voltage control for LG case

5.5.2 Case II: Line-to-Line-to-Ground Fault (LLG)

For the LLG case, the conventional LQR shows the best performance by frequency nadir to reach only 59.59 Hz. The proposed approach comes second-best by allowing the nadir to drop 0.04 Hz lower than conventional optimal control (static LQR). It is followed by a frequency droop approach at 59.54 Hz. As far as settling time is concerned the proposed approach settles the fastest in 48.33 seconds, whereas conventional LQR and frequency droop approach settles at 90 and 105 seconds, respectively. Fig. 5.9 shows the frequency regulation whereas fig. 5.10 show the power shared by dispatch-able energy storage devices for various approaches. From fig. 5.10 it can be observed that the proposed approach responds with a faster change in power shared by battery and ultra-capacitor devices due to dynamically updated penalty factors. Even though the frequency nadir response for various approaches is comparable, the proposed approach performs faster settling due to a higher power supply during the settling response of frequency.

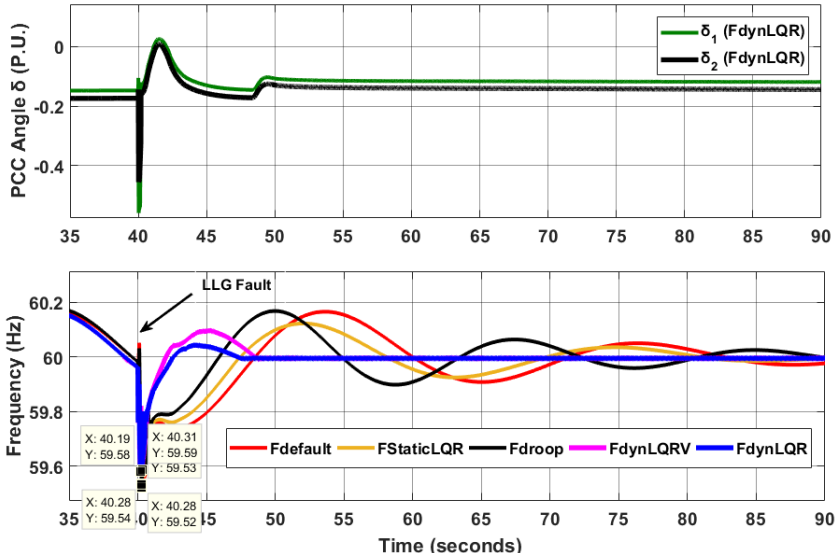

Figure 5.9: Frequency and δ for LLG fault a) PCC angle b) Frequency.

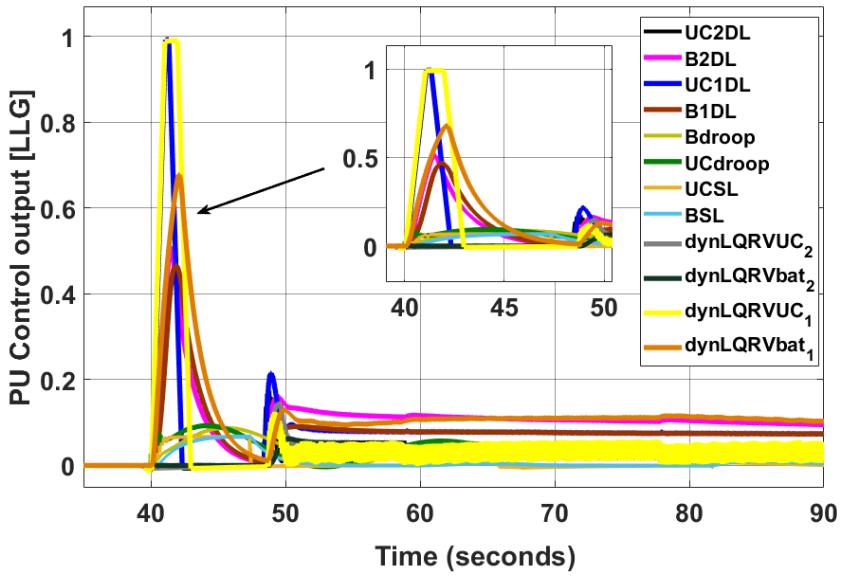

Figure 5.10: Per Unit control output for various frequency regulation approaches for LLG event

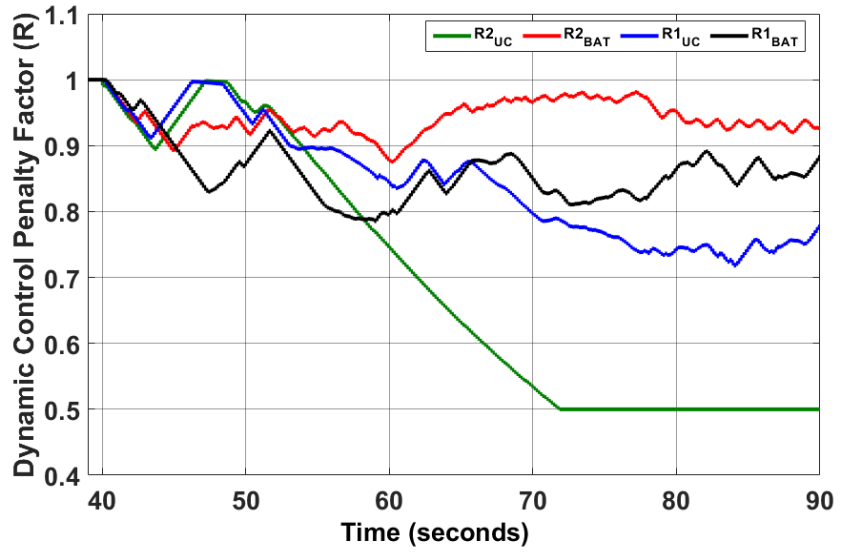

Figure 5.11: Ramp function based control penalty factor R for LLG fault case

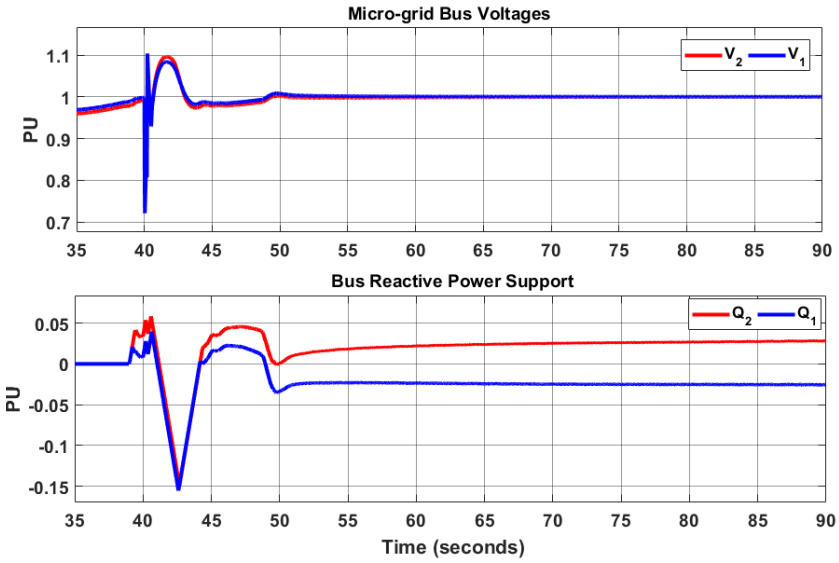

Figure 5.12: Reactive Power support using PCC voltage control for LLG case

5.5.3 Case III: Line-to-Line-to-Line-to-Ground Fault (LLLG)

In the case of the LLLG fault event, the proposed dynamic optimal control shows 6.9% improvement in frequency nadir compared to the default response of the system. This is a 4.5% improvement compared to the frequency droop approach. The proposed optimal control settles 65 seconds faster than the default response, 37 seconds faster than conventional optimal control, and 60 seconds faster than the frequency droop approach. Thus, the proposed dynamic optimal control approach shows a significant improvement in the settling time of frequency. Fig. 5.13 shows the frequency response for various approaches. Fig. 5.14 describes the contribution of per unit power from each storage device for various approaches. It can be observed for the proposed approach that the HESS connected at bus 300 (UC1DL, B1DL) supply more power compared to that at connected at bus 86. This is because the LLLG fault event is closer to bus 300 and hence the angle at bus 300, δ_1 of fig. 5.13 subplot 1 show a higher deviation compared to δ_2.

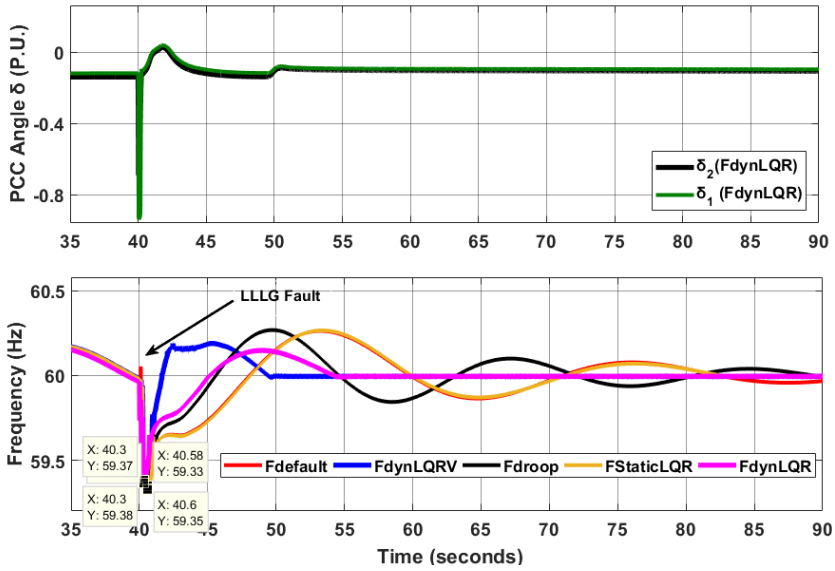

Figure 5.13: Frequency and δ for LLLG fault a) PCC angle b) Frequency.

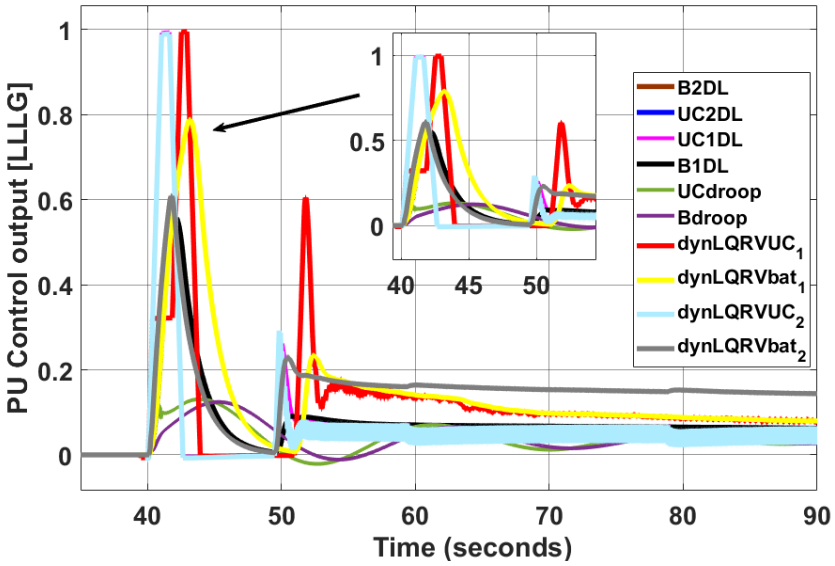

Figure 5.14: Per Unit control output for various frequency regulation approaches for LLLG event.

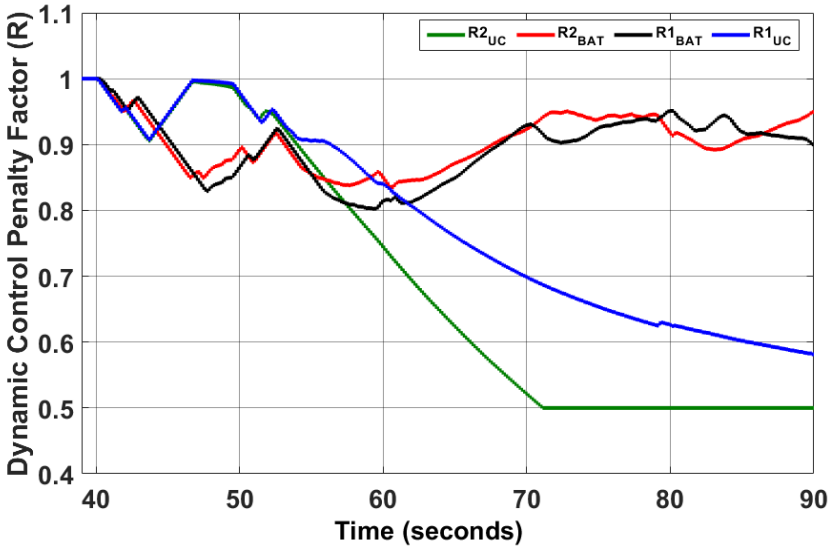

Figure 5.15: Ramp function based control penalty factor R for LLLG fault case

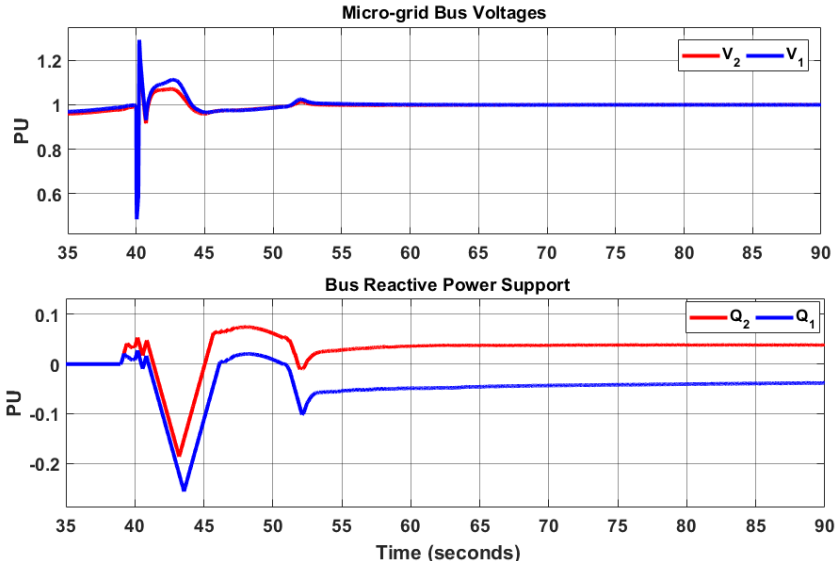

Figure 5.16: Reactive Power support using PCC voltage control for LLLG case

5.5.4 Case IV : Step loading (Step)

Fig. 5.17 and fig. 5.18 show the frequency, angles, and power-sharing for various approaches for the step loading case. A step change of 1400 kW of unbalanced load at bus 51 results in a frequency nadir of 59.84 Hz with the proposed dynamic optimal control approach. This is a 0.2 Hz improvement when compared to both conventional optimal control and frequency droop approaches. The settling time for the proposed approach is also 17 seconds and 31 seconds faster than conventional optimal control and frequency droop approaches, respectively. The proposed approach settles at 43.31 seconds whereas the default response of the system settles at 84 seconds. Similar to the power-sharing graph from the LLLG case, the share of power is higher for the proposed dynamic optimal control from the HESS closest to the fault location (B1DL, UC1DL). These devices also provide significant power for improved settling between 50 and 90 seconds.

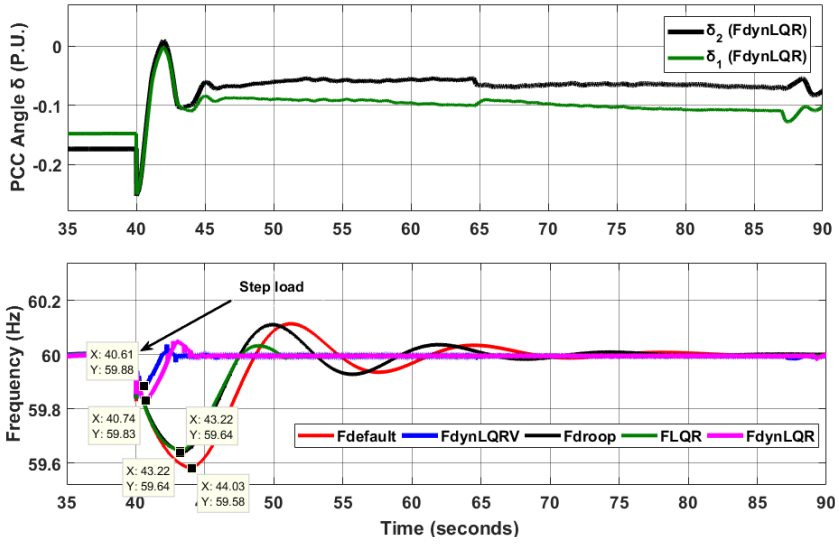

Figure 5.17: Frequency and δ for step loading case a) PCC angle b) Frequency.

Table 5.1 summarizes the performance comparisons between the frequency regulation approaches discussed in this optimal control. The following abbreviations are used for this table: CA is Control Approach, FN is Frequency Nadir, ST is settling

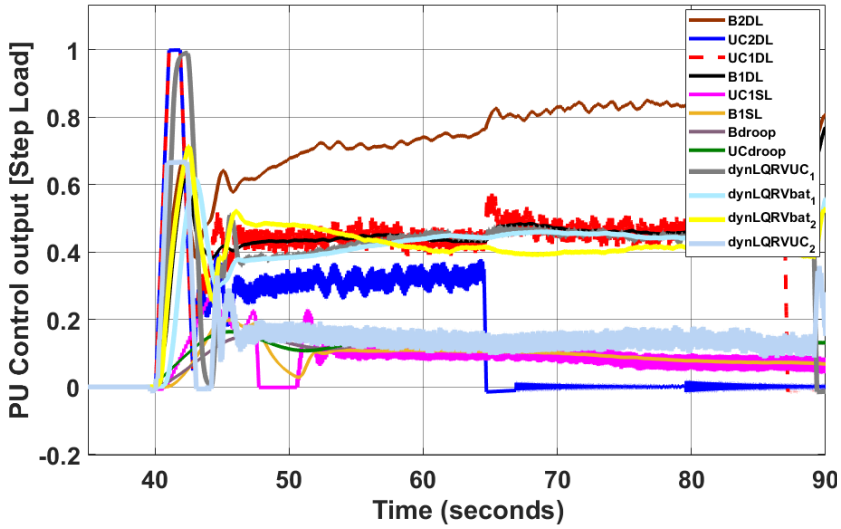

Figure 5.18: Per Unit control output for various frequency regulation approaches for step loading case.

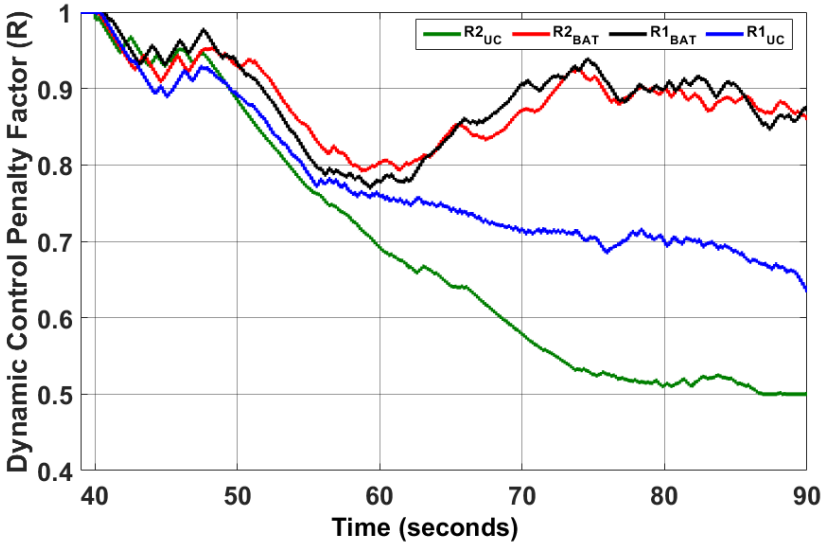

Figure 5.19: Ramp function based control penalty factor R for step loading case

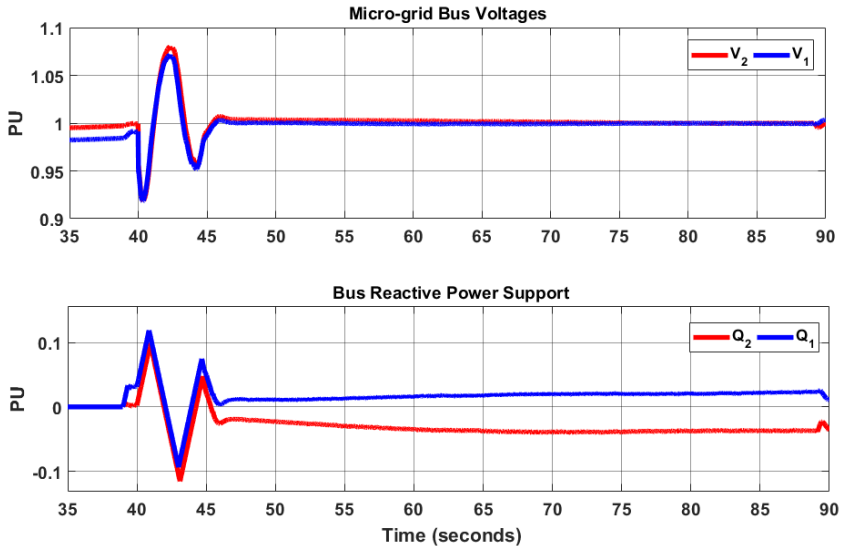

Figure 5.20: Reactive Power support using PCC voltage control for step loading case

Table 5.1: Results on Modified 123 bus network

Event	CA	FN (Hz)	Imp Vs MBS	ST (s)	Imp Vs MBS
LG fault	MBS	59.85	-	115	-
	PDLQRV	59.95	73.33%	43	72
	PDLQR	59.93	65.33%	44	71
	SLQR	59.86	6.8%	65	50
	FD	59.89	26.66%	90	25
LLG fault	MBS	59.52	-	115	-
	PDLQRV	59.58	5.92%	46.33	68.67
	PDLQR	59.55	2.08%	48.33	66.67
	SLQR	59.59	6.25%	90	25
	FD	59.54	4.16%	105	10
LLLG fault	MBS	59.33	-	115	-
	PDLQRV	59.38	6.9%	48	67
	PDLQR	59.37	4.6%	54	61
	SLQR	59.33	-	87	28
	FD	59.35	2.4%	110	5
Step loading	MBS	59.58	-	84	-
	PDLQRV	59.88	67.9%	42.4	41.6
	PDLQR	59.83	56.9%	43.31	40.69
	SLQR	59.64	14.28%	50.95	23.95
	FD	59.64	14.28%	75.70	8.30

time, Imp Vs MBS is Improvement versus Modified Bus System, PDLQRV is Proposed Dynamic LQR with Voltage support, SLQR is static (conventional) LQR, FD is Frequency Droop, MBS is Modified Bus System.

5.6 Summary of Proposed Uncertainty based Optimal Control

Results for micro-grids at bus 300 and bus 86 based on the four case studies indicate that the uncertainty-based optimal control improves both inertial and secondary frequency response compared to both the non-updating $\Delta\delta$ minimization optimal control and conventional frequency-droop approach. On adding the reactive power support for PCC voltage regulation, the proposed uncertainty-based optimal control further improves frequency nadir. The proposed approach also distributes power more efficiently amongst dispatch-able HESS devices based on their respective sensitivities to change in frequency. Such an approach also has the advantage of being modular and inherently compatible with multi-micro-grid networks.

CHAPTER 6: GLOBALLY OPTIMIZED FREQUENCY REGULATION USING ADMM APPROACH FOR MULTI-MICRO-GRIDS

This paper proposes a novel approach for globally optimized frequency regulation performed by multi-micro-grids based on Point of Common Coupling (PCC) angle minimization. The proposed approach utilizes the Alternating Direction Method of Multipliers (ADMM) based Multiple Input Multiple Output (MIMO) system analysis to generate individual transfer functions relating dispatch-able Distributed Energy Resource (DER) set points which are control inputs and grid frequency/individual PCC angles (δ) for AD-DC multi-micro-grid structures depending on their locations in the distribution network. Transfer functions generated by the MIMO identification also provide a measure of the sensitivity of powers with respect to change in global distribution frequency or individual angle δ for each section of AC-DC multi-micro-grid. This approach coordinates the power-sharing between each micro-grid such that the dispatch-able DER set to point to supply for a commonly seen fault/dynamic is globally optimized.

6.1 Introduction

The approach discusses in the previous chapter suits well for individual micro-grids as the optimization is limited to individual $\Delta\delta$ occurring at that bus in a distribution like the modified 123 bus system. However, if we consider the case wherein there are multiple micro-grids in the distribution system, we will need to coordinate the power-sharing between each micro-grid such that the active power set to point to supply for a commonly seen fault/dynamic is globally optimized. To achieve such a globally optimized operating condition it is essential to develop an aggregated state

space of all the micro-grids involved in supporting the event.

This is provided by a tool known as the Alternating Direction Method of Multipliers (ADMM) which gives a dynamically updating, Identification-based Multi-Input Multi-Output (MIMO) system for analysis and control. Like LQR, the ADMM approach also specializes in multi-agent systems where a large number of complex subsystems are connected and operate in coordination. The entire system can be summarized by using a MIMO state-space representation such that interaction for every possible combination of inputs and outputs can be quantified using an input-to-output transfer function. An asynchronous and distributed alternating direction method of multipliers (ADMM) algorithm is discussed in [106] for a MAS-based micro-grid to solve and optimize the overall energy cost represented as a sum of locally observable convex functions. Examples of energy management systems relying on ADMM consensus can be seen in [107] and [108] where the operational cost of the system is minimized to derive profits from energy exchanges in micro-grids. In [109] a centralized convex optimization problem of a microgrid with distributed energy resources is decomposed into sub-problems solved iteratively by the respective agents in a distributive manner using privacy-preserving asynchronous alternating direction method of multipliers (ADMM) algorithm. Optimal Power Flow is an example of non-convex optimization, but ADMM used in [110] uses difference-of-convex programming (DCP) to solve the nonconvex Optimal Power Flow (OPF) problem in a distributed way for a DC micro-grid. For AC micro-grid synchronization, [111] presents a recursive algorithm to restore synchronization in voltage and frequency using ADMM by casting the synchronization phenomena in inverter-based ac microgrids as an optimization problem solved using the alternating direction method of multipliers (ADMM). For economic dispatch problem (EDP) of island micro-grid, [112] proposes a distributed optimization strategy based on alternating direction multiplier method(ADMM). The strategy takes the maximization of the MG system benefit as the objective function.

On similar lines, authors of [113] solve the EDP with general convex cost functions based on an alternating direction method of multipliers (ADMM) for islanded micro-grid. Some other EDP and OPF problems and approaches are discussed in [114], [115] and [116]. ADMM is also used for droop approaches like in [117], where a consensus-based distributed droop control of VSGs for isolated AC micro-grids is proposed. To improve on convergence rate and the noise resilience in distributed droop control authors of [118] implement consensus-based distributed droop control by the alternating direction multipliers method. Authors of [104] present a novel approach to power-sharing methodology for parallel-connected single-phase inverters (SPIs) using Alternating Direction Method of Multipliers (ADMM) based identification of multiple inputs and multiple-output (MIMO) system and its optimal control.

Two approaches of frequency regulation will be studied in this chapter, namely frequency-droop and ADMM based $\Delta\delta$ minimization. ADMM based multiple-input multiple-output (MIMO) identification method will be used to generate individual transfer functions relating to inverter active power which are input control sources and grid frequency/ individual $\Delta\delta$ for micro-grid depending on their locations in the power grid. Transfer functions generated by the MIMO identification also provide a measure of the sensitivity of powers with respect to change in global distribution frequency or individual $\Delta\delta$ angle for each micro-grid.

6.2 Research Contributions

This chapter proposes ADMM based Multi-Input-Multi-Output (MIMO) system optimization, that can find an optimal control consensus amongst multiple micro-grid in performing a common objective of supporting frequency regulation. The system under test is a DC-AC hybrid micro-grid that includes a novel DC Ring architecture capable of emulating a DC topology-based residential community. Key highlights of this chapter are:

- A comprehensive DC-AC micro-grid model with distributed DERs connected

in a proposed DC ring structure that can emulate a DC-topology-connected residential community.

- Model validation with modified IEEE 123 bus distribution system acting as AC section of the proposed DC-AC micro-grid.
- High order ADMM based MIMO identification of the DC-AC micro-grid with transfer functions for all possible combinations of inputs and outputs.
- Global consensus optimization-based set-points for all DERs connected in micro-grid for frequency regulation.
- Quantitative comparison of frequency-droop approach and the proposed $\Delta\delta$ minimization approach for multi-micro-grid operation based on globally optimized set-points.

6.3 Overall Architecture and the DC Ring Design

To simulate the scenario of multi-micro-grids connected in a DC-AC hybrid topology a DC Ring structure consisting of 4 DERs is considered. Each DER consists of a PV farm and HESS comprising of high energy density battery and high power density UC devices. The size of each PV farm is 1 MW and HESS consisting of 600 kWh battery and 400 kW UC bank. Each DER represents 35 residential households, thus the entire DC ring can be considered an electrical equivalent model of a residential community (4 MW). The DC ring is connected to 2 identical 3-ph $d-q$ inverters. Each inverter is designed for 4 MW size to also account for any reactive power demand by the hierarchical control. The primary objective of the inverter is to relay the power generated by the DC ring (Active Power) to the AC side of the network. The modified 123 bus system shown in fig. 6.4 is used as AC interconnected for the inverters. The inverters connect the modified 123 bus system with a DC ring at two locations, namely bus 18 and bus 86. The DC-AC hybrid topology consists

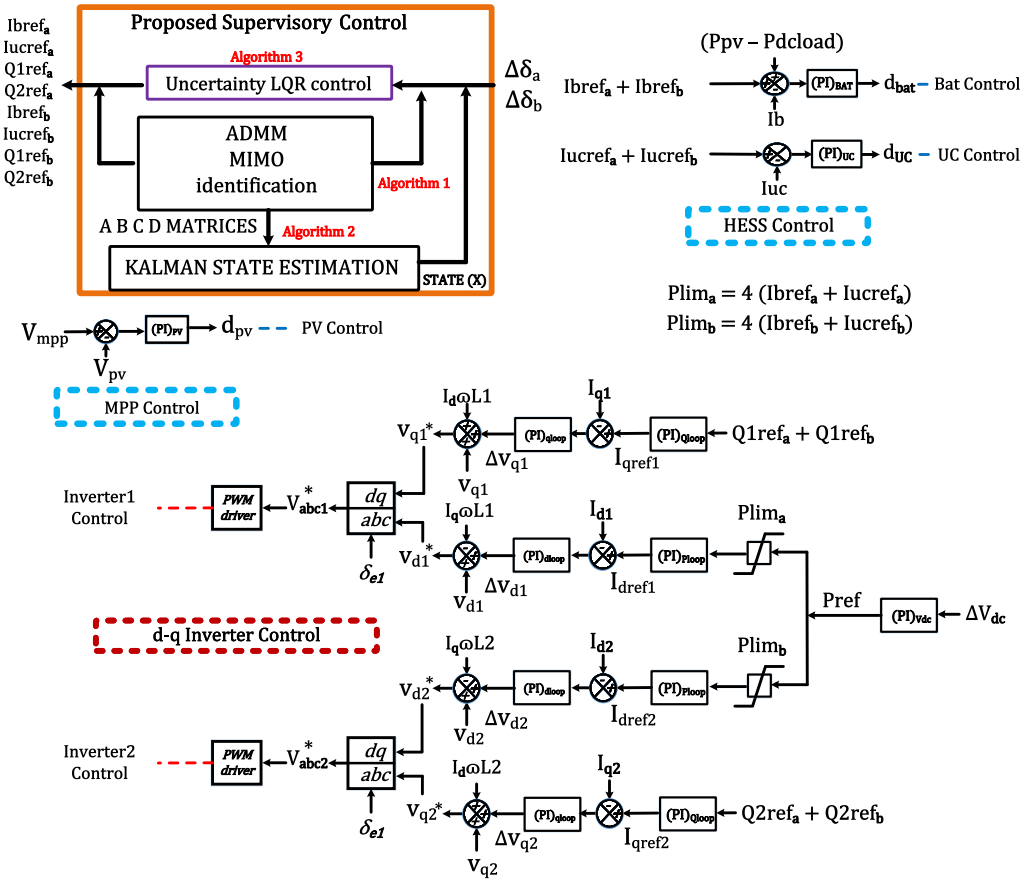

Figure 6.1: Proposed Control Architecture for DC Ring Structure.

of 2 output angle deviations and a total of 8 dispatch-able power sources (1 battery and 1 UC source in each DER). In addition to that, each inverter will have 1 reactive power reference available (Q-control). Thus, the ADMM MIMO will need to identify a total of 20 transfer function combinations. To avoid computational burden on the system, each DER will be given identical sets of power references from the proposed architecture, thus reducing the transfer function combinations to 8. The proposed control architecture is summarized in Fig. 6.1. The detailed input-output ADMM MIMO identification is shown in Fig. 6.3.

6.4 ADMM Based MIMO transfer function identification

Our system under test consists of 2 inverters connected on buses 18 and 86 of the modified 123 bus system and a DC ring structure with 4 DERs (DC micro-grids).

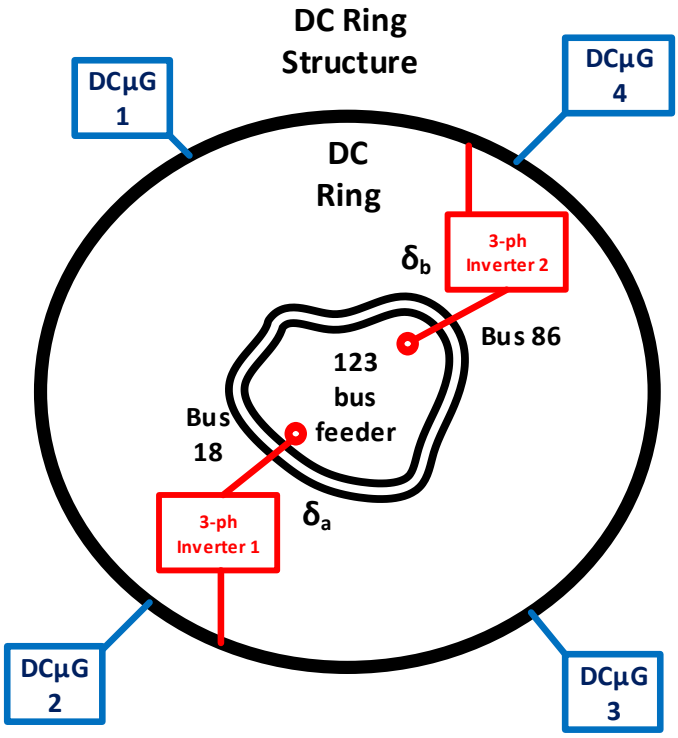

Figure 6.2: DC-AC hybrid topology test bench using DC Ring and modified 123 bus feeder.

MIMO identification using ADMM will consist of system identified outputs ($\Delta\delta_a$) and ($\Delta\delta_b$). The system inputs will be Ib_a, Iuc_a, $Q1_a$, $Q2_a$ dedicated for control of angle deviation for inverter 1 and Ib_b, Iuc_b, $Q1_b$, $Q2_b$ for that of inverter 2.

where, ($\Delta\delta_a$) is the angular deviation at inverter 1 PCC in degrees, Ib_a and Iuc_a are the per-unit battery and UC current/power outputs from each DER of the DC ring contributing to mitigate ($\Delta\delta_a$) at inverter 1. ($\Delta\delta_b$) is the angular deviation at inverter 2 PCC in degrees, Ib_b and Iuc_b are the per-unit battery and UC current/power outputs from each DER of the DC ring contributing to mitigate ($\Delta\delta_b$) at inverter 2.

Fig 6.3 summarizes the process of MIMO identification using ADMM and the resultant ABCD matrices for each identified transfer function combination. The identified transfer function matrix in equation 6.1 represents transfer functions for all the possible input-output combinations.

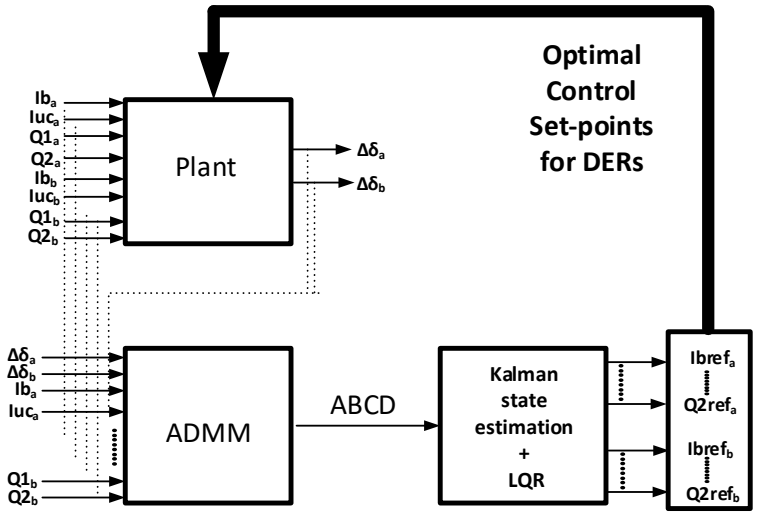

Figure 6.3: ADMM MIMO Identification and Kalman-LQR based optimal control set-points for DERs.

Where m equals the number of outputs and n equals the number of system inputs.

For 2 outputs and 4 inputs, there are 8 sets of ABCD matrices corresponding to the identified transfer function combinations. This assimilates the relationship of one output to every available input of the system.

$$\begin{bmatrix} \Delta\delta_a(z) \\ \Delta\delta_b(z) \end{bmatrix} = \begin{bmatrix} G_{11}(z) & G_{12}(z) & G_{13}(z) & G_{14}(z) \\ G_{21}(z) & G_{22}(z) & G_{23}(z) & G_{24}(z) \end{bmatrix} \begin{bmatrix} Ib_a(z) \\ Iuc_a(z) \\ Q1_a(z) \\ Q2_a(z) \\ Ib_b(z) \\ Iuc_b(z) \\ Q1_b(z) \\ Q2_b(z) \end{bmatrix} \tag{6.1}$$

and generalized as

$$\underset{m\times 1}{P(z)} = \underset{m\times n}{G(z)}\ \underset{n\times 1}{U(z)} \tag{6.2}$$

Based on the MIMO transfer functions, the individual transfer functions $(G_{11}, G_{12}, ., G_{24})$ can be represented as

$$G_{11} = \frac{\Delta\delta_a}{Ib_a} = \frac{b_0^{Ib_a} + b_1^{Ib_a} z^{-1} + ... + b_k^{Ib_a} z^{-k}}{1 + a_1^{Ib_a} z^{-1} + a_2^{Ib_a} z^{-2} + ... + a_k^{Ib_a} z^{-k}} \tag{6.3}$$

$$G_{12} = \frac{\Delta\delta_a}{Iuc_a} = \frac{b_0^{Iuc_a} + b_1^{Iuc_a} z^{-1} + ... + b_k^{Iuc_a} z^{-k}}{1 + a_1^{Iuc_a} z^{-1} + a_2^{Iuc_a} z^{-2} + ... + a_k^{Iuc_a} z^{-k}} \tag{6.4}$$

$$G_{24} = \frac{\Delta\delta_b}{Q2_b} = \frac{b_0^{Q2_b} + b_1^{Q2_b} z^{-1} + ... + b_k^{Q2_b} z^{-k}}{1 + a_1^{Q2_b} z^{-1} + a_2^{Q2_b} z^{-2} + ... + a_k^{Q2_b} z^{-k}} \tag{6.5}$$

where b_0, b_1...,b_k are the numerator coefficients of the transfer functions and a_1,a_2...a_k are the denominator coefficients of the transfer functions. ADMM method uses least squares method to first estimate the individual transfer functions and reach a global consensus problem.

Then a global consensus optimization problem can be formulated as:

$$\min_{a^{Ib_a}..a^{Q2_b}} \frac{1}{2}||[P][a] - [B] + [P_x][b]||^2 \tag{6.6}$$

where a is a vector of all the denominator coefficients and b is the vector of all the numerator coefficients. also, B is the matrix of the current samples of I_{mn}, P is the matrix of the previous samples of $\Delta\delta_m$ and P_x are the previous samples of I_{mn}. The objective is to make a^{Ib_a}=a^{Iuc_a}...=a^{Q2_b}=z for a global consensus problem, so the numerator and denominator coefficients are calculated iteratively till the objective is achieved.

This method provides online ADMM based MIMO identification of the dynamically changing state space of the AC-DC multi-micro-grid. A_{ss}, B_{ss} and C_{ss} matrices (D_{ss}

Algorithm 8 ADMM MIMO Identification Algorithm

Step: 1 Populate 400 samples of data for Ib_a, Iuc_a, $Q1_a$, $Q2_a$, Ib_b, Iuc_b, $Q1_b$, $Q2_b$ and $(\Delta\delta_a)$, $(\Delta\delta_b)$ to create input and output vector for identification.

Step: 2 Calculate the numerators and denominators of each individual transfer function for every output with respect to each input.

Step: 3 Arrange the vectors in least squares format

Step: 4 Solve iteratively to form $a^{Ib_a} = a^{Iuc_a} .... = a^{Q2_b} = z$ by using b's.

Step: 5 Obtain the global consensus solution (when all a's are equal)

Step: 6 Compute the ABCD , A_{ss}, B_{ss} and C_{ss} matrices ($D_{ss} = 0$) matrices for the individual transfer functions.

$= 0$) obtained as a result of this method can be further utilized to calculate the optimal gain using LQR algorithm for individual DER set points.

To obtain the dynamic state vector, X(k), we use Kalman estimation online in the same calling function that processes the LQR routine. Algorithm 9 details the step-wise process of estimating the state of interest ($\Delta\delta$) from the dynamic state space. The state estimate from Algorithm 9 is used to calculate the optimal control output of LQR. LQR gain (K_{LQR}) for every sample is calculated using a 2-step process given in Algorithm 10, which gives the optimal control output, $Ibat\_ref$.

6.5 Validation on Modified IEEE 123 bus network

To test the global consensus-based ADMM approach for frequency regulation we implement the proposed architecture with the IEEE 123 bus distribution test feeder. The feeder is modified by adding a synchronous generator on bus 149 such that it can generate its response to grid dynamics. This response will be considered as a base case for comparison purposes. To validate the proposed architecture, the DC ring structure is shown in Fig. 6.2 is connected to buses 18 and 86 on the modified IEEE 123 bus system through identical 3-phase $d-q$ inverters. For the case study, a step loading condition (SL) (Case I) and a Line-to-Ground fault event (LG) (Case II) is

Algorithm 9 Kalman State Estimation

Step: 1 Initialize Matrices $\hat{X_{ke}}$, P_{ke}, Q_{ke}, K_{ke}, R_{ke}, Res

Step: 2 Collect $(Ibat\_ref)$ and $(\Delta\delta)$ samples and arrange in Matrices U and y respectively, include the RLS identified state space matrices A_{ss}, B_{ss}, C_{ss}

Step: 3 Calculate the initial estimate of states $\hat{X_{ke}}$

$$\hat{X_{ke}}(k) = A_{ss}(k) \cdot \hat{X_{ke}}(k-1) + B_{ss}(k) \cdot U(k)$$

Step: 4 Calculate the Error Co-variance Estimate

$$P_{ke}(k) = A_{ss}(k) \cdot P_{ke}(k-1) \cdot A_{ss}^{T}(k) + Q_{ke}$$

Step: 5 Calculate the Kalman Gain :

$$K_{ke}(k) = \frac{P_{ke}(k) \cdot C_{ss}^{T}(k)}{C_{ss}(k) \cdot P_{ke}(k) \cdot C_{ss}^{T}(k) + R_{ke}}$$

Step: 6 Calculate the measurement residue

$$Res(k) = y(k) - C_{ss}(k) * \hat{X_{ke}}(k)$$

Step: 7 Update the Error Co-variance Estimate

$$P_{ke}(k) = [I - K_{ke}(k) \cdot C_{ss}(k)] \cdot P_{ke}(k)$$

Step: 8 Update the State Co-variance Estimate

$$\hat{X_{ke}}(k) = \hat{X_{ke}}(k) + K_{ke}(k) \cdot Res(k)$$

Algorithm 10 Uncertainty based Linear Quadratic Regulator Control

Step: 1 Extract RLS identified state space matrices A_{ss}, B_{ss}, C_{ss} and Kalman Estimate $\hat{X_{ke}}$

Step: 2 Set Control and state penalty factors using equations and initialize Algebraic Riccati Solution $P_{lqr}(k-1)$ and the time period of the LQR call function in simulation, T_c

$$Q_{lqr}(k) \geq Q_{gain} C'^T C'$$

$$R_{lqr} \leq (Z^{max})^T (B^+)^T B^+ (Z^{max})$$

Step: 3 Solve for Algebraic Riccati Equation

$$\begin{aligned} P_{lqr}(k) = [P_{lqr}(k-1) \cdot A_{ss}(k) + A_{ss}^T(k) \cdot P_{lqr}(k-1) \\ - P_{lqr}(k-1) \cdot B_{ss}(k) \cdot R_{lqr}^{-1}(k) \cdot B_{ss}^T(k) \\ \cdot P_{lqr}(k-1) + Q_{lqr}(k)] \cdot T_c + P_{lqr}(k-1) \end{aligned}$$

step: 4 Update Control penalty factor based on storage device's sensitivity to angle deviation.

$$R = R \pm \Delta R$$

Step: 5 Find LQR gain K_{lqr} for k^{th} time

$$K_{lqr}(k) = R_{lqr}^{-1} \cdot B_{ss}^T(k) \cdot P_{lqr}(k)$$

Step: 6 The optimal control output $Ibat\_ref$ is given by:

$$Ibat\_ref(k) = -K_{lqr}(k) \cdot \hat{X_{ke}}(k)$$

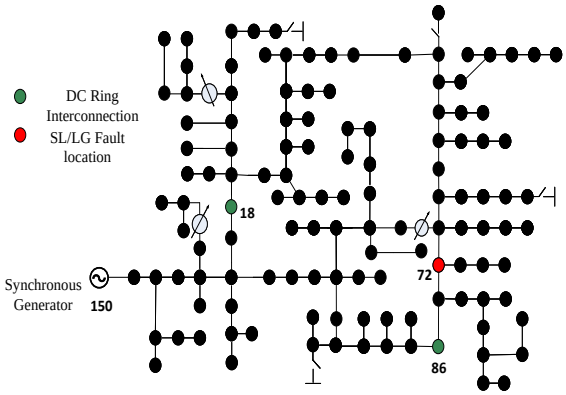

Figure 6.4: DC Ring interconnection on the modified 123 bus feeder.

Table 6.1: Results on Modified 123 bus system

	Par.	MBS	MBSFD	Imp.	MBSCOpt	Imp.
Case I	FN (Hz)	59.84	59.87	18.37%	59.92	49.98%
	ST (s)	63.25	58	5.25	24	34
Case II	FN (Hz)	59.95	59.95	20%	59.99	80%
	ST (s)	56.58	49.12	7.46	18.26	38.32

simulated at bus 72. In the case of SL, a 1400 kW of the unbalanced load is added to the system at 10 seconds. For LG fault event, Phase A fault is simulated for 0.18 seconds on bus 72 between phase and ground with fault and ground resistance both being 1 Ω. Fig. 6.4 shows the DC ring interconnection and the test cases I and II performed on the modified 123 bus system.

6.5.1 Frequency response to Step loading (Case I)

Fig. 6.5 shows PCC angles for inverters 1 and 2, the frequency regulation comparison for various approaches and PU HESS power-sharing from DERs towards inverter 1, given by Bat_a and UC_a, and inverter 2, given by Bat_b and UC_b in response to step loading condition initiated at 10 seconds in simulation on the modified 123 bus system. As a result of adding 1400 kW of unbalanced loads, the default frequency nadir of the test system drops to 59.84 Hz. For the frequency-droop approach, the frequency nadir improves by 0.03 Hz, up to 59.87 Hz. The proposed global consensus-based optimal

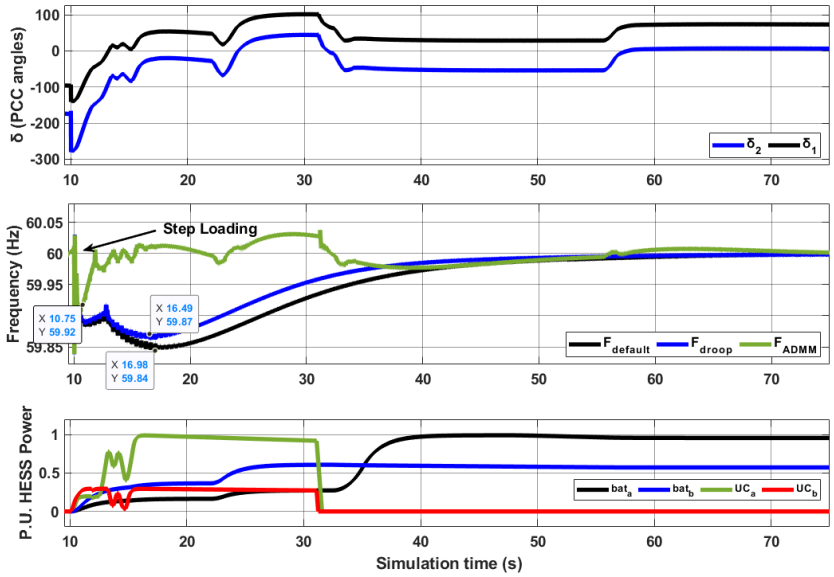

Figure 6.5: Case I : Frequency regulation [default system Vs $\Delta\delta$ minimization using consensus based optimal control Vs Frequency-droop].

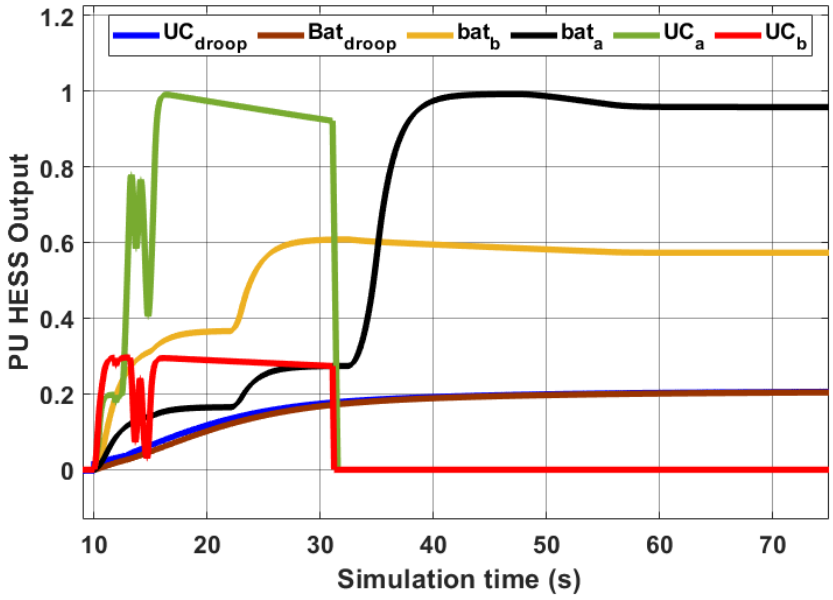

Figure 6.6: Case I : Per Unit control output for various frequency regulation approaches.

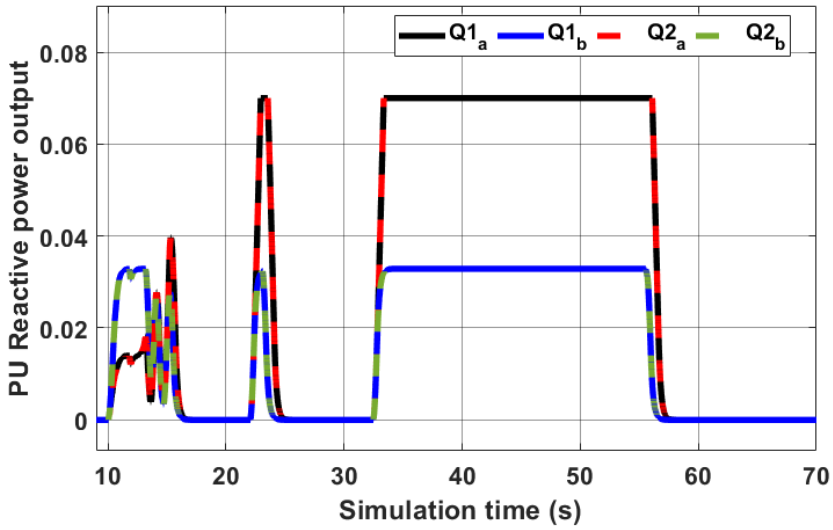

Figure 6.7: Case I : Per Unit reactive power support for Inverter angle minimization.

control approach performs best with a frequency nadir of 59.92 Hz. This is a 0.08 Hz improvement from the synchronous generator's inertial response. The default system settles at 63.25 seconds. The frequency-droop approach settles 5 seconds faster than the default system at 58 seconds. The proposed approach settles the fastest in 34 seconds. For the proposed approach, Fig. 6.6 shows the power pushed by battery and UC devices into each of the inverters. This uneven power distribution amongst inverters is due to larger PCC voltage angle deviations observed on inverter 2 $\Delta\delta_b$ compared to that seen by inverter 1 $\Delta\delta_a$. The global consensus-based optimization defines both the active power and the reactive power contribution towards regulating frequency. Fig. 6.7 shows the reactive power support for each of the inverters.

6.5.2 Frequency response to L-G Fault (Case II)

For LG events, the frequency nadir drops to 59.95 Hz for the default system. As shown in Fig. 6.8, the consensus-based optimal control approach shows the best performance as the frequency nadir hardly drops below regulation at 59.99 Hz as compared to 59.96 Hz for frequency-droop control. The proposed architecture shows an improvement of 0.04 Hz from the base case response of the synchronous generator. To quantify this, it's an 80% improvement from the default response. The proposed

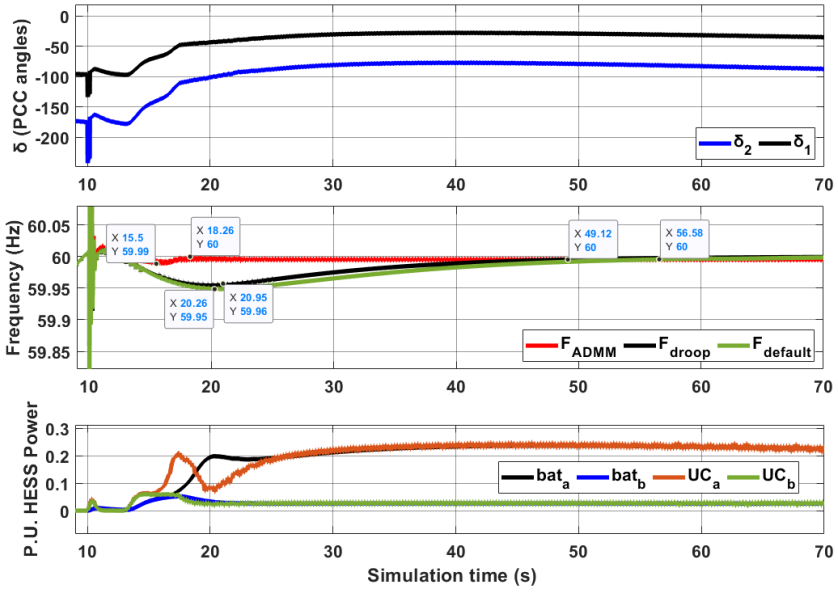

Figure 6.8: Case II : Frequency regulation [default system Vs $\Delta\delta$ minimization using consensus based optimal control Vs Frequency-droop].

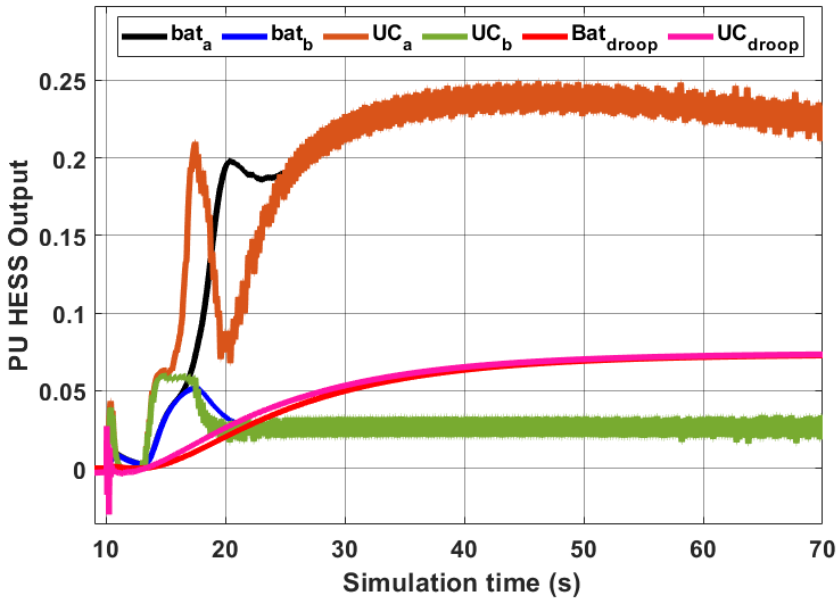

Figure 6.9: Case II : Per Unit control output for various frequency regulation approaches.

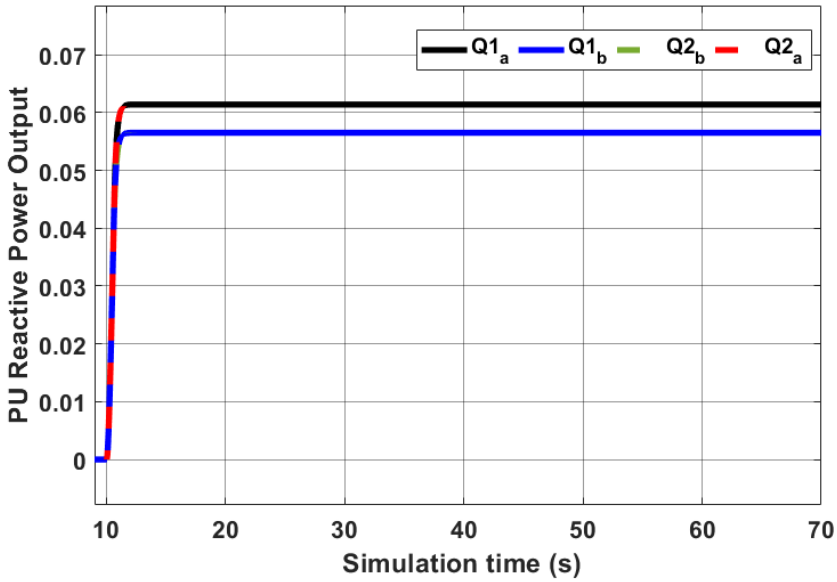

Figure 6.10: Case II : Per Unit reactive power support for Inverter angle minimization.

architecture also settles 38.32 seconds faster than the default response and 31 seconds faster than the conventional frequency droop approach. Unlike Case I, the power contribution to both inverters is almost the same. This is because of the nature of the fault event under study. The ($\Delta\delta$) deviation does not persist long enough for the HESS to react to it and hence they supply the same power to both inverters.

Table 6.1 showcases the result for the modified 123 bus system. The proposed architecture performs well for both the inertial response and secondary response. The following abbreviations are used for this table: Par. is Parameter, FN is Frequency Nadir, ST is settling time, Imp. is Improvement versus Modified Bus System, MBSCOpt is Consensus-based Optimal Control, MBSFD is Frequency Droop, MBS is Modified Bus System.

6.6 Conclusions

This chapter provides a novel frequency regulation approach that generates HESS setpoints based on PCC angle deviations and fault proximity. Setpoints are deduced using all possible input-output combinations within the proposed micro-grid architecture which results in a global consensus for optimization. The result section provides a

quantitative comparison between the proposed architecture and the frequency-droop approach based on frequency nadir and settling time parameters. It was observed that the proposed consensus-based optimal control significantly improves the inertial and secondary frequency responses of the system to grid dynamic/fault conditions. The chapter also designs and studies a DC-AC hybrid micro-grid by modifying the IEEE 123 bus system with a DC ring consisting of 4 DERs and interconnecting the DC ring structure at 2 locations on the 123 bus system through $d-q$ inverters. This chapter could serve as a good reference to start and improve on the applications of the droop-less frequency regulation approach that can be favorable for upcoming DERs connected in DC topologies. In summary, the chapter proposes a DC-AC hybrid architecture that aims at regulating the grid frequency locally and independent of the dynamics introduced by other micro-grids in the network.

6.7 Summary of Proposed DC-AC micro-grid control architecture

This section proposes a comprehensive DC-AC multi-micro-grid architecture involving 4 DERs connecting in a DC Ring and the modified IEEE 123 bus distribution system acting as an AC micro-grid. The proposed system serves as a testbed to implement and validate a global consensus-based optimal control operation for frequency regulation. $\Delta\delta$ minimization-based frequency regulation approach proposed in the earlier section is validated with the DC-AC multi-micro-grid structure. Finally, the proposed frequency regulation approach is compared with the conventional frequency-droop using DC-AC multi-micro-grid system.

CHAPTER 7: CONCLUSION AND FUTURE WORK

7.1 Conclusion

This thesis presents a novel, locally controlled, voltage angle minimization-based frequency regulation approach that can operate without the knowledge of system droop characteristics. The approach is tested using various control methods including Conventional LQR, a control uncertainty-based dynamic LQR, and compared with the conventional frequency-droop approach. Finally, the proposed approach is validated using an LQR based optimization on a MIMO DC-AC hybrid multi-micro-grid for global consensus on DER dispatch to contribute towards frequency regulation.

The contributions of this thesis are as follows:

- Proposed PCC angle minimization-based frequency regulation approach that can support the inertial and secondary response of grid frequency by compensating for locally detected voltage angle deviations. The architecture scalability is tested and validated on a modified IEEE 13 and 123 bus distribution system. The test system improves the frequency nadir by up to 7% and settling time by up to 30 seconds using the proposed approach.

- Tested $\Delta\delta$ minimization-based LQR control for frequency regulation on modified IEEE 123 bus system as an enhancement to the proposed PCC angle minimization approach. The improved approach performs slightly better than the conventional frequency-droop approach for primary frequency regulation by controlling RoCoF. The secondary frequency response is significantly improved compared to the conventional approach. For the LLG and LLLG case studies performed, the proposed approach shows frequency nadir improvement of up to

4.5% and faster settling time up to 45 seconds.

- The existing LQR approach is improved by initializing penalty factors based on control uncertainty and allowing power-sharing optimization between HESS devices based on the effect of individual device dispatch on frequency sensitivity. Frequency nadir improvements of up to 40% are recorded for the proposed approach. It also displays a faster settling time of up to 46 seconds when compared to the frequency-droop approach.

- Proposed a DC-AC hybrid multi-micro-grid with DC ring system that provides a comprehensive test bench which can be validated using modified IEEE 123 bus system as the AC sub-system. The proposed consensus-based optimal control improves the inertial response by up to 32% and secondary response by up to 38 seconds.

7.2 Future work

Future work related to this research can be directed towards the following areas:

- Testing and Validation for the proposed comprehensive DC-AC multi-micro-grid architecture in a real-time environment. The architecture can be scaled even further to consist of 20 DER DC Ring with 4 three-phase $d-q$ inverters feeding into a modified IEEE 123 bus system.

- ADMM based MIMO identification can be tested and validated in a real-time environment to probe into the possibility of its real-time field implementation with respect to computational burden.

REFERENCES

[1] F. Katiraei, R. Iravani, N. Hatziargyriou, and A. Dimeas, "Microgrids management," *IEEE Power and Energy Magazine*, vol. 6, pp. 54–65, May 2008.

[2] A. Bidram and A. Davoudi, "Hierarchical structure of microgrids control system," *IEEE Transactions on Smart Grid*, vol. 3, pp. 1963–1976, Dec 2012.

[3] J. M. Guerrero, L. Hang, and J. Uceda, "Control of distributed uninterruptible power supply systems," *IEEE Transactions on Industrial Electronics*, vol. 55, pp. 2845–2859, Aug 2008.

[4] H. Zhou, T. Bhattacharya, D. Tran, T. S. T. Siew, and A. M. Khambadkone, "Composite energy storage system involving battery and ultracapacitor with dynamic energy management in microgrid applications," *IEEE Transactions on Power Electronics*, vol. 26, pp. 923–930, March 2011.

[5] C. J. Hanley, D. T. Ton, J. D. Boyes, and G. H. Peek, "Solar energy grid integration systems – energy storage (segis-es).,"

[6] J. M. Guerrero, J. C. Vasquez, J. Matas, M. Castilla, and L. G. de Vicuna, "Control strategy for flexible microgrid based on parallel line-interactive ups systems," *IEEE Transactions on Industrial Electronics*, vol. 56, pp. 726–736, March 2009.

[7] H. H. Huang, C. Y. Hsieh, J. Y. Liao, and K. H. Chen, "Adaptive droop resistance technique for adaptive voltage positioning in boost dc x2013;dc converters," *IEEE Transactions on Power Electronics*, vol. 26, pp. 1920–1932, July 2011.

[8] J. M. Guerrero, J. C. VÃ¡squez, and R. Teodorescu, "Hierarchical control of droop-controlled dc and ac microgrids x2014; a general approach towards standardization," in *2009 35th Annual Conference of IEEE Industrial Electronics*, pp. 4305–4310, Nov 2009.

[9] S. Augustine, M. K. Mishra, and N. Lakshminarasamma, "Adaptive droop control strategy for load sharing and circulating current minimization in low-voltage standalone dc microgrid," *IEEE Transactions on Sustainable Energy*, vol. 6, pp. 132–141, Jan 2015.

[10] J. Schonbergerschonberger, R. Duke, and S. D. Round, "Dc-bus signaling: A distributed control strategy for a hybrid renewable nanogrid," *IEEE Transactions on Industrial Electronics*, vol. 53, pp. 1453–1460, Oct 2006.

[11] S. Anand, B. G. Fernandes, and J. Guerrero, "Distributed control to ensure proportional load sharing and improve voltage regulation in low-voltage dc microgrids," *IEEE Transactions on Power Electronics*, vol. 28, pp. 1900–1913, April 2013.

[12] H. Kakigano, Y. Miura, and T. Ise, "Distribution voltage control for dc microgrids using fuzzy control and gain-scheduling technique," *IEEE Transactions on Power Electronics*, vol. 28, pp. 2246–2258, May 2013.

[13] M. Farhadi and O. Mohammed, "Adaptive energy management in redundant hybrid dc microgrid for pulse load mitigation," *IEEE Transactions on Smart Grid*, vol. 6, pp. 54–62, Jan 2015.

[14] C. Jin, P. Wang, J. Xiao, Y. Tang, and F. H. Choo, "Implementation of hierarchical control in dc microgrids," *IEEE Transactions on Industrial Electronics*, vol. 61, pp. 4032–4042, Aug 2014.

[15] H. Lotfi and A. Khodaei, "Ac versus dc microgrid planning," *IEEE Transactions on Smart Grid*, vol. 8, pp. 296–304, Jan 2017.

[16] A. Khodaei, S. Bahramirad, and M. Shahidehpour, "Microgrid planning under uncertainty," *IEEE Transactions on Power Systems*, vol. 30, pp. 2417–2425, Sept 2015.

[17] P. T. Baboli, M. Shahparasti, M. P. Moghaddam, M. R. Haghifam, and M. Mohamadian, "Energy management and operation modelling of hybrid ac x2013;dc microgrid," *IET Generation, Transmission Distribution*, vol. 8, pp. 1700–1711, October 2014.

[18] P. Cairoli and R. A. Dougal, "New horizons in dc shipboard power systems: New fault protection strategies are essential to the adoption of dc power systems.," *IEEE Electrification Magazine*, vol. 1, pp. 38–45, Dec 2013.

[19] E. J. Ng and R. A. El-Shatshat, "Multi-microgrid control systems (mmcs)," in *IEEE PES General Meeting*, pp. 1–6, July 2010.

[20] R. H. Lasseter, "Smart distribution: Coupled microgrids," *Proceedings of the IEEE*, vol. 99, pp. 1074–1082, June 2011.

[21] W. Saad, Z. Han, H. V. Poor, and T. Basar, "Game-theoretic methods for the smart grid: An overview of microgrid systems, demand-side management, and smart grid communications," *IEEE Signal Processing Magazine*, vol. 29, pp. 86–105, Sept 2012.

[22] J. M. Eyer and G. P. Corey, "Energy storage for the electricity grid : benefits and market potential assessment guide : a study for the doe energy storage systems program.,"

[23] M. J. Erickson, T. M. Jahns, and R. H. Lasseter, "Comparison of pv inverter controller configurations for certs microgrid applications," in *2011 IEEE Energy Conversion Congress and Exposition*, pp. 659–666, Sept 2011.

[24] N. Mendis, K. M. Muttaqi, S. Sayeef, and S. Perera, "Application of a hybrid energy storage in a remote area power supply system," in *2010 IEEE International Energy Conference*, pp. 576–581, Dec 2010.

[25] W. Li, G. Joos, and J. Belanger, "Real-time simulation of a wind turbine generator coupled with a battery supercapacitor energy storage system," *IEEE Transactions on Industrial Electronics*, vol. 57, pp. 1137–1145, April 2010.

[26] Y. Zhang, Z. Jiang, and X. Yu, "Control strategies for battery/supercapacitor hybrid energy storage systems," in *2008 IEEE Energy 2030 Conference*, pp. 1–6, Nov 2008.

[27] L. Gao, R. A. Dougal, and S. Liu, "Power enhancement of an actively controlled battery/ultracapacitor hybrid," *IEEE Transactions on Power Electronics*, vol. 20, pp. 236–243, Jan 2005.

[28] O. Torres-PÃ©rez, S. MÃ©ndez-Murillo, and N. Quijano, "Comparative analysis of mppt techniques for a photovoltaic system in cundinamarca," in *2017 IEEE 3rd Colombian Conference on Automatic Control (CCAC)*, pp. 1–6, Oct 2017.

[29] V. R. Kota and M. N. Bhukya, "A simple and efficient mppt scheme for pv module using 2-dimensional lookup table," in *2016 IEEE Power and Energy Conference at Illinois (PECI)*, pp. 1–7, Feb 2016.

[30] N. Alamir, M. A. Ismeil, and M. Orabi, "New mppt technique using phase-shift modulation for llc resonant micro-inverter," in *2017 Nineteenth International Middle East Power Systems Conference (MEPCON)*, pp. 1465–1470, Dec 2017.

[31] C. Abbey and G. Joos, "Short-term energy storage for wind energy applications," in *Fourtieth IAS Annual Meeting. Conference Record of the 2005 Industry Applications Conference, 2005.*, vol. 3, pp. 2035–2042 Vol. 3, Oct 2005.

[32] T. Zhou and B. Francois, "Energy management and power control of a hybrid active wind generator for distributed power generation and grid integration," *IEEE Transactions on Industrial Electronics*, vol. 58, pp. 95–104, Jan 2011.

[33] X. He, H. Ji, Y. Song, G. Song, H. Cai, and Y. Mi, "Voltage stability control for dc microgrid with energy storage," in *2017 IEEE Conference on Energy Internet and Energy System Integration (EI2)*, pp. 1–6, Nov 2017.

[34] T. R. Oliveira, W. W. A. G. Silva, and P. F. Donoso-Garcia, "Distributed secondary level control for energy storage management in dc microgrids," *IEEE Transactions on Smart Grid*, vol. 8, pp. 2597–2607, Nov 2017.

[35] M. A. Silva, H. N. de Melo, J. P. TrovÃ£o, P. G. Pereirinha, and H. M. Jorge, "Hybrid topologies comparison for electric vehicles with multiple energy storage systems," in *2013 World Electric Vehicle Symposium and Exhibition (EVS27)*, pp. 1–8, Nov 2013.

[36] P. Karlsson and J. Svensson, "Dc bus voltage control for a distributed power system," *IEEE Transactions on Power Electronics*, vol. 18, pp. 1405–1412, Nov 2003.

[37] H. Kakigano, Y. Miura, T. Ise, and R. Uchida, "Dc voltage control of the dc micro-grid for super high quality distribution," in *2007 Power Conversion Conference - Nagoya*, pp. 518–525, April 2007.

[38] L. Zhang, T. Wu, Y. Xing, K. Sun, and J. M. Gurrero, "Power control of dc microgrid using dc bus signaling," in *2011 Twenty-Sixth Annual IEEE Applied Power Electronics Conference and Exposition (APEC)*, pp. 1926–1932, March 2011.

[39] D. Chen, L. Xu, and L. Yao, "Dc voltage variation based autonomous control of dc microgrids," *IEEE Transactions on Power Delivery*, vol. 28, pp. 637–648, April 2013.

[40] D. Salomonsson and A. Sannino, "Low-voltage dc distribution system for commercial power systems with sensitive electronic loads," *IEEE Transactions on Power Delivery*, vol. 22, pp. 1620–1627, July 2007.

[41] T. DragiÄeviÄ, J. M. Guerrero, and J. C. Vasquez, "A distributed control strategy for coordination of an autonomous lvdc microgrid based on power-line signaling," *IEEE Transactions on Industrial Electronics*, vol. 61, pp. 3313–3326, July 2014.

[42] J. Rocabert, A. Luna, F. Blaabjerg, and P. RodrÃguez, "Control of power converters in ac microgrids," *IEEE Transactions on Power Electronics*, vol. 27, pp. 4734–4749, Nov 2012.

[43] E. Mojica-Nava, C. A. Macana, and N. Quijano, "Dynamic population games for optimal dispatch on hierarchical microgrid control," *IEEE Transactions on Systems, Man, and Cybernetics: Systems*, vol. 44, pp. 306–317, March 2014.

[44] L. Meng, F. Tang, M. Savaghebi, J. Vasquez, and J. Guerrero, "Tertiary control of voltage unbalance compensation for optimal power quality in islanded microgrids," in *2016 IEEE Power and Energy Society General Meeting (PESGM)*, pp. 1–1, July 2016.

[45] F. Shahnia, R. P. S. Chandrasena, S. Rajakaruna, and A. Ghosh, "Primary control level of parallel distributed energy resources converters in system of multiple interconnected autonomous microgrids within self-healing networks," *IET Generation, Transmission Distribution*, vol. 8, pp. 203–222, February 2014.

[46] M. Cucuzzella, G. P. Incremona, and A. Ferrara, "Decentralized sliding mode control of islanded ac microgrids with arbitrary topology," *IEEE Transactions on Industrial Electronics*, vol. 64, pp. 6706–6713, Aug 2017.

[47] G. P. Incremona, M. Cucuzzella, A. Ferrara, and L. Magni, "Model predictive control and sliding mode control for current sharing in microgrids," in *2017 IEEE 56th Annual Conference on Decision and Control (CDC)*, pp. 2661–2666, Dec 2017.

[48] M. A. Nezhad and H. Bevrani, "Frequency control in an islanded hybrid microgrid using frequency response analysis tools," *IET Renewable Power Generation*, vol. 12, no. 2, pp. 227–243, 2018.

[49] Y. Xia, Y. Peng, and W. Wei, "Triple droop control method for ac microgrids," *IET Power Electronics*, vol. 10, no. 13, pp. 1705–1713, 2017.

[50] T. L. Vandoorn, B. Renders, L. Degroote, B. Meersman, and L. Vandevelde, "Active load control in islanded microgrids based on the grid voltage," *IEEE Transactions on Smart Grid*, vol. 2, pp. 139–151, March 2011.

[51] P. M. Diaz and H. J. El-Khozondar, "Electrical energy storage technologies and the application potential in power system operation: A mini review," in *2019 IEEE 7th Palestinian International Conference on Electrical and Computer Engineering (PICECE)*, pp. 1–9, 2019.

[52] S. Vazquez, S. M. Lukic, E. Galvan, L. G. Franquelo, and J. M. Carrasco, "Energy storage systems for transport and grid applications," *IEEE Transactions on Industrial Electronics*, vol. 57, no. 12, pp. 3881–3895, 2010.

[53] R. Abhinav and N. M. Pindoriya, "Grid integration of wind turbine and battery energy storage system: Review and key challenges," in *2016 IEEE 6th International Conference on Power Systems (ICPS)*, pp. 1–6, 2016.

[54] A. Chauhan and R. P. Saini, "Renewable energy based power generation for stand-alone applications: A review," in *2013 International Conference on Energy Efficient Technologies for Sustainability*, pp. 424–428, 2013.

[55] Y. Han, X. Ning, P. Yang, and L. Xu, "Review of power sharing, voltage restoration and stabilization techniques in hierarchical controlled dc microgrids," *IEEE Access*, vol. 7, pp. 149202–149223, 2019.

[56] H. Bevrani, A. Ghosh, and G. Ledwich, "Renewable energy sources and frequency regulation: survey and new perspectives," *IET Renewable Power Generation*, vol. 4, no. 5, pp. 438–457, 2010.

[57] Houhe Chen and Yiming Kong, "Optimal spinning reserve for wind power integrated system using cvar," in *2014 IEEE Conference and Expo Transportation Electrification Asia-Pacific (ITEC Asia-Pacific)*, pp. 1–4, 2014.

[58] H. Yuhui, L. Dong, and L. Huaiqing, "Site and size selection strategies of energy storage system based on power supply and storage capability index," in *International Conference on Renewable Power Generation (RPG 2015)*, pp. 1–6, 2015.

[59] F. Matthey, T. Kamijoh, K. Takeda, S. Ando, T. Nomura, T. Shibata, and A. Honzawa, "Cost-benefit analysis tool and control strategy selection for lithium-ion battery energy storage system," in *2015 IEEE Power Energy Society General Meeting*, pp. 1–5, 2015.

[60] I. Alsaidan, A. Khodaei, and W. Gao, "Determination of battery energy storage technology and size for standalone microgrids," in *2016 IEEE Power and Energy Society General Meeting (PESGM)*, pp. 1–5, 2016.

[61] B. Das and A. Kumar, "Optimal sizing and selection of energy storage system considering load uncertainty," in *2018 2nd International Conference on Power, Energy and Environment: Towards Smart Technology (ICEPE)*, pp. 1–9, 2018.

[62] C. Romaus, J. Bocker, K. Witting, A. Seifried, and O. Znamenshchykov, "Optimal energy management for a hybrid energy storage system combining batteries and double layer capacitors," in *2009 IEEE Energy Conversion Congress and Exposition*, pp. 1640–1647, 2009.

[63] T. Thomas and M. K. Mishra, "Control strategy for a pv-wind based standalone dc microgrid with hybrid energy storage system," in *2019 IEEE 1st International Conference on Energy, Systems and Information Processing (ICESIP)*, pp. 1–6, 2019.

[64] X. Zeng, T. Liu, S. Wang, Y. Dong, and Z. Chen, "Comprehensive coordinated control strategy of pmsg-based wind turbine for providing frequency regulation services," *IEEE Access*, vol. 7, pp. 63944–63953, 2019.

[65] P. C. Nakka and M. K. Mishra, "Droop characteristics based damping and inertia emulation of dc link in a hybrid microgrid," *IET Renewable Power Generation*, vol. 14, no. 6, pp. 1044–1052, 2020.

[66] Y. Fu, Y. Wang, and X. Zhang, "Integrated wind turbine controller with virtual inertia and primary frequency responses for grid dynamic frequency support," *IET Renewable Power Generation*, vol. 11, no. 8, pp. 1129–1137, 2017.

[67] Z. Peng, J. Wang, D. Bi, Y. Dai, and Y. Wen, "The application of microgrids based on droop control with coupling compensation and inertia," *IEEE Transactions on Sustainable Energy*, vol. 9, no. 3, pp. 1157–1168, 2018.

[68] K. W. Joung, T. Kim, and J. Park, "Decoupled frequency and voltage control for stand-alone microgrid with high renewable penetration," *IEEE Transactions on Industry Applications*, vol. 55, no. 1, pp. 122–133, 2019.

[69] U. Datta, A. Kalam, and J. Shi, "Battery energy storage system control for mitigating pv penetration impact on primary frequency control and state-of-charge recovery," *IEEE Transactions on Sustainable Energy*, vol. 11, no. 2, pp. 746–757, 2020.

[70] Y. Li, L. He, F. Liu, C. Li, Y. Cao, and M. Shahidehpour, "Flexible voltage control strategy considering distributed energy storages for dc distribution network," *IEEE Transactions on Smart Grid*, vol. 10, no. 1, pp. 163–172, 2019.

[71] X. Li, Z. Li, L. Guo, J. Zhu, Y. Wang, and C. Wang, "Enhanced dynamic stability control for low-inertia hybrid ac/dc microgrid with distributed energy storage systems," *IEEE Access*, vol. 7, pp. 91234–91242, 2019.

[72] A. Joshi, A. Suresh, and S. Kamalasadan, "Control and dispatch of distributed energy resources with improved frequency regulation using fully active hybrid energy storage system," in *2020 IEEE International Conference on Power Electronics, Smart Grid and Renewable Energy (PESGRE2020)*, pp. 1–6, 2020.

[73] M. Davari and Y. A. I. Mohamed, "Robust vector control of a very weak-grid-connected voltage-source converter considering the phase-locked loop dynamics," *IEEE Transactions on Power Electronics*, vol. 32, pp. 977–994, Feb 2017.

[74] P. Wang, J. Xiao, L. Setyawan, C. Jin, and C. F. Hoong, "Hierarchical control of active hybrid energy storage system (hess) in dc microgrids," in *2014 9th IEEE Conference on Industrial Electronics and Applications*, pp. 569–574, June 2014.

[75] W. H. Kersting, "Radial distribution test feeders," in *2001 IEEE Power Engineering Society Winter Meeting. Conference Proceedings (Cat. No.01CH37194)*, vol. 2, pp. 908–912 vol.2, Jan 2001.

[76] D. Chen, Y. Xu, and A. Q. Huang, "Integration of dc microgrids as virtual synchronous machines into the ac grid," *IEEE Transactions on Industrial Electronics*, vol. 64, pp. 7455–7466, Sep. 2017.

[77] J. Fang, Y. Tang, H. Li, and X. Li, "A battery/ultracapacitor hybrid energy storage system for implementing the power management of virtual synchronous generators," *IEEE Transactions on Power Electronics*, vol. 33, pp. 2820–2824, April 2018.

[78] G. Deshpande and S. Kamalasadan, "An approach for micro grid management with hybrid energy storage system using batteries and ultra capacitors," in *2014 IEEE PES General Meeting | Conference Exposition*, pp. 1–5, July 2014.

[79] N. Arab, B. Kedjar, A. Javadi, and K. Al-Haddad, "A multifunctional single-phase grid-integrated residential solar pv systems based on lqr control," *IEEE Transactions on Industry Applications*, vol. 55, no. 2, pp. 2099–2109, 2019.

[80] E. Okyere, A. Bousbaine, G. T. Poyi, A. K. Joseph, and J. M. Andrade, "Lqr controller design for quad-rotor helicopters," *The Journal of Engineering*, vol. 2019, no. 17, pp. 4003–4007, 2019.

[81] B. Mu and Y. Shi, "Distributed lqr consensus control for heterogeneous multiagent systems: Theory and experiments," *IEEE/ASME Transactions on Mechatronics*, vol. 23, no. 1, pp. 434–443, 2018.

[82] H. Zhang, T. Feng, H. Liang, and Y. Luo, "Lqr-based optimal distributed cooperative design for linear discrete-time multiagent systems," *IEEE Transactions on Neural Networks and Learning Systems*, vol. 28, no. 3, pp. 599–611, 2017.

[83] Z. Dongmei, W. Xingang, and M. Li, "Consensus for multi-agent dynamic systems: An lqr perspective," in *Proceedings of the 31st Chinese Control Conference*, pp. 6261–6266, 2012.

[84] C. Han and W. Wang, "Distributed observer-based lqr control for discrete-time multi-agent systems," in *2017 29th Chinese Control And Decision Conference (CCDC)*, pp. 5573–5578, 2017.

[85] H. Sun, Y. Liu, F. Li, and X. Niu, "Distributed lqr optimal protocol for leader-following consensus," *IEEE Transactions on Cybernetics*, vol. 49, no. 9, pp. 3532–3546, 2019.

[86] Y.Kimpara, M.Kurimoto, and T. Y.Manabe, "An experimental study on active power control of photovoltaic power generation for supporting grid frequency regulation," in *2018 IEEE Power Energy Society General Meeting (PESGM)*, pp. 1–5, Aug 2018.

[87] Y. A. I. Mohamed and E. F. El-Saadany, "Adaptive decentralized droop controller to preserve power sharing stability of paralleled inverters in distributed generation microgrids," *IEEE Transactions on Power Electronics*, vol. 23, pp. 2806–2816, Nov 2008.

[88] A. Wang and J. Zhang, "A novel reactive power control strategy in virtual flux droop control," in *2017 18th International Symposium on Electromagnetic Fields in Mechatronics, Electrical and Electronic Engineering (ISEF) Book of Abstracts*, pp. 1–2, Sep. 2017.

[89] A. Thakallapelli and S. Kamalasadan, "An online reduced order modeling based frequency regulation adaptive control architecture for wind integrated power grid," in *2018 IEEE Industry Applications Society Annual Meeting (IAS)*, pp. 1–8, Sep. 2018.

[90] e. X. Kong, J. Pan, "Emulating the features of conventional generator with virtual synchronous generator technology: an overview," *The Journal of Engineering*, vol. 2017, no. 13, pp. 2135–2139, 2017.

[91] H. Ali, B. Li, Z. Xu, H. Liu, and D. Xu, "Virtual synchronous generator design based modular multilevel converter for microgrid frequency regulation," in *2019 22nd International Conference on Electrical Machines and Systems (ICEMS)*, pp. 1–6, 2019.

[92] J. Fang, X. Li, Y. Tang, and H. Li, "Power management of virtual synchronous generators through using hybrid energy storage systems," in *2018 IEEE Applied Power Electronics Conference and Exposition (APEC)*, pp. 1407–1411, March 2018.

[93] J. F. Patarroyo-Montenegro, J. E. Salazar-Duque, and F. Andrade, "Lqr controller with optimal reference tracking for inverter-based generators on islanded-mode microgrids," in *2018 IEEE ANDESCON*, pp. 1–5, 2018.

[94] R. Bimarta and K. Kim, "A robust frequency-adaptive current control of a grid-connected inverter based on lmi-lqr under polytopic uncertainties," *IEEE Access*, vol. 8, pp. 28756–28773, 2020.

[95] D. Das, G. Gurrala, and U. J. Shenoy, "Linear quadratic regulator-based bumpless transfer in microgrids," *IEEE Transactions on Smart Grid*, vol. 9, no. 1, pp. 416–425, 2018.

[96] G. R. GonÃ§alves da Silva, A. S. Bazanella, C. Lorenzini, and L. Campestrini, "Data-driven lqr control design," *IEEE Control Systems Letters*, vol. 3, no. 1, pp. 180–185, 2019.

[97] D. O. NeacÅu and A. SÃ®rbu, "Design of a lqr-based boost converter controller for energy savings," *IEEE Transactions on Industrial Electronics*, vol. 67, no. 7, pp. 5379–5388, 2020.

[98] L. Wei and F. Fang, "H_∞-lqr-based coordinated control for large coal-fired boilerâturbine generation units," *IEEE Transactions on Industrial Electronics*, vol. 64, no. 6, pp. 5212–5221, 2017.

[99] U. Markovic, Z. Chu, P. Aristidou, and G. Hug, "Lqr-based adaptive virtual synchronous machine for power systems with high inverter penetration," *IEEE Transactions on Sustainable Energy*, vol. 10, no. 3, pp. 1501–1512, 2019.

[100] S. Abdelrazek and S. Kamalasadan, "A weather-based optimal storage management algorithm for pv capacity firming," *IEEE Transactions on Industry Applications*, vol. 52, no. 6, pp. 5175–5184, 2016.

[101] V. Cecchi, S. Kamalasadan, J. Enslin, and M. Miller, "Grid impacts and mitigation measures for increased pv penetration levels using advanced pv inverter regulation," in *2013 IEEE Energy Conversion Congress and Exposition*, pp. 561–568, IEEE, 2013.

[102] S. Kamalasadan, *A new generation of adaptive control: An intelligent supervisory loop approach.* PhD thesis, University of Toledo, 2004.

[103] M. Ghafouri, U. Karaagac, H. Karimi, S. Jensen, J. Mahseredjian, and S. O. Faried, "An lqr controller for damping of subsynchronous interaction in dfig-based wind farms," *IEEE Transactions on Power Systems*, vol. 32, no. 6, pp. 4934–4942, 2017.

[104] R. Bisht, A. Suresh, and S. Kamalasadan, "Multiple single phase inverters based combined active power management and voltage regulation of power distribution system based on a novel optimal control architecture," in *2019 North American Power Symposium (NAPS)*, pp. 1–6, 2019.

[105] A. Thakallapelli, S. J. Hossain, and S. Kamalasadan, "Coherency and online signal selection based wide area control of wind integrated power grid," *IEEE Transactions on Industry Applications*, vol. 54, no. 4, pp. 3712–3722, 2018.

[106] Y. Zheng, Y. Song, D. J. Hill, and Y. Zhang, "Multiagent system based microgrid energy management via asynchronous consensus admm," *IEEE Transactions on Energy Conversion*, vol. 33, no. 2, pp. 886–888, 2018.

[107] S. K. Akula and H. Salehfar, "Energy management system for interconnected microgrids using alternating direction method of multipliers (admm)," in *2018 North American Power Symposium (NAPS)*, pp. 1–6, 2018.

[108] Z. Lin, J. Chen, J. Ren, G. Song, and Y. Zhang, "Distributed optimal operation for distribution networks with multi-microgrid based on admm," in *2019 IEEE PES GTD Grand International Conference and Exposition Asia (GTD Asia)*, pp. 866–871, 2019.

[109] M. H. Ullah and J. Park, "Distributed energy optimization in mas-based microgrids using asynchronous admm," in *2019 IEEE Power Energy Society Innovative Smart Grid Technologies Conference (ISGT)*, pp. 1–5, 2019.

[110] M. Wang, Y. Su, L. Chen, Z. Li, and S. Mei, "Distributed optimal power flow of dc microgrids: A penalty based admm approach," *CSEE Journal of Power and Energy Systems*, pp. 1–9, 2019.

[111] S. Abhinav, I. D. Schizas, F. Ferrese, and A. Davoudi, "Optimization-based ac microgrid synchronization," *IEEE Transactions on Industrial Informatics*, vol. 13, no. 5, pp. 2339–2349, 2017.

[112] C. Ling, C. Zheng, T. Rui, and G. Li, "Real-time economic dispatching of microgrid using alternating direction multiplier method," in *2019 14th IEEE Conference on Industrial Electronics and Applications (ICIEA)*, pp. 1063–1068, 2019.

[113] G. Chen and Q. Yang, "An admm-based distributed algorithm for economic dispatch in islanded microgrids," *IEEE Transactions on Industrial Informatics*, vol. 14, no. 9, pp. 3892–3903, 2018.

[114] M. Mohiti, M. Mazidi, and H. Monsef, "An admm-based decentralized model for optimal operation of smart distribution network with multiple microgrids," in *Electrical Engineering (ICEE), Iranian Conference on*, pp. 1113–1118, 2018.

[115] O. I. Parra, J. Cruz, and E. Mojica-Nava, "Admm for transactive control of microgrids," in *2019 IEEE Milan PowerTech*, pp. 1–6, 2019.

[116] E. MÃŒnsing, J. Mather, and S. Moura, "Blockchains for decentralized optimization of energy resources in microgrid networks," in *2017 IEEE Conference on Control Technology and Applications (CCTA)*, pp. 2164–2171, 2017.

[117] L. Lu and C. Chu, "Consensus-based distributed droop control of vsgs for isolated ac micro-grids by admms," in *2016 IEEE International Symposium on Circuits and Systems (ISCAS)*, pp. 2138–2141, 2016.

[118] L. Lu and C. Chu, "Consensus-based droop control of isolated micro-grids by admm implementations," *IEEE Transactions on Smart Grid*, vol. 9, no. 5, pp. 5101–5112, 2018.

APPENDIX A: Modified IEEE 123 bus distribution system

IEEE 123 node test feeder was downloaded as a standard test distribution system from the IEEE PES website. This system operates at a nominal voltage of 4.16 kV. It provides voltage drop problems that must be solved with the application of voltage regulators and shunt capacitors. This circuit is characterized by overhead and underground lines, unbalanced loading with constant current, impedance, and power, four voltage regulators, shunt capacitor banks, and multiple switches. This circuit has minimal convergence problems. IEEE 123 node test feeder is shown in fig A.1

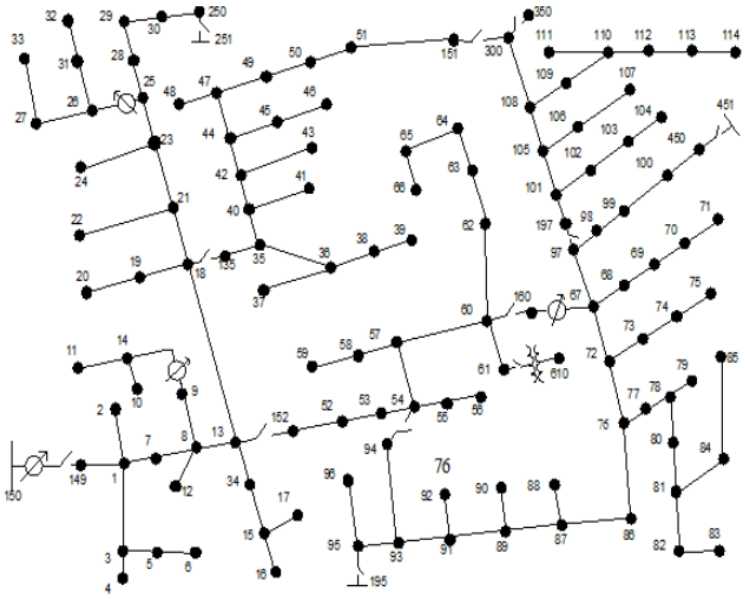

Figure A.1: IEEE 123 node test feeder

The test feeder is added with a P.U. synchronous generator model using ARTEMIS RT-LAB compatible SIMULINK SSN model. The synchronous machine is designed to look at the total active and reactive power loading on the test feeder. From the feeder data, the total 3-phase active power load does not exceed 3,490 kW, whereas the total reactive power load is 1,925 kVAR. Considering maximum loading and estimating the total DER size to be used on the test bench the synchronous generator is designed for an 8000 kVA rating.

The model of a Synchronous machine has different components. The frequency regulation loop gives the PU power reference that the synchronous generator needs to operate at. The dPslack value is then inputted to the turbine regulator SIMULINK Block. The output is vfgain which is the new field voltage set point of the synchronous generator and Pm which is the mechanical power. But we will ignore the Pm value since we already have dPslack generated by our frequency control. The dPslack value is input to the mechanical model block on the machine which gives us wmec (mechanical angular frequency). This wmec along with vfgain drives the SSN synchronous generator block as shown in fig A.2

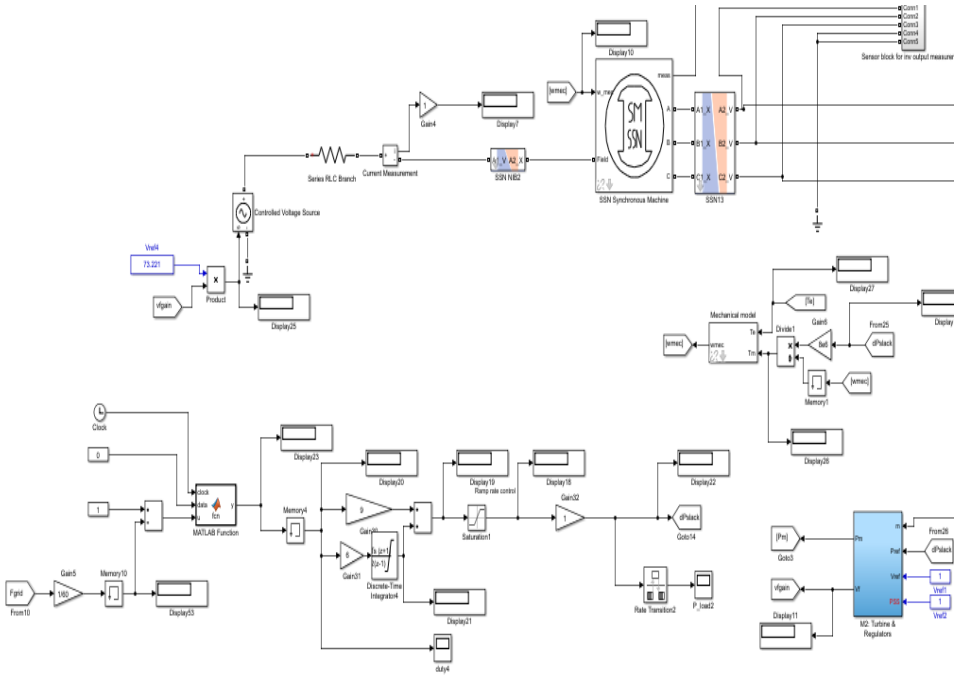

Figure A.2: SSN Synchronous Generator in SIMULINK

The P.U. design of the synchronous generator is completed using a MATLAB code shown in fig A.3

```
clc
clear all


%to get SI sync machine parameters from PU parameter inputs

nom = [8e6  13800   60];
Xdq = [2.86 0.7 0.22 2.0 0.85 0.2 0.2];
para_type = 1;
tau = [3.4 0.01 0.4 0.05];
Rs = 0.0025;
mec = [6.5 0 4];
initc = [0 17.089 1.59541 1.59541 1.59541 34.5919 -85.4081 154.592 4.05897];
simsat = 'off';
sat=[0.6404,0.7127,0.8441,0.9214,0.9956,1.082,1.19,1.316,1.457;0.7,0.7698,0.8872,0.9466,0.9969,1.046,1.1,1.151,1.201];
user_field_current=40;  % user selected I_field current
choice = '3';
[nom,sta,fld,dam,mec,ini,simsat,sat] = ssn_SynchronousMachine_STD2SI_conversion(nom,Xdq,tau,Rs,mec...
    ,initc,simsat,sat,para_type,user_field_current);
```

Figure A.3: Design of P.U. Synchronous Generator parameters